A REDUCED-ORDER MODEL OF A CHEVRON PLATE HEAT EXCHANGER FOR RAPID THERMAL MANAGEMENT BY USING THERMO-CHEMICAL ENERGY STORAGE

A Thesis

by

NICHOLAS PAUL NIEDBALSKI

Submitted to the Office of Graduate Studies of
Texas A&M University
in partial fulfillment of the requirements for the degree of

MASTER OF SCIENCE

August 2012

Major Subject: Mechanical Engineering

A Reduced-Order Model of a Chevron Plate Heat Exchanger for Rapid Thermal Management by Using Thermo-Chemical Energy Storage

A REDUCED-ORDER MODEL OF A CHEVRON PLATE HEAT EXCHANGER FOR RAPID THERMAL MANAGEMENT BY USING THERMO-CHEMICAL ENERGY STORAGE

A Thesis

by

NICHOLAS PAUL NIEDBALSKI

Submitted to the Office of Graduate Studies of
Texas A&M University
in partial fulfillment of the requirements for the degree of

MASTER OF SCIENCE

Approved by:

Chair of Committee,	Debjyoti Banerjee
Committee Members,	Robert Handler
	Marvin Adams
	Soumya Patnaik
Head of Department,	Jerry Caton

August 2012

Major Subject: Mechanical Engineering

ABSTRACT

A Reduced-Order Model of a Chevron Plate Heat Exchanger for Rapid Thermal Management by Using Thermo-Chemical Energy Storage.

(August 2012)

Nicholas Paul Niedbalski, B.S. Mechanical Engineering, Gonzaga University

Chair of Advisory Committee: Dr. Debjyoti Banerjee

The heat flux demands for electronics cooling applications are quickly approaching the limits of conventional thermal management systems. To meet the demand of next generation electronics, a means for rejecting high heat fluxes at low temperatures in a compact system is an urgent need. To answer this challenge, in this work a gasketed chevron plate heat exchanger in conjunction with a slurry consisting of highly endothermic solid ammonium carbamate and a heat transfer fluid. A reduced-order 1-dimensional model was developed and used to solve the coupled equations for heat, mass, and momentum transfer. The feasibility of this chosen design for satisfying the heat rejection load of 2kW was also explored in this study. Also, a decomposition reaction using acetic acid and sodium bicarbonate was conducted in a plate heat exchanger (to simulate a configuration similar to the ammonium carbamate reactions). This enabled the experimental validation of the numerical predictions for the momentum transfer correlations used in this study (which in turn, are closely tied to both the heat transfer correlations and chemical kinetics models). These experiments also reveal important parameters of interest that are required for the reactor design.

A numerical model was developed in this study and applied for estimating the reactor size required for achieving a power rating of 2 kW. It was found that this goal could be achieved

with a plate heat exchanger weighing less than 70 kg (~100 lbs) and occupying a volume of 29 L (which is roughly the size of a typical desktop printer).

Investigation of the hydrodynamic phenomena using flow visualization studies showed that the flow patterns were similar to those described in previous studies. This justified the adaptation of empirical correlations involving two-phase multipliers that were developed for air-water two-phase flows. High-speed video confirmed the absence of heterogeneous flow patterns and the prevalence of bubbly flow with bubble sizes typically less than 0.5 mm, which justifies the use of homogenous flow based correlations for vigorous gas-producing reactions inside a plate heat exchanger. Absolute pressure measurements - performed for experimental validation studies - indicate a significant rise in back pressure that are observed to be several times greater than the theoretically estimated values of frictional and gravitational pressure losses. The predictions from the numerical model were found to be consistent with the experimental measurements, with an average absolute error of ~26%.

DEDICATION

I wish to dedicate this thesis to my family, especially my father, Robert; my mother, Debra; and my sister, Dayna for their unwavering love and support throughout this process.

ACKNOWLEDGEMENTS

I would like to thank Dr. Soumya Patnaik (AFRL-RZPS) and Dr. Thomas Reitz (AFRL-RZPS) at AFRL-WPAFB and AFOSR for sponsoring my work at the Thermal Lab in the Propulsion Directorate, as well as for sponsoring my travel and stipend under the "Co-op" program. I also wish to thank Doug Johnson (AFRL-RZPS), who designed, procured, and assembled the experimental apparatus and assisted me in its use, in addition to providing patient, helpful advice and support toward both my experimental and computational work; Dr. Paul Krietzer (AFRL-RZPS) for the direction and assistance with the high-speed video equipment; and Dr. Jamie Ervin (AFRL-RZPS) and Stephen Emo (AFRL-RZPS). I also thank my advisor, Dr. Debjyoti Banerjee, for his mentorship and guidance during the course of my research. Also, I would like to thank the Defense Advanced Projects Agency (DARPA) - Micro/Nano-Fluidics Fundamentals Focus Center (DARPA-MF^3) - under the aegis of Dr. Abe Lee (Center Director) as well as Dr. Dennis Polla (Program Manager) and Dr. Tayo Akinawande (Program Manager) for sponsoring my research activities at Texas A&M University that partially supported me while pursuing my graduate studies for my M.S. thesis. I would also like to acknowledge our research collaborators for our DARPA-MF3 center activities - Dr. George Whitesides (Harvard University), as well as Dr. Gisela Lin and Dr. Marc Madou (University of California at Irvine). During the completion of my M.S. thesis at Texas A&M University - I was also supported from the following research projects managed by Dr. Banerjee at the Multi-Phase Flows and Heat Transfer Laboratory and the Texas Engineering Experiment Station (TEES) – which I gratefully acknowledge: Qatar National Research Foundation (QNRF); and the National Science Foundation (NSF-CBET/TTTP) under the aegis of Program Manager – Dr. Sumanta Acharyya.

There are, of course, many others to whom I am indebted, at both AFRL and Texas A&M University, for making this endeavor possible. Since it is not possible to name everyone here, I wish to extend my greatest thanks to my colleagues at both institutions for their support and advice.

NOMENCLATURE

Uppercase

A	Cross-sectional area of equivalent parallel plate channel
AC	Ammonium carbamate
B_0	Constant in Eq.(44)
B_1	Constant in Eq. (44)
B_2	Constant in Eq. (44)
C	Mass concentration, kg/m^3
Eq	Discrete conservation equation of cell (i,n)
D	Diameter, m
Da	Damköhler number
F	Constant in Eq. (101), $Pa \cdot s \cdot m^3 \cdot kg^{-1}$
Fc	Convective flux function
Fdl	Diffusive flux function, lower surface
Fdu	Diffusive flux function, upper surface
G	Constant in Eq. (5), kPa
ΔH	Enthalpy of decomposition, kJ/kg
I	Number of cells per channel
J	Total number of cells in computational domain
K	Shape factor in Eq. (40)
K_o	Kozeny's coefficient
K_1	Constant in Eq. (45)
K_2	Constant in Eq. (45)

K_3	Constant in Eq. (45)
L	Length, m
M	Number of moles
$\dot{M}'''$	Dimensionless volumetric reaction rate
N	Number of channels
Nu	Nusselt number
P	Pressure, kPa
PG	Propylene glycol
Pe	Péclet number
PHE	Plate heat exchanger
Pr	Prandtl number
$\dot{Q}$	Heat transfer rate, W/channel
R	Ratio of slurry to load side heat capacity rates
Re	Reynolds number
S	Discrete volumetric source term
T	Temperature, K
U	Superficial velocity, m/s
W	Plate width, m
X	Lockhart-Martinelli parameter
$\hat{X}$	Corrugation aspect ratio
V	Volume, m^3
$\dot{V}$	Volumetric flow rate, m^3/s
Y	Vertical position in video frame, mm
Z	Horizontal position in video frame, mm

Lowercase

a	Constant in Eq. (4), $kPa^{-1} \cdot s^{-1} \cdot m^{-2}$
b	Constant in Eq. (43)
c	Constant in Eq. (43)
$2d$	Plate spacing, m
c_p	Specific heat capacity, kJ/kg·K
e	Constant in Eq. (5), K
f	Darcy friction factor
f_0	Friction factor for flow in a sine duct in Eq. (44)
f_1	Friction factor for sinusoidal wavy flow in Eq. (45)
f_c	Friction factor for crossing flow in Eq. (46)
f_b	Friction factor for flow reversal in Eq. (47)
g	Gravitational acceleration, m^2/s
h	Convection coefficient, $W/m^2 \cdot K$
j	Total volume flux, m/s
k	Thermal conductivity, W/m·K
$\hat{k}$	Rate constant, s^{-1}
$\dot{m}'''$	Volumetric reaction rate, $kg/m^3 \cdot s$
n'''	Particles per unit volume, m^{-3}
q''	Heat flux, W/m^2
t	Time, s
t_{plate}	Thickness of plate, m
r	Ratio of initial to final molar concentration
u	Z-direction velocity, m/s

$\dot{w}$	Power, W
x	Mass quality
$\dot{x}_{PG}$	Volume fraction of propylene glycol
$\dot{x}'_{PG}$	Adjusted volume fraction of propylene glycol
y^*	Radial coordinate, m
z^*	Axial coordinate, m
z	Dimensionless axial coordinate

Greek

Λ	Corrugation pitch, m
Φ	Generic intensive flow variable
Φ_{AE}	Area enlargement factor
Φ_{TP}^2	Two-phase multiplier
α	Void fraction
λ	Thermal diffusivity, m^2/s
β	Chevron angle
γ	Constant in Eq. (39)
ε	Relative uncertainty
σ	Surface tension coefficient, N/m
θ	Dimensionless temperature
η	Dimensionless concentration
ρ	Density, kg/m^3
τ	Tortuosity factor

κ	Reaction rate constant, $kg \cdot kPa^{-2} \cdot s^{-1} \cdot m^{-2}$
ω	Particle size parameter in(13), $m^{1/3}/kg^{2/3}$
φ	Dimensionless convection coefficient
ϕ''	Numerical wall flux term
ϕ'''	Numerical volumetric source term
ξ	Similarity variable in Eq. (67)
μ	Dynamic viscosity, Pa·s
δ	Perturbation operator
ψ	Lévêque similarity function
υ	Flow distribution parameter
ζ_{Φ}	Numerical weighting parameter for variable Φ

Subscripts

A	Acceleration
G	Gravity
F	Friction
SP	Single-phase
TP	Two-phase
atm	Evaluated at atmospheric conditions
b	Bulk
c	Corrugated section
e	Equivalent
eff	Effective

g	Gas phase
eq	Equilibrium
h	Hydraulic
i	Cell index
j	Plate index
in	Inlet
l	Lower surface
ls	Liquid phase, slurry side
ld	Load fluid side
n	Channel index
out	Outlet
p	Particle
pp	Port-to-port
s	Chemical species index
u	Upper surface
w	Wall

Superscripts

*	Dimensional quantities
+	Quantities assuming perfect channel distribution

TABLE OF CONTENTS

Page

ABSTRACT iii

DEDICATION v

ACKNOWLEDGEMENTS vi

NOMENCLATURE viii

TABLE OF CONTENTS xiv

LIST OF FIGURES xvi

LIST OF TABLES xx

CHAPTER

I INTRODUCTION 1

Review of Gasketed Plate Heat Exchangers 6

II NUMERICAL MODEL DEVELOPMENT AND PREDICTIONS 11

One-dimensional Model Formulation 12
Reaction Rate Model 13
Transport Equations 18
Conservation of Mass 22
Conservation of Linear Momentum 23
Conservation of Energy 25
Inlet and Outlet Conditions 25
Plate Surface Conditions 26
Non-dimensional Transport Equations 26
Pressure Drop Correlations 28
Single-phase Flow 29
Two-phase Flow 37
Void Fraction Correlations 40
Heat Transfer Correlations 42
Singe-phase Flow 43
Two-phase Flow 45
Numerical Model 50
Computational Domain and Discretization Scheme 50
Solution Procedure 53
Temperature Dependence of Thermal Properties 57

CHAPTER Page

Model Predictions for a Reactor Sizing Problem 58
Material Properties 59
Estimation of Kinetic Parameters 62
Effect of Residence Time on Conversion 63
Axial Temperature and Concentration Profiles 70

III EXPERIMENTAL WORK 73

Motivation 73
Methodology 74
Preliminary Testing and Chemical Characterization Studies 74
Chemical Kinetics 74
Fluid Properties 78
Experimental Facility 80
Testing Procedure 85
System Assembly and Preparation 86
Testing Cycle 86
Instrument Calibration 87
Uncertainty Analysis 87
Results 93
Single-phase Pressure Drop Tests 93
Two-phase Pressure Drop Tests 96
Two-phase Multiplier Assessment 104
Void Fraction Correlation Assessment 109
Flow Visualization Results 112
Bubble Pathlines 114
Bubble Size Distributions 117

IV CONCLUSIONS AND FUTURE WORK 120

REFERENCES 125

APPENDIX A 133

APPENDIX B 135

VITA 141

LIST OF FIGURES

FIGURE		Page
1	Photograph of plate stack assembly for Alfa Laval M3 chevron plate heat exchanger used in this study	7
2	Top view of chevron pattern overlay when a pair of heat transfer plates are stacked to form flow channels. Model rendered using SolidWorks 2012	8
3	Schematic illustrating crossing flow. The blue arrows represent flow traveling along the corrugation troughs on the upper plate; the dotted red arrows represent the same for the lower plate. Note that these crossing streams are occurring in the same channel	8
4	Dissociation pressure P_{eq} as a function of temperature predicted by Equation (5) compared with experimental results obtained in the literature. Diamonds: Bennet et al [31]; Squares: Koutinas et al. [4]; Purple X's: Egan and Potts [32]; Blue stars: Briggs and Migrdichian [33]	15
5	Diagram of flow arrangement used for numerical simulations	19
6	Coordinate system and channel indexing scheme	19
7	Control volume for analyzing two-phase flow in 1-D model framework	20
8	Anatomy of the Alfa Laval M3 plate used in this work. The gasket location on plate periphery was drawn to facilitate reader understanding	30
9	Side view of typical corrugation pattern showing wavelength and height parameters	30
10	Comparison of Rouhani correlation (solid lines) and drift flux model for vertical bubbly flow (dashed lines) for different C_{in}: 1 kg/m^3 (green), 5 kg/m^3 (red), and 10 kg/m^3 (blue)	42
11	Comparison of single-phase Nusselt number predictions obtained using the correlations from (60) (red), (61) (green), and (63) blue	45
12	Comparison between two-phase Nusselt number predictions from Equation (76) as a function of conversion and single-phase Nusselt number predictions at the same superficial liquid velocity for different AC mass loadings (C_{in}). Dashed black line: Mulley and Manglik correlation, Equation (60); dashed blue line: Martin correlation, Equation (76); dashed red line: Kakac correlation, Equation (61)	49

FIGURE Page

13 Typical finite volume cell 51

14 Viscosity of pure propylene glycol (PG) as a function of temperature [39] 58

15 Conversion (top) and total latent heat absorbed (bottom) as a function of load inlet temperature for a slurry inlet pressure of 108 kPa and slurry inlet temperature of 335 K for slurry flow rates of 0.04, 0.10 and 0.14 L/s (blue, red, green)..... 64

16 Conversion as a function of load temperature for different inlet pressures and slurry flow rates of 0.014 L/s (dashed line) and 0.043 (solid line): 110 kPa (blue), 108 kPa (red), 106 kPa (orange), 105 kPa (green), and 102 kPa (black)... 65

17 Latent/sensible heat ratio as a function of normalized load temperature for slurry flow rates of 0.014 L/s (dashed line) and 0.043 L/s (solid line) for different inlet pressures: 110 kPa (blue), 108 kPa (red), 106 kPa (orange), 105 kPa (green), and 102 kPa (black) 66

18 AC mass concentration as a function of dimensionless axial distance for 108 kPa inlet pressure and slurry flow rate of 0.014 L/s for different load temperatures. AC mass loading was 8 kg/m^3 71

19 Slurry temperature profile as a function of dimensionless axial distance for 110 kPa inlet pressure and slurry flow rate of 0.014 L/s at different load temperatures. AC mass loading was 8 kg/m^3 72

20 Viscosity of PG and water mixture as a function of PG volume fraction, as calculated from averages in Table 8..... 80

21 Front view of PHE apparatus; red arrows illustrate flow path 81

22 Test rig piping and instrumentation diagram. The circle elements P0, P1, P2, P3, and P4 represent pressure transducer ports 82

23 Photograph of H-brackets and pressure screws to limit compliance of window at problematic leak regions 84

24 Total frictional pressure drop over the chevron pattern compared with predictions from Martin's (red line) and Fernandes et al.'s (blue line) correlations. Percentage of PG was adjusted to extend range of Reynolds numbers covered by the data: 20% (purple) and 31.5% (green) 95

25 Absolute pressure readings for representative single phase flow tests with both 31.5% and 20% PG/water mixtures. Each dot corresponds to the location of a pressure transducer relative to the position of transducer P0 96

FIGURE Page

26 Absolute pressure readings for test series A4 99

27 Volume flow rate for acid and bicarb pumps for test series A4 100

28 Total pressure drop for the center corrugated section (red line, P1-P3) and from inlet to outlet port (blue line, P0-P4) for test series A4 100

29 Absolute pressure versus axial position for test set A 101

30 Absolute pressure versus axial position for test set B 102

31 Absolute pressure versus axial position for test set C 102

32 Absolute pressure versus axial position for test set D 103

33 Reactor back pressure as function of maximum gas flux 104

34 Two-phase multiplier from experimental data (blue) compared to Equation (48) (red) as a function of the Lockhart-Martinelli parameter. Approximate curve fit shown in green 106

35 Comparison of numerical prediction (solid line) to experimental axial pressure profiles (dashed line) for test series A1 108

36 Comparison of numerical prediction (solid line) to experimental axial pressure profiles (dashed line) for test series D1 108

37 Gas phase superficial velocity at outlet as a function of gas phase mass flux 109

38 Gas velocity at outlet normalized by total volumetric flux using void fraction predictions from Rouhani correlation (blue) and drift flux model (red) 110

39 Void fraction predicted by Rouhani correlation (blue) and drift flux model (red) 110

40 Test series B3, run 1: axial position between pressure transducer P0 and P1. Typical of type I flow. 113

41 Test series B3, run 2: axial position between pressure transducer P2 and P3. Typical of type II flow. Blue arrows represent direction of ‘crossing flow’ furrow-directed streams (solid - upper furrows; dashed – lower furrows) 113

42 Bubble path lines traced from test B3, run 1 at various times during steady-state condition. Lines indicate crests of furrows; solid lines represent the upper plate (transparent window) and dashed lines represent the lower plate 114

FIGURE Page

43 Bubble path lines traced from test B3, run 2 at various times during steady-state condition 115

44 Bubble path lines traced from test B3, run 3 at various times. Fewer bubbles were able to be tracked because there was a higher number of bubbles in this region that adhered to the window and obscured view 115

45 Bubble velocity distribution sampled from test B3 run 1.Bubbles were selected from a “reference” frame, and their centroid position tracked for 7-10 frames thereafter. Velocity was calculated as (Yt -Yt+Δt)/Δt, where Yt is the y position of a bubble’s centroid at time t and Δt is the time interval between successive frames (0.001 sec) 117

46 Bubble size distribution for test B3, run 1 118

47 Bubble size distribution for test B3, run 2 118

LIST OF TABLES

TABLE		Page
1	Constants used in Equations (43)-(45)	36
2	Convective and diffusive flux functions rendered in discrete form	52
3	Volumetric source terms rendered in discrete form	53
4	Material property inputs for simulations	59
5	PHE geometric parameters used in simulation	61
6	Reactor size (min. number of plates) to reject a thermal load of 2 kW; all units are on a per-slurry channel basis. Red text indicates T_{ld} exceeding 85°C	68
7	Minimum number of plates required to manage the waste heat of a hypothetical 200 cm^2 electronic device assuming heat fluxes between 50 and 100 W/cm^2; red text indicates that the maximum temperature for electronics cooling has been exceeded; green text indicates most favorable operating conditions	70
8	Approximate rate constant measurements	77
9	Raw data for falling ball viscometer measurements for different PG/water mixtures	79
10	Plate geometric characteristics for M3 plates used in experiments	81
11	Instrument bias uncertainties	89
12	Total uncertainties of select experimental parameters	89
13	Pre-mixed solution uncertaities	90
14	Total relative uncertainties (ε) calculated for each two-phase experimental series	93
15	Test Matrix	97

CHAPTER I

INTRODUCTION

The removal of waste heat from electronics devices is a pressing issue. The combined effect of temperature constraints and increasing heat flux demands of next generation electronics devices are rapidly approaching the limit of conventional thermal management systems that rely on single-phase heat transfer or phase change materials. In the same vein, it is also the desire of the designers in various industries to reduce power requirements and system size for the supporting equipment in thermal management systems. Typically in electronics cooling applications, the operating temperatures are restricted to the ranges of 30-80°C. This makes the task of rejecting high heat fluxes especially problematic. Boiling or evaporative systems, though very capable of handling high heat fluxes, are of limited utility for such situations due to the severe restrictions in operating temperature. Phase change materials (PCMs), such as ice slurries or wax type materials, offer a wider range of operating temperatures, but suffer from only modest latent heats, and therefore cannot be expected to meet the demand for high specific heat duties since large quantities would be required. In the pursuit of a thermal management scheme that can handle high heat fluxes at temperatures suitable for electronics cooling applications with miniaturized system footprint, it is clear that alternate methods for capturing and dissipating low-grade waste heat are needed.

In a 2011 survey of contemporary thermal energy storage technologies for solar power, the National Renewable Energy Laboratory determined that thermochemical storage possessed superior energy densities compared to sensible or phase-change storage systems [1].

This thesis follows the style of International Journal of Thermal Sciences.

Schmidt's [2] survey of candidate technologies to address the low-grade electronics heat dissipation problem reached a similar conclusion, and ultimately determined that both high energy density and the appropriate temperature range could be achieved with a highly endothermic solid-gas chemical reaction – namely, the decomposition of solid ammonium carbamate, NH_2COONH_4. Schmidt further demonstrated with a small-scale batch reactor that the endothermic decomposition of ammonium carbamate (AC) was a feasible and promising avenue for the absorption and rejection of low-grade heat. The decomposition or formation of ammonium carbamate has been previously applied toward thermal management and thermal energy storage systems due to its high enthalpy of reaction (around 2000 kJ/kg) and commercial availability as a byproduct of urea synthesis [2, 3]. From the standpoint of contemporary high-performance electronic systems, where the rejection of low-quality heat is becoming an increasingly urgent need, the principle advantage this material offers over boiling or evaporation based systems is its ability to react strongly within the 30-60° range [2]; AC is typically found in powder form, and decomposes according to the following net reaction [4]:

$$NH_2COONH_4(s) \rightarrow CO_2(g) + 2NH_3(g) \quad (1)$$

Having established the potential for thermal management applications offered by ammonium carbamate, the next important question of engineering concern is how to best exploit its decomposition to yield high power ratings with a minimum footprint, thereby maintaining the remarkably high energy density. This question has, in part, been addressed by Schmidt in considering how to overcome the difficulty of ammonium carbamate's low thermal conductivity (~0.4 $w/m^2/K$). He suggested that the ammonium carbamate salt be immersed in a suitable liquid heat transfer medium, such as propylene or ethylene glycol, to facilitate the transport of thermal energy. However, a stirred batch reactor with a low heat transfer surface to volume ratio was used to implement this method. While capable of demonstrating the thermal management

capability of ammonium carbamate, such reaction vessel architecture would not scale well and the high energy density advantage of the chemical is lost. Therefore, developing and analyzing a practical means for delivering waste heat to the ammonium carbamate is the primary engineering objective of this thesis.

Anxionnaz *et al.* [5] explored the idea of using compact heat exchangers as multi-functional reactors and heat transfer platform owing to their high specific heat duty capabilities, which they quote as 1400 to 4000 kW/m^3/K for metallic foams and offset fin strip based systems, respectively. In particular, they considered plate heat exchangers **(**PHEs) for this purpose as well, claiming higher heat transfer coefficients and consequently lower heat transfer surface area for a given thermal load. Compared to a shell-and-tube heat exchanger for the same application, 1/2 to 1/3 of the surface area would be required. Chevron plate heat exchangers are especially attractive for this purpose because they can easily be disassembled for inspection and maintenance. They can also be modified easily allowing for more plates to be added thus extending their heat transfer capacity, if needed.

In an earlier paper, Edge *et al.* [6] pointed out that the multi-function heat exchanger-reactor concept represented significant potential for maximizing the conversion efficiency of chemical reactions in cases that would otherwise be mass transfer limited. They characterized the degree of mixing intensity in a PHE using the calibrated Walker reaction, which has two competing steps:

Step 1: $$OH^- + H^+ \rightarrow H_2O + 55.8\,kJ \tag{2}$$

Step 2: $$CH_3C(OCH_3)_2CH_3 + 18.0\,kJ \rightarrow (CH_3)_2CO + 2CH_3OH \tag{3}$$

Step 2 is catalyzed by H^+, which is consumed by step 1. Step 1 is extremely rapid and is therefore diffusion limited. Likewise, the extent of step 2 is sensitive to the degree of mixing. The products produced in step 2 are used as an indicator for the mixing intensity in a chemical

process. They developed a numerical predictive tool that was used to model the dynamics of the above process and demonstrate good agreement with their experimental characterization, which shows the high mixing intensity that PHEs are capable of generating, and thus high heat and mass transfer.

Recently, some researchers have sought to exploit the exceptional thermal performance of PHEs as a means of implementing phase change materials (PCMs) for thermal management. Ma and Zhang [7] studied the thermal-hydraulic performance of a clathrate hydrate slurry (CHS) in a PHE, specifically tetrabutylammonium bromide (TBAB). They report an experimental study of two types of TBAB hydrates, each with latent heats of approximately 200 kJ/kg and melting temperatures around 10°C. Their results for slurry flow rates of 0.1 kg/s with a hot-side temperature of 20°C showed almost 100% melting was achieved, which would translate to latent heat absorptions as high as 4.2 kW at a 21% solid TBAB loading by volume. However, the pressure drop measurements indicated substantial increase by a factor of ~1.2 - 2. Similarly, Bellas *et al.* [8] investigated the thermal performance of ice slurry consisting of a 5% propylene/water mixture in a PHE. They reported over 30% increase in the heat duty compared to chilled water over flow rates ranging from ~1 m^3/hr to ~3.5 m^3/hr, with ice loadings of 5-20% by volume. This study was conducted with hot-side fluid at a temperature of 22°C and ice particles sizes ranging from 170 to 600 μm. Large increase in pressure drops were again observed, ranging from 15-20%. However, despite the increased pumping power required for these PCM slurries and the shortcomings in energy density, these studies demonstrate the viability of using a PHE to facilitate heat transfer to a phase change material. Ammonium carbamate, in contrast, has a much higher latent heat than the materials used in these previous works (i.e., 2000 kJ/kg compared to 200 or 300). Thus, for similar ranges of thermo-hydraulic

parameters a near order-of-magnitude increase in attainable power ratings for a system of comparable size can be expected using ammonium carbamate.

The literature detailing the capabilities of PHEs demonstrate ample promise for delivering heat to a thermochemical heat sink rapidly and efficiently by enhanced mixing and high surface-to-volume ratios, while maintaining a compact footprint. Accordingly, the combination of a compact heat exchanger/reactor and a high energy density thermochemical storage material represents an important direction in thermal management research, simultaneously addressing the need for high specific heat duty systems capable of operating at low temperature. Specifically, in this study the aforementioned concept is explored by considering a PHE with ammonium carbamate slurry as the working fluid. This scientific endeavor has not yet been undertaken in the open literature to date. Hence, the scope of this study includes the development of a design tool in the form of a reduced-order model to analyze the heat and mass transfer performance of such a reactor utilizing ammonium carbamate. Such an endeavor will help to determine the feasibility for using this platform for thermal management (especially for low temperature operation) and for exploring the design space to identify the significant design parameters. Modeling the complex multi-phase flow phenomena that occur inside a PHE can be quite complicated. Hence, the numerical predictions from the model are validated experimentally. The experimental validation involves high-speed flow visualization and acquisition of pressure data. The experiments are performed to mimic a scenario that is similar to the ammonium carbamate decomposition reaction inside a commercial PHE. The experiments are designed to estimate the empirical parameters in existing momentum correlations.

To date, no studies exist that model a solid-gas reacting slurry within a PHE, nor are there any experimental studies where gas products from chemical reactions are evolved within a

liquid medium inside the heat exchanger channels. Hence the proposed study is expected to make contributions to the field of thermal-fluids sciences, particularly in the realm of multi-phase flows in the following ways:

1. Develop a novel thermal management scheme that exploits the high energy density of ammonium carbamate and the superior thermal performance of a chevron plate heat exchanger for removing high heat fluxes at temperatures suitable for electronics cooling.
2. Develop a numerical model involving coupled thermo-fluidic-chemical analysis to solve the multi-phase flow problem involving non-linear equations for combined conjugate heat transfer, mass transfer, and chemical reaction equations.
3. Provide empirical insights into the hydrodynamics of reacting two-phase flow regimes occurring inside a commercial plate heat exchanger. This approach involves utilization of both high-speed flow visualization and axial pressure measurements.

Review of Gasketed Plate Heat Exchangers

Gasketed plate heat exchangers (PHEs), or plate-and-frame heat exchangers, are a class of compact heat transfer equipment that offers several advantages over more traditional designs, such as shell and tube heat exchangers. A PHE consists of a stack of several corrugated plates separated by gaskets, shown partially assembled in Figure 1; when the stack is compressed by two heavy-duty ‘face plates’ and bolts, the spacing in between the stacked plates form the channels for fluid flow. The plate corrugations promote enhanced heat transfer by inducing complex secondary flow patterns [9]. When maintenance tasks are required, the PHE stack can be disassembled and the plates removed for cleaning and inspection. Additionally, the heat exchanger’s capacity can be adjusted by adding or removing plates, increasing or decreasing the heat transfer surface area as the application requires. For this reason, PHEs are extremely

versatile and flexible. The high surface area to volume ratio also means that PHEs will scale well for increasing heat duties.

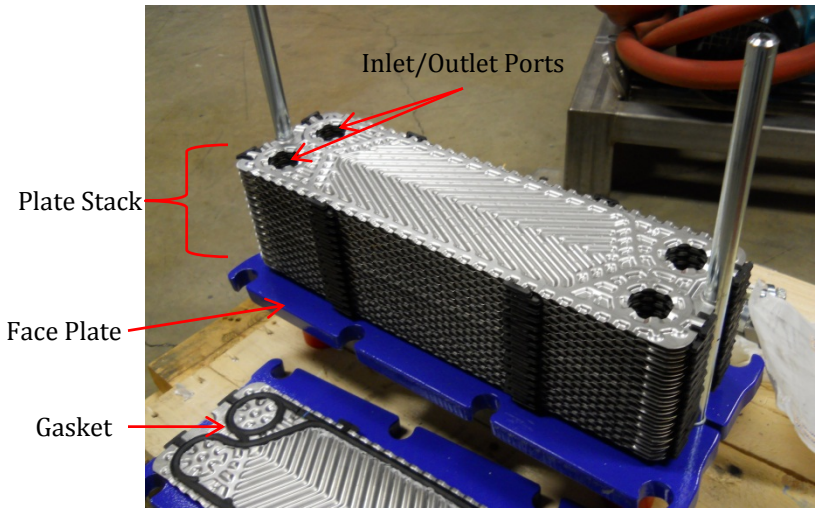

Figure 1- Photograph of plate stack assembly for Alfa Laval M3 chevron plate heat exchanger used in this study

The plates can be stamped with various corrugation geometries to enhance fluid mixing and heat transfer. The most commonly used is the chevron/herringbone pattern [10], an example of which is shown in Figure 1. Figure 2 and Figure 3 show the assembly drawing obtained by CAD (computer aided design). The CAD rendering of the two assembled plates (with a 30° chevron pattern) were formed by the two mating heat transfer plates. These figures were generated using a commercial CAD tool (SolidWorks ™, version 2012). The illustrations show how the chevron patterns on the two plates are aligned in opposite directions to create the flow channels (in the figure the upper plate pattern is rendered transparent for added clarity). The contact points where the corrugation crests from the upper and lower plate meet stabilize the

plates mechanically against differential pressure [10], so the plates can be quite thin and pose negligible resistance to heat transfer for most applications.

Figure 2 – Top view of chevron pattern overlay when a pair of heat transfer plates are stacked to form flow channels. Model rendered using SolidWorks 2012

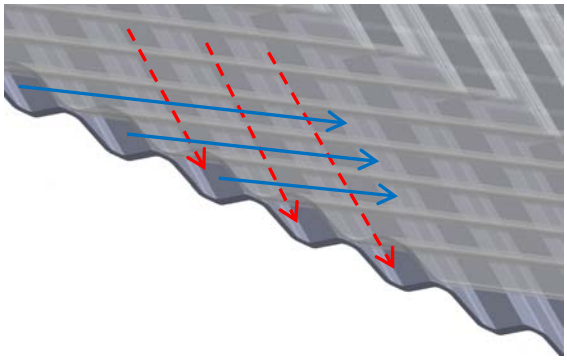

Figure 3 – Schematic illustrating crossing flow. The blue arrows represent flow traveling along the corrugation troughs on the upper plate; the dotted red arrows represent the same for the lower plate. Note that these crossing streams are occurring in the same channel

When the plates are stacked to form the channels, these corrugation patterns form a When the plates are stacked to form the channels, these corrugation patterns form a complex and tortuous network flow passages, as can be seen in Figure 3. The corrugation furrows on the upper and lower plate host crossing streams of fluid, with a free shear layer at the mid-plane region of the channel where the upper and lower plate meet. The interaction between these crossing streams produces several secondary flow phenomena, which, in addition to promoting the onset of turbulence at very low Reynolds numbers [10], give rise to remarkable enhancements in heat transfer and mixing of fluids. This occurs due to a combination of the following flow phenomena:

- A combination of flow phenomena in the corrugation furrows and flow phenomena in the wavy patterns between the upper and low plate, was described by Dović *et al.*and Focke and Knibbe as following a spiral helix path [11,12].
- At low ("soft") chevron angles (between 30° and 72° from plate axis), the flow follows a "zig-zag" path between the upper and lower plates and along the direction of their respective furrows. This causes the flow direction to be reflected to the opposite plate once it reaches the center rib or the gasket edge. For high ("hard") plate angles, a similar "zig-zag" behavior occurs, but the flow directions is reflected at the contact points between the upper and lower plate [13].
- Interaction between the aforementioned components causes boundary layer disruption and generation of Goertler vortices [12].

The presence of swirl flow and "zig-zag" paths mentioned above were noted by Shah and Focke [13] to occur regardless of the presence of turbulence, and were also cited as the

primary heat transfer enhancement mechanism in low Reynolds number flows. Thus, one may still anticipate high heat transfer coefficients, even with the lower flow rates that would be required to lengthen the residence time of the slurry, which is typically a concern for continuous flow reactors [5]. A number of plate designs were conceived and studied to maximize the aforesaid effects, some incorporating asymmetric chevron angles [14], plate combinations where the chevron angles on the upper and lower plates are different (mixed-angle plates) [15,16], and different corrugation trough profiles (e.g., sinusoidal, rounded trapezoidal, etc.) [17, 18]. Hence, multi-phase flow and heat transfer in combination with chemical reactions (for solid micro-particle slurries) during flow in PHEs were utilized in this study for their ability to enhance heat transfer at low Reynolds numbers. This is an unprecedented and complex configuration for study of transport phenomena.

The remaining part of the thesis is divided as follows: Chapter 2 provides a description of the numerical models used in this study; Chapter 3 provides a description of the experimental approach and model validation, in addition to presenting the results obtained; and Chapter 4 presents the conclusions drawn from this study and a recommended path for future work.

CHAPTER II

NUMERICAL MODEL DEVELOPMENT AND PREDICTIONS

As a first approximation to developing predictive tools for the reactor/heat exchanger system, a 1-D finite volume model for the entire heat exchanger was developed. In essence, the geometry of the plate heat exchanger is reduced to an 'equivalent' flat plate heat exchanger, where the hydraulic and thermal performance are estimated by utilizing established correlations, such as those by Focke, Martin, and others [9-11, 19]. While this simplified approach obviously cannot reproduce the complex flow effects caused by the tortuous flow passages, such an approximation is frequently employed in industry [20]; indeed, similar 1-D models have been developed by other investigators to analyze heat exchanger performance in the food industry [21].

Some investigators, such as Ciafolo *et al.* [22], and Jain and Joshi [23], among others [24, 25], have proposed high-fidelity CFD models for the case of single-phase flow in plate heat exchangers to calculate both thermal and hydraulic performance. In particular, the large eddy simulations performed by Ciafolo *et al*. showed complex, vortical 3-D secondary flow patterns for different values of chevron angles and Reynolds numbers (*Re*). The numerical computations, along with the experimental data for local temperature obtained by Gherasim *et al.* [26] and the local heat transfer coefficients obtained by Heggs *et al.* [27] , suggests that any reduced order modeling approach will need to employ empirical correlations to obtain any degree of qualitative accuracy, at the very least – there exists large deviations in the heat transfer coefficient over the unit cell formed by two crossing furrows, as well as irregularly-shaped isotherms over the width of the plate. One may easily conclude that anything less than a full 3-D simulation cannot reproduce even the single-phase hydrodynamics and heat transfer. For a useful design tool that encompasses both two-phase flow and the complex flow phenomena, and executes within a

reasonable time frame, the model must rely on empirical relations. The development of CFD models for *single-phase* flows in PHEs are to this day a very active area of research [28]. Attempts to produce a high-fidelity CFD model for a multi-phase reacting flow in a PHE are lacking in the literature, since this is a substantially more complicated problem. Hence, the sensible and cost-effective approach for modeling of transport phenomena in these multi-phase systems is to use reduced-order semi-empirical models, such as the one developed in this study.

The main limitation is the model's reliance on empirical correlations, none of which appear to encompass the specific operating conditions anticipated in this system, and do not give local heat and mass transfer information. For the purpose of demonstrating feasibility to reject a given low-quality thermal load, it may be sufficient to utilize these correlations so long as they underestimate the heat transfer, thereby yielding conservative estimates. The model's modular code allows for improved heat, mass, and momentum transfer correlations to be incorporated, which are developed in the bench-scale testing phase.

One-dimensional Model Formulation

The analysis of an "open system" reactor requires the formulation of transport equations to describe the advection and diffusion of mass and energy within the carrier fluid and a means to model the solid-gas decomposition reaction itself as a function of the independent flow variables. In the following section the aforementioned mathematical models are developed and their theoretical basis is described.

Reaction Rate Model

Kinetic models for the decomposition of ammonium carbamate are sparse in the open literature, with only two mathematical models proposed: one due to Frejacques [28], and another due to Claudel and Boulamri [29]. The latter is the best choice as a starting point, since it is the only model to be empirically substantiated; additionally, these authors showed that the kinetics postulated by Frejacques did not match their experimental findings. Claudel and Boulamri found that the decomposition and reformation of AC followed a net rate law of the form:

$$\left|\frac{dP_p}{dt}\right| = aA_p\left(P_{eq} - P\right)^2 \tag{4}$$

where, P_p is the partial pressure of the gaseous decomposition products, P_{eq} is the equilibrium pressure corresponding to the temperature at which the reaction occurs, and P is the local pressure condition. One would expect the reaction to occur when $P < P_{eq}$, and proceed in reverse when $P > P_{eq}$, assuming gaseous products are present (obviously an undesirable situation for a thermal management system). The model proposed by Claudel and Boulamri was criticized by Ramachandran *et al.* [30], who claimed that it would imply that the partial pressure of the gaseous products would increase even when $P > P_{eq}$. However, in their paper, they did not include the absolute value sign seen on the left-hand side of Equation (4), the presence of which would seem to render their criticism moot.

Even though this study was conducted on a closed system of dry powder in a known volume -- their experimental data was obtained by measuring the partial pressure in a batch reactor -- far from the dynamic conditions considered in this study, Claudel and Boulamri observed that the proposed rate law is indicative of crystal dissolution/formation, a behavior that was also observed in other gas-solid reactions. Because of the low solubility of AC in propylene glycol, it is reasonable to assume that the reaction will be primarily heterogeneous, and thus the

solid-gas mechanism implied by Equation (4) should still hold. Schmidt observed experimentally a strong dependence of the decomposition of solid AC suspended in ethylene glycol on pressure. It should also be noted that the temperature dependence of P_{eq} did not appear to be significantly affected by the presence of a liquid medium in Schmidt's experimental work, either. Hence, in the case of solid AC suspended in propylene glycol, we retain the form of the P_{eq} curve [4, 31]:

$$P_{eq}(T) = G \exp\left(-\frac{e}{T}\right) \tag{5}$$

where, G and e are constants equal to 1.9122×10^{10} kPa and 6321.7 K respectively, as obtained from [4]. Figure 4 depicts the relationship between P_{eq} and temperature as predicted by Equation (5). The plot in Figure 4 also shows the comparison between the theoretical model of Equation (5) and experimental results reported in the literature [4, 31-33] for different temperature ranges. The plots show that the predictions from the theoretical model are consistent with the experimental data reported in the literature. The dissociation pressure relation shown in Figure 4 demonstrates that the reaction rate, and hence the power rating of the reactor, can be controlled either by regulating the operating temperature or pressure of the reactor.

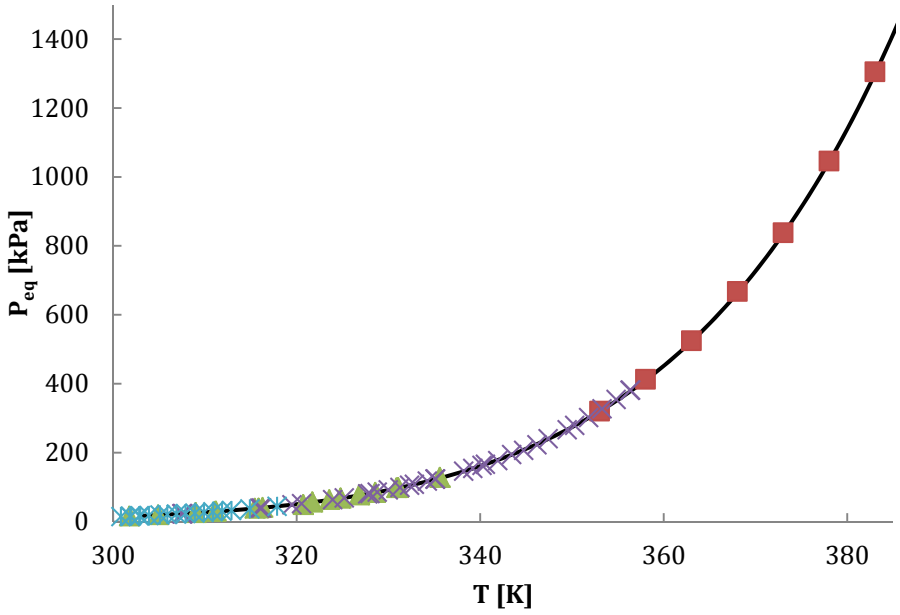

Figure 4 - Dissociation pressure P_{eq} as a function of temperature predicted by Equation (5) compared with experimental results obtained in the literature. Diamonds: Bennet et al [31]; Squares: Koutinas et al. [4]; Purple X's: Egan and Potts [32]; Blue stars: Briggs and Migrdichian [33]

Further contemplation of the dissociation pressure relation shown in Figure 4 demonstrates that the reaction rate, and hence the power rating of the reactor, can be controlled either by regulating the operating temperature or pressure of the reactor.

In order to incorporate this model into the field conservation equations of mass and energy, it is convenient to consider the reaction model on a per-unit-volume basis, as is typically done for modeling mass transfer in an Eulerian reference frame [34], where conservation of mass for a constituent species *s* is written as:

$$\frac{dC_s}{dt} = \dot{m}_s''' + \nabla \cdot \left(D_s \nabla C_s \right) \tag{6}$$

where, C_s is the concentration of the s-th chemical species (units of mass/volume), D_s is the binary diffusion coefficient for the s-th chemical species (length^2/time), and $\dot{m}_s'''$ is the volumetric rate of species generation/consumption due to chemical reaction. Of course, Equation (6) assumes a continuous concentration field for each constituent chemical species, and that said species are present in small amounts compared to the solvent. It is reasonable, however, to extend these assumptions to the ammonium carbamate suspension when one considers that the characteristic particle size to be used in the slurry is roughly 0.03 mm, which is approximately 1/100th of the channel depth. Additionally, the target mass loading per unit of slurry volume is in the neighborhood of 1g/liter, which gives a mass ratio of 1:1000. Note that 1 g of AC can absorb approximately 2 kJ of heat [2, 35], which offers a potential power rating of 2 kW at a 1 L/s slurry flow rate.

With these considerations, the reaction within the slurry may be considered, from the scale of the bulk flow, as a reacting solution in which the sizes of the AC particles are neglected. This further implies that the AC particles travel at the same velocity as the liquid, and their effects on the momentum equation may be ignored [36]. However, based on the physical mechanism implied by the kinetic model of Claudel and Boulamri, the surface area of the particles plays an important role in the rate of decomposition. To this end, we consider a single AC particle with surface area A_p, volume V_p, and density ρ_p. Assuming that the same decomposition mechanism postulated by Claudel and Boulamri exists when suspended in PG, the rate of decomposition of an individual AC particle will be proportional to the local equilibrium pressure drop and its surface area, as in Equation (5):

$$\frac{d}{dt}\left(\rho_p V_p\right) = -\kappa A_p \left(P_{eq} - P\right)^2 \tag{7}$$

The mass "concentration" of AC per unit volume of PG is:

$$C = n''' \rho_p V_p \tag{8}$$

where n''' is the number of AC particles per unit volume. It follows that the volumetric reaction rate is then

$$\dot{m}''' = -n''' \kappa A_p \left(P_{eq} - P \right)^2 \tag{9}$$

With the aim of expressing $\dot{m}'''$ in terms of C so it may be used in Equation 3, one may express particle surface area in terms of its volume; assuming that the particles are approximately spherical, the surface area is:

$$A_p = \left(4\pi\right)^{1/3} \left(3V_p\right)^{2/3} \tag{10}$$

Or, in terms of mass concentration,

$$A_p = \left(4\pi\right)^{1/3} \left(\frac{3C}{n''' \rho_p} \right)^{2/3} \tag{11}$$

Further simplification may be achieved by assuming that the number of particles per unit volume n''' is a constant depending only on the feed rate of AC particles into the reactor. There are three major conditions that must be met for this assumption to hold:

1) The particles are evenly distributed, and no agglomeration or break-up into smaller particles occur;
2) Particles do not accumulate within the reactor, nor are they completely consumed by the reaction, and;
3) Particles at a given location within the channel are subject to the same local pressure and temperature conditions.

Such an assumption is akin to a shrinking core model, where only the size of the solid particle changes; we are justified in adopting this assumption in light of the reaction rate being dependent on surface area: the number of particles may be viewed as shrinking until their surfaces are too

small to produce a reaction (A_p tends toward 0 as the reaction progresses). We may also assume an even distribution on account of the strong mixing that occurs from the secondary flows present in PHE's and the agitation produced by the gas bubbles. Subject to this assumption, one obtains the source term for the (AC) mass conservation equation:

$$\dot{m}''' = -\omega\kappa C^{2/3}\left(P_{eq} - P\right)^2 \tag{12}$$

where:

$$\omega = \left(4\pi n'''\right)^{1/3}\left(\frac{3}{\rho_p}\right)^{2/3} \tag{13}$$

Assuming $P_{eq} > P$, otherwise, the rate is simply 0, assuming no gaseous CO_2 or NH_3 are present in regions where $P_{eq} < P$, in which case the reverse reaction is expected to occur. Such a condition could only happen if the reactor back pressure is suddenly and drastically increased for a sustained time period, or if the temperature of the slurry is suddenly and drastically decreased in the same fashion. These situations are unlikely to develop if constant reactor conditions are maintained, and could therefore only plausibly arise in the case of equipment failure or other accident scenarios.

Transport Equations

Based on the assumption of very small solid AC particles suspended in the liquid heat transfer medium, the complicated solid-liquid-gas flow may be reduced to a pseudo two-phase flow in which the liquid-solid system is treated as a mixture. Figure 5 and Figure 6 show the coordinate system used to designate the channel and axial location in relation to the simplified "equivalent parallel plate" geometry used in the model. A location in the system is uniquely determined by specifying (z^*,n), where z^* is the axial location measured from the inlet and n is

the channel index. Hence, a the value of a generic, cross-section averaged flow variable Φ in the physical domain is a function $\Phi(z^*,n)$.

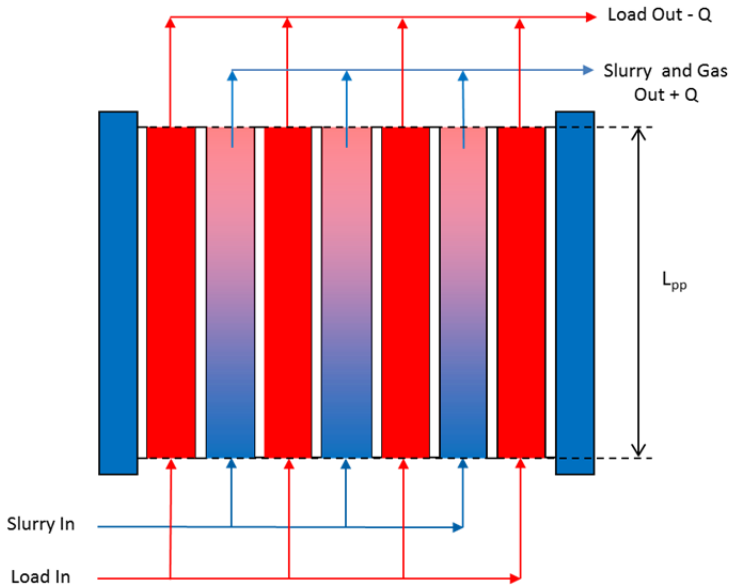

Figure 5 – Diagram of flow arrangement used for numerical simulations

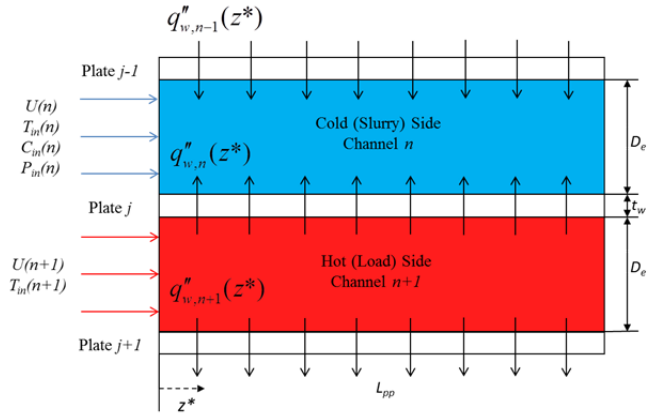

Figure 6 – Coordinate system and channel indexing scheme

The separated flow model [37] is used as the basis in formulating the conservation laws. The equations are derived by performing an integral balance of mass, momentum, and energy for both phases on a control volume of length dz^* encompassing the entire channel cross-section; a side view diagram of such a control volume is illustrated in Figure 7. Since two-phase flows exhibit random transient behavior, we assume the velocity, temperature, pressure, and concentration fields are adequately represented by time-averaged quantities whose mean values vary only in space [38].

The liquid and gas phases are assumed to be segregated (reminiscent of annular flow), each with its set of conservation equations. The void fraction, α, is herein defined as the fraction of the channel's total cross sectional area, A, occupied by the gas phase. The pressures in each phase are assumed to be equal in any given cross section ($P_l = P_g = P$).

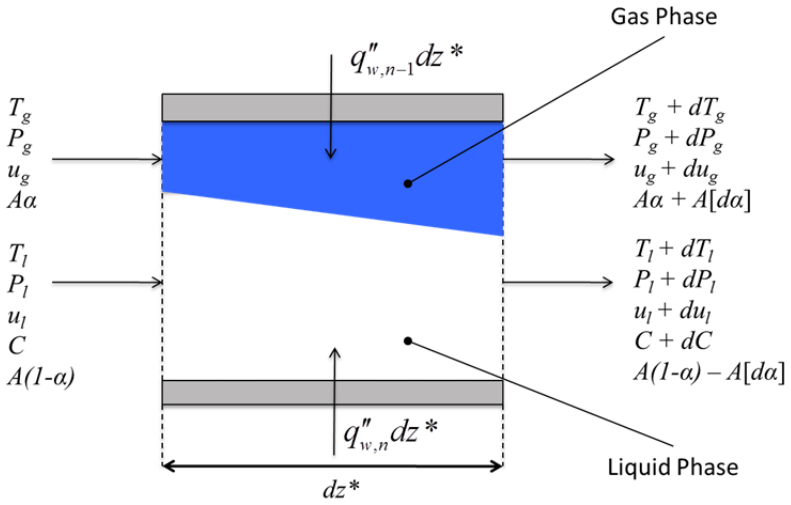

Figure 7 – Control volume for analyzing two-phase flow in 1-D model framework

The following assumptions are applied:

- The gas mixture is insoluble in the liquid phase
- No evaporation occurs in the liquid phase on the slurry side
- As previously mentioned in the discussion on decomposition rate modeling, the contribution of the suspended solids on the momentum equation is negligible.
- The flow is one-dimensional. Cross-sectional variation in the temperature, velocity, and void fraction profiles are replaced by area averaged quantities. These average quantities are permitted to differ between the liquid and gas phases. Since heat flux and friction information are obtained from experimental correlations, cross-sectional variation in the flow variable fields need not be considered --- this simplification is typical of heat exchanger analysis methods, such as the LMTD or ε-NTU methods [20].
- In developing the energy equation, it is assumed that heat transfer to the gas phase is negligible when compared to heat transferred to the liquid phase and suspended AC. This assumption may be justified in light of the short residence time of the fluid within the heat exchanger, as well as the low value of temperature difference (between the hot side and the cold side ~30°C) and the comparatively low thermal conductivity of the gas phase.
- The reaction is assumed to occur predominately at the local bulk temperature. The reason for this approximation is the high degree of mixing resulting from gas generation and transit while the reaction is underway. By analogy to turbulent flow in a duct, this effect will tend to produce a fairly uniform time-averaged distribution of temperature and AC concentration, leaving only a thin film of fluid near the plate surface, which is close to the wall temperature. Therefore, only a small portion of the suspended AC would deviate from the bulk temperature.

- Axial conduction is negligible, since the Péclet (*Pe* = *RePr*) number is >100 for all test cases for pure propylene glycol as the heat transfer fluid. Using property data for propylene glycol furnished by Sun *et al.* [39], and assuming a flow rate of 5 liters per minute, one may compute *Pe* as follows:

$$\mathrm{Re} = \frac{\dot{V}\rho_{ls}}{W\mu_{ls}N} = \frac{\left(1.67\cdot 10^{-5}\,\frac{m^3}{s}\right)\left(1036\,\frac{kg}{m^3}\right)}{7\left(0.040Pa\cdot s\right)\left(0.1m\right)} \simeq 3 \tag{14}$$

$$Pe = \mathrm{Re}\,\mathrm{Pr} = \left(3\right)\left(510\right) \simeq 1500 \tag{15}$$

where, *N* is the number of channels, $\dot{V}$ is the total volume flow rate into the exchanger (currently limited to ~5 liters per minute by the benchtop experiment's pump displacement), and *W* is the total width of between the gasket available for flow. The viscosity, density, and Prandtl number are obtained for a reference temperature of 30° C, since *Re* is the lowest for this value of temperature.

Conservation of Mass

Assuming steady-state operation, conservation of mass requires that:

$$\frac{d}{dz^*}\left(u_{ls,n}\rho_l\left(1-\alpha_n\right)\right) = 0 \tag{16}$$

$$\frac{d}{dz^*}\left(u_{ls,n}C_n\left(1-\alpha_n\right)\right) = -\dot{m}_n'''\left(1-\alpha_n\right) \tag{17}$$

$$\frac{d}{dz^*}\left(u_{g,n}\rho_{g,n}\alpha_n\right) = \dot{m}_n'''\left(1-\alpha_n\right) \tag{18}$$

where it is assumed that the suspended AC remains within the liquid phase, and thus the source term represents the volumetric gas generation rate per unit volume of *liquid phase* in the control volume. This is the reason for the term *(1-α)* being present on the right-hand-side of Equations

(16) and (17), since the volume of liquid within a control volume of length dz^* is given by $(1-\alpha)dz^*$.

Since the liquid phase is incompressible, Equation (16) may be integrated from the inlet to an arbitrary downstream location z^* to relate the liquid velocity at the inlet to the void fraction and liquid velocity at location z^*:

$$u_{ls,n} = \frac{U_{ls,n}}{1-\alpha_n} \tag{19}$$

Similarly, Equations (17) and (18) may be combined and integrated to obtain:

$$u_{g,n} = \frac{U_{ls,n}\left(C_{in,n} - C_n\right)}{\rho_{g,n}\alpha_n} \tag{20}$$

Conservation of Linear Momentum

For consistency with the two-phase flow literature, the momentum equation is rendered in terms of acceleration, gravity, frictional and total pressure gradients [29]:

$$\frac{dP_n}{dz^*} = \frac{dP_{F,n}}{dz^*} + \frac{dP_{G,n}}{dz^*} + \frac{dP_{A,n}}{dz^*} + \dot{m}'''_n(1-\alpha_n)\left(u_{ls,n} - u_{g,n}\right) \tag{21}$$

where the acceleration pressure drop is given by:

$$\frac{dP_{A,n}}{dz^*} = u_{ls,n}\rho_{ls}\left(1-\alpha_n\right)\frac{du_{ls,n}}{dz^*} + u_{g,n}\rho_{g,n}\alpha_n\frac{du_{g,n}}{dz^*} \tag{22}$$

and the gravity pressure drop is given by:

$$\frac{dP_{G,n}}{dz^*} = g\left[\left(1-\alpha_n\right)\rho_{ls} + \alpha_n\rho_{g,n}\right] \tag{23}$$

The 4th term on the right-hand side of Equation (21) represents the acceleration that the evolved gas must undergo, assuming it is traveling at the liquid phase velocity when it is produced; this is mathematically equivalent to gas traveling at the liquid velocity being "injected" into a gas stream traveling at velocity u_g, and does not explicitly account for the complex interaction

between the phases resulting from gas generation, such as bubble growth, coalescence and bifurcation. There appears to be no correlations available in the literature to accomplish this.

The frictional pressure drop term, dP_F / dz^*, accounts for the total fluid/gas interaction with the wall over the entire channel perimeter at location *z**. This term is expressed in terms of a single-phase friction factor, *f*, and corresponding two-phase multiplier, Φ_{TP}^2, defined as:

$$\Phi_{TP,n}^2 = \frac{\left(\frac{dP_n}{dz^*}\right)_{F,TP}}{\left(\frac{dP_n}{dz^*}\right)_{F,SP}} \tag{24}$$

where the subscript *F, TP* denotes the two-phase frictional pressure drop, and *F, SP* is the frictional pressure drop of some reference single-phase flow, for which the friction factor may be readily determined. The single-phase friction factor may be that of the flow considered as consisting of the liquid phase alone at the same total mass flow rate, the liquid phase alone at its respective mass flow rate, or the gas phase alone at its respective mass flow rate; these are designated, respectively, with the subscripts *lo, l,* and *v* in both [37] and [38]. The choice of how to represent the single-phase friction factor in this model depends on the correlations selected to estimate Φ_{TP}^2. For the sake of this analysis, we will express the frictional pressure drop in terms of f_{ls} and Φ_{TP}^2:

$$\frac{dP_{F,n}}{dz^*} = \frac{\left(f \rho U^2\right)_{ls,n}}{2D_h} \Phi_{TP,n}^2 \tag{25}$$

Because of the pressure dependence of AC decomposition, modeling this term is important in predicting how the decomposition varies along the heat exchanger channel. Since the pressure is only a concern on the slurry side, no attempt is made to compute the pressure distribution on the load side.

Conservation of Energy

Conservation of energy in the liquid phase, assuming energy transfer to the gas phase to be negligible, is given by a balance of convection, wall heat flux, and the volumetric endothermic reaction in channel *n*:

$$U_{ls,n}\frac{dT_n}{dz^*} = -\frac{\Delta H}{\rho_{ls}c_{p,ls}}\dot{m}'''_n\left(1-\alpha_n\right) + \frac{q''_n + q''_{n-1}}{D_e\rho_{ls}c_{p,ls}} \tag{26}$$

where, ΔH is the enthalpy of decomposition per unit mass, $c_{p,ls}$ is the specific heat capacity of the liquid phase on the slurry side, q''_n is the heat flux to/from the lower plate, and q''_{n-1} is the heat flux to/from the upper plate. For the load fluid side, Equation (25) simply becomes:

$$U_{ld,n}\frac{dT_n}{dz^*} = \frac{q''_n + q''_{n-1}}{D_e\rho_{ld}c_{p,ld}} \tag{27}$$

As with the two-phase multiplier, the wall heat flux terms are estimated using existing correlations, depending on the flow conditions.

Inlet and Outlet Conditions

The inlet pressures, inlet temperatures, mass flow rates, and AC feed rate are presumed known and provided as inputs to the solver; they may be specified independently for each channel, if the user desires to account for flow maldistribution. The inlet conditions ($P_{in,n}$, $U_{l,n}$, $C_{in,n}$, $T_{in,n}$) along with the flow direction for each channel (i.e., parallel flow or counter flow) are stored as a vector with *N* elements, with each entry corresponding to a specific channel *n*. Since the governing equations are first order in the axial direction, no outlet condition needs to be specified.

Plate Surface Conditions

The face plates (see Figure 5) are assumed adiabatic, since they are approximately 20 mm thick compared to the 0.5 mm thick heat transfer plates. The heat flux through the plate is assumed to be 1-dimensional and in the direction of the plate surface normal since the plates are approximately thin compared to their length and width; for the heat exchanger used in this study, the plate thickness is 0.5 mm, and the material is 316 stainless steel, which has a thermal conductivity of 13.4 W/m/K [40]. With this simplification, the heat flux between channel *n* and channel *n-1* through plate *j* between them, as illustrated in Figure 6, may be computed using the overall heat transfer coefficient h_{eff}:

$$q''_{n-1} = \left[\frac{1}{h_n} + \frac{t_{plate}}{k_{plate}} + \frac{1}{h_{n-1}} \right]^{-1} \left(T_{n-1} - T_n \right) = h_{eff,n-1} \left(T_{n-1} - T_n \right) \tag{28}$$

where, T_n and T_{n-1} are the bulk fluid temperatures of channels *n* and *n-1* respectively, k_{plate} is the thermal conductivity of the plate material, and t_{plate} is the plate thickness. Similarly, h_n and h_{n-1} are the convection coefficients on the side of channels *n* and *n-1*, respectively. This relation essentially serves as the "link" between channels.

Non-dimensional Transport Equations

Transforming the governing equations to a non-dimensional form reveals the relevant parameters that influence the model. If one introduces the following dimensionless variables,

$$\theta_n = \frac{T_n}{\left(\frac{\Delta H C^+_{in}}{\rho_{ls} c_{p,ls}} \right)} \tag{29}$$

$$\eta_n = \frac{C_n}{C^+_{in}} \tag{30}$$

$$z = \frac{z^*}{L_{pp}} \tag{31}$$

$$\upsilon_n = \frac{U_n}{U^+} \tag{32}$$

$$Da = \frac{\omega \kappa L_{pp}}{C_{in}^{+1/3} U_{ls}^+} \left(P_{eq}(T_{ld,in}^+) - P_{atm} \right)^2 \tag{33}$$

$$\varphi_n = \frac{h_{eff,n} L_{pp}}{D_e \left(U^+ \rho c_p \right)_{ls}} \tag{34}$$

$$R = \frac{\left(U^+ \rho c_p \right)_{ls}}{\left(U^+ \rho c_p \right)_{ld}} \tag{35}$$

$$\dot{M}_n''' = \begin{cases} \eta_n^{2/3} \left[\dfrac{P_{eq}(T_n) - P_n}{P_{eq}(T_{ld,in}^+) - P_{atm}} \right]^2 & P_{eq} > P \\ 0 & P_{eq} \le P \end{cases} \tag{36}$$

where the $^+$-superscript signifies that the variable is evaluated at the inlet as if there were no maldistribution present (e.g., $U_{ls}^+ = \dot{V}_{slurry,total} \big/ N_{slurry} D_e W$). Thus, the parameter υ is a measure of the degree of flow maldistribution in a given channel. The energy and mass conservation equations for the slurry side in a given channel n, respectively, become:

$$\upsilon_{ls,n} \frac{d\theta_n}{dz} = -Da \dot{M}_n''' (1 - \alpha_n) + \varphi_n \left(\theta_{n+1} - \theta_n \right) + \varphi_{n-1} \left(\theta_{n-1} - \theta_n \right) \tag{37}$$

$$\upsilon_{ls,n} \frac{d\eta_n}{dz} = -Da \dot{M}_n''' (1 - \alpha_n) \tag{38}$$

And for the load side:

$$\upsilon_{ld,n} \frac{d\theta_n}{dz} = R_n \left[\varphi_n \left(\theta_{n+1} - \theta_n \right) + \varphi_{n+1} \left(\theta_{n-1} - \theta_n \right) \right] \tag{39}$$

Three dimensionless groups are obtained by this procedure, a Damköhler number (*Da*), φ, and heat capacity rate ratio (*R*). The Damköhler number represents the ratio of the characteristic time scales of chemical reaction to advection, or reaction rate to residence time. Consequently, small *Da* are indicative of operating conditions where the AC feed rate is too high to achieve complete conversion; large *Da* are indicative of operating conditions where the AC feed rate is insufficient to realize maximum heat rejection (i.e., complete conversion long before the slurry exits the channel). The dimensionless group φ serves as an indicator of energy transport between the plates to energy transfer by advection in the bulk flow. Lastly, *R* relates the magnitude of temperature change in the load side to the slurry side; for cases where the heat capacity rate on the load side is significantly higher than that of the slurry side, $R \rightarrow 0$, and consequently the load side temperature may be approximated as isothermal.

Pressure Drop Correlations

Due to the pressure dependence of the reaction rate model, the frictional pressure drop is expected to accelerate the decomposition as the slurry progresses downstream by way of increasing the $(P_{eq} - P)^2$ driving force. It is therefore imperative to accurately compute the hydraulic performance on of plate heat exchangers. The following section is a survey of presently available empirical and semi-empirical correlations for predicting the pressure drop of PHEs as a function of geometry, fluid properties, and flow rates.

Single-phase Flow

In the area of single phase flow within a plate heat exchanger, many correlations for various ranges of *Re* and plate geometries have been proposed. Before discussing the data available in the open literature, it is instructive to define the geometric parameters typically used to characterize the plate and corrugation pattern – the scope is limited to plates having the chevron/herringbone pattern with sinusoidal corrugations, since this is the type of plate used in the benchtop experiment, and the chevron type is the most widely used [13]. Figure 8 shows the top view of an Alfa Laval M3 plate with a 30° chevron angle measured from the main flow direction; the gasket restricts the flow to within the corrugation confines and directs it toward the appropriate port while the distribution zones ensure that the flow is allocated evenly over the width of the corrugated section. Figure 9 shows a side view of the corrugation pattern in a typical chevron PHE, looking directly down the furrow, to define the pitch and depth parameters. It should be noted here that the precise geometry of the corrugation troughs differs by manufacturer, the specific details being proprietary.

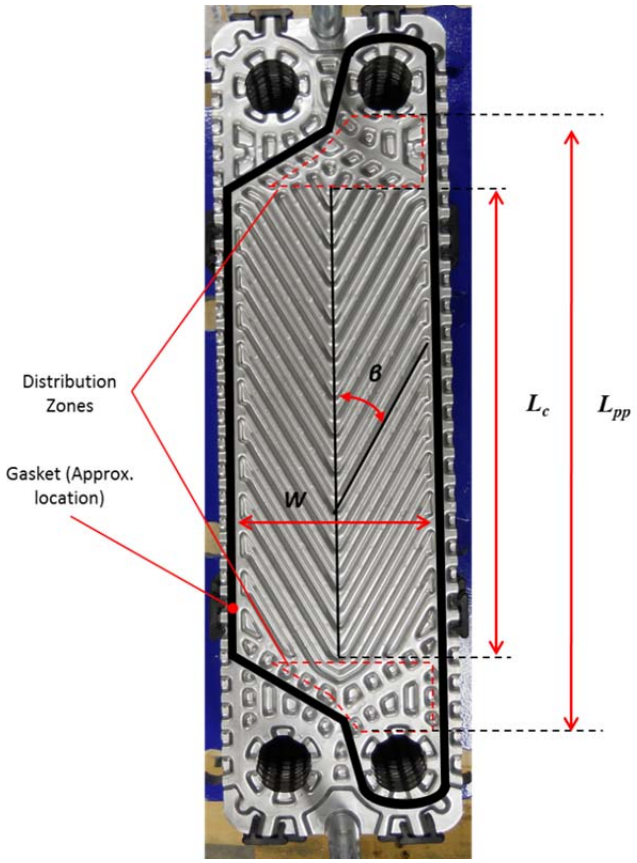

Figure 8 – Anatomy of the Alfa Laval M3 plate used in this work. The gasket location on plate periphery was drawn to facilitate reader understanding

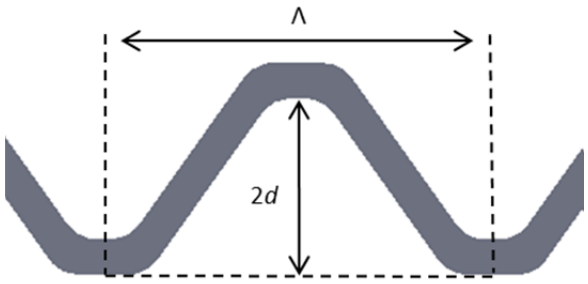

Figure 9 – Side view of typical corrugation pattern showing wavelength and height parameters

There are two popular ways to define *Re* for PHEs*:* based on the actual plate surface area used in the definition of the hydraulic diameter (four times the ratio of the fluid volume to the wetted surface area), or based on the projected plate surface area [13]. The equivalent diameter, D_e , uses the projected area of the plate (i.e., L_cW), and is simply equal to $4d$; the alternative definition, designated D_h, uses the actual plate surface area, and is related to the equivalent diameter by $D_e = D_h / \Phi_{AE}$, where Φ_{AE} is the "area enlargement factor" – the ratio of the actual surface area to the projected surface area [34]. Φ_{AE} may be approximated by a three-point integration formula for sinusoidal corrugations employed by Martin [41]:

$$\Phi_{AE} \cong \frac{1}{6}\left[1+\sqrt{1+\hat{X}^2}+4\sqrt{1+\hat{X}^2/2}\right] \tag{40}$$

where $\hat{X} = 2\pi d/\Lambda$ is a dimensionless parameter that defines the corrugation aspect ratio. Since there is no theoretical justification for using the actual surface area in lieu of the projected surface area, many researchers use the equivalent diameter for the sake of convenience [13].

As previously mentioned, there are a multitude of single phase friction factor correlations available, a summary of which has been compiled by Thonon [42] in 2004. Most appear to be applicable to a specific set of plate geometries, fluids, and/or flow conditions. For instance, Muley *et al.* [43] observed substantial differences between the work of Focke *et al.* [10], and Thonon *et al.* [44], even for the same chevron angles; This discrepancy was attributed to the different area enlargement factors and corrugation aspect ratios studied by these two authors. Thonon [42] also compares several studies that developed correlations from industrial plates with those that used only corrugated passages – the difference being that the correlations for industrial plates include the port-to-port pressure drop (which includes the distribution zones leading into the corrugated section), whereas the other studies considered only the length of the plate containing the chevrons. From this, Thonon concludes that "accurate estimation of the

pressure drop cannot be obtained from general correlations, and that specific studies need to be performed on every type of plate heat exchangers" (*sic*).

While the lack of a generally applicable pressure drop correlation is an obstacle to developing an accurate predictive model for a variety of PHE configurations, the choice of available correlations in the literature may be narrowed by the following consideration: the reaction is expected to occur within the corrugated section, so correlations developed from corrugated model passages are the more attractive option. A more realistic approach would be to divide the total pressure drop into contributions from the corrugated section and the inlet/outlet distribution geometry.

Additionally, there are only a few studies (for example, [10, 41-46]) that correlate data for low *Re* (<1 to 10), which will be representative of the operating conditions of the slurry side of the PHE, due to both the high viscosity of propylene glycol at the operating temperatures, and the flow rate limitations of the experimental apparatus. Of the models that were not proprietary and/or limited to a single model of chevron PHE, two promising leads were found for a widely applicable model at low *Re*. Fernandes *et al.* performed numerical studies for the hydraulic behavior of chevron PHEs having sinusoidal corrugations in the low *Re* regime (fully-developed laminar flow) based on an analogy to porous media [46]. Accordingly, these authors posit a friction factor correlation of the form $f = K\,Re^{-1}$, with $K = K_o\,\tau^2$ being Kozeny's coefficient; a commercial CFD code was used to compute Kozeny's coefficient for $1.1 < \Phi_{AE} < 1.5$ and $29° < \beta < 60°$, and the following relationships for the tortuosity coefficient, τ, and the shape factor, K_o, were proposed

$$\tau = 1 + 0.5\sqrt{\left(\frac{1}{\sin(90-\beta)}\right)^{\gamma} - 1} \tag{41}$$

$$K_o = 16\left(\frac{90}{90-\beta}\right)^{0.6554-0.0929\gamma} \tag{42}$$

where, $\gamma = 4b/\Lambda\cos(\beta)$ defines the ratio of the corrugation depth to the pitch projected in the main flow direction. The numerical calculation was validated by comparing the predicted value of K for a double sine duct ($\beta = 0$) to that of Ding and Manglik [47], and the results differed by less than 1%; the analytical model reproduced the numerical calculations to within 3.5%. It should be noted, however, that the CFD model used in their study assumed perfect contact between the upper and lower plates, and flow symmetry with neighboring unit cells along the channel width.

Another semi-empirical model is offered by Martin [41], and decomposes the friction factor contributions into flow reversals, the crossing of streams following the upper and lower furrows, and the increased effective flow length. Martin develops his model based on the flow pattern observations of Focke *et al.* [10] and Gaiser [48], which showed that two types of flow exist simultaneously: flow with crossing streams that follows the furrows of the lower and upper plate – "crossing flow", in Martin's vernacular -- and flow that follows a sinusoidal wavy pattern. Martin postulated that, when driven by a common pressure gradient, the relative contribution to the total flow rate by each type of flow is proportional to their respective projected cross-sectional areas, since the latter dominates at high β, while the former dominates at low β. Two limiting cases are considered to illustrate this point: when $\beta = 0$, a collection of straight, parallel double-sine ducts like that which was studied by Ding and Manglik is formed; when $\beta = 90°$, a wavy passage like that which was studied by Metwally and Manglik [49] and Rush *et al.* [50] is formed. For intermediate angles, the friction factor contribution from the

crossing flow conforming to the furrows is proportional to *cos(β)*, while the sinusoidal wavy-flow contribution is proportional to *1-cos(β)*. The resulting model reads:

$$\frac{1}{\sqrt{f}} = \frac{\cos\beta}{\sqrt{b\tan\beta + c\sin\beta + f_0\cos\beta}} + \frac{1-\cos\beta}{\sqrt{3.8 f_1}} \tag{43}$$

where the friction factor for flow in a straight duct of sinusoidal cross section is:

$$f_0 = \begin{cases} \dfrac{B_0}{\mathrm{Re}} & \mathrm{Re} < 2000 \\ \left(B_1 \ln\left(\mathrm{Re}\right) + B_2\right)^{-2} & \mathrm{Re} \geq 2000 \end{cases} \tag{44}$$

The friction factor for a wavy duct following a sinusoidal path (with a phase shift of π/2 between the upper and lower plates) is:

$$f_1 = \begin{cases} \dfrac{K_1}{\mathrm{Re}} + K_2 & \mathrm{Re} < 2000 \\ \dfrac{K_3}{\mathrm{Re}^m} & \mathrm{Re} \geq 2000 \end{cases} \tag{45}$$

The constants *B* and *K* in the above two equations are functions of the corrugation shape and aspect ratio *Λ/2d*. This model can be seen to give the correct asymptotic values for the cases discussed above. Note that the two additional terms [*b tan(β)*] and [*c sin(β)*] approximately account for two additional frictional contributions that occur in crossing flow:

1. The flow following the upper furrow crosses the flow following the lower furrow, and will tend to induce secondary helical motion in both flow streams. The strength of this secondary flow effect arises from one substream possessing a velocity component that is perpendicular to the direction of the other substream it crosses [10, 51]; the constant *c* is defined as:

$$c = f_c \frac{2D_h}{\Lambda} \tag{46}$$

where f_c is a friction factor associated with the crossing substreams, which Martin assumes to be constant.

2. A sub-stream that follows the furrow along one plate will experience an abrupt change in direction when either the center of chevron pattern or the edge of the plate is encountered, and subsequently follows the furrow of the opposite plate. The constant b is defined as:

$$b = f_b \frac{2D_h}{W} \tag{47}$$

where f_b is a friction factor associated with the flow reversal, and as in the case of crossing substreams, is assumed constant.

The fact that Martin's correlation provides a means to account for secondary flow phenomena, at least approximately, and grants consideration to the experimentally observed overall flow structure (i.e., the simultaneous existence of furrow and longitudinal wavy flow) affords a wide range of applicability that makes it an attractive option to incorporate into the model. The largest obstacle in this case is finding reasonable values for the constants b and c (including the parameters in f_o and f_1) that would encompass the desired operating range and geometry of a typical PHE slurry reactor. Table 1 gives the values for empirical constants used in his correlation, which matched data for the turbulent flow regime well:

Table 1 – Constants used in Equations (43)-(45)

b	0.18	K_1	597
c	0.36	K_2	3.85
B_0	64	K_3	39
B_1	1.8	m	0.289
B_2	-1.5		

Due to the lack of any demonstrably better parameters to choose for the low-*Re* conditions expected in this study, the values stated above were used. In fact, Dović *et al*. [51] compared Martin's model to pressure drop measurements obtained from a PHE with $\beta = 28°$ and $2d / \Lambda \approx 0.28$) and "found good agreement (10%) for $Re < 50$".

It is noted here that Martin's correlation does not predict the early transition to turbulence that have been observed to occur in PHEs, which can occur at *Re* as low as 10 for high chevron angles [45]. The onset of transition will depend on the specific plate geometry, including the chevron angle, the corrugation aspect ratio, and the corrugation shape, which vary by manufacturer. Ciafolo *et al*.'s [22] numerical results suggest that the secondary flows (*e.g.*, swirl flow and Goertler vortices) have a much greater effect on the heat transfer coefficient than fluid turbulence for *Re* around 2000. Therefore, for low *Re*, as long as the secondary flow mechanisms are accounted for, the assumption of laminar flow is a reasonable approximation. Lacking a general model to reliably predict the transition to turbulence as a function of PHE geometric parameters the flow is assumed laminar during single-phase flow.

Two-phase Flow

Much of the literature focusing on two-phase flow in PHEs centers on the characterization of thermo-hydraulic performance of refrigerants in boiling and condensation, which are summarized by García-Cascales *et al.* [52]. While the correlations and findings of these works would not be applicable to the gas and liquid flow on the slurry side of the reactor, it is worth mentioning that the working fluid on the load side need not be restricted to a single phase fluid, and that it may be fruitful to investigate the potential advantages of employing a condensation process in the future since it would be easier to adjust the temperature at which heat is rejected and thereby also control the reaction rate.

The most reasonable parallel that exists between the reacting flow expected to occur in the system (used in this study) and the experimental studies reported in the open literature is that of two-phase air and water flow. Within the reacting flow, the presence of the gas phase is not linked to vaporization or condensation of the liquid phase – the two phases may be regarded as separate entities that only interact mechanically and through thermo-chemical reactions. The liquid temperature will change during the course of AC decomposition as the suspended AC absorbs sensible heat from the surrounding fluid in accordance with its reaction rate, whereas in condensation or boiling the phase change occurs at constant temperature. Since both of these key differences can be realized in the case of air-water two-phase flow (if one were to perhaps inject air continuously in the bulk of the liquid phase and along the length of heat exchanger channel), it is reasonable to assume that similar hydrodynamic conditions will exist in the reactor. This is tantamount to assuming that the predominant mechanism responsible for increased flow friction are the eddies and other secondary flow structures due to the passage of bubbles. Taking these observations into account, the local pressure drop should depend on the void fraction, the flow quality, the flow pattern, and the rate of gas production by AC decomposition. All but the last of

these dependencies may be estimated by applying the correlations developed for air-water flow, although the model will need to allow for changes in flow regime (and hence, void fraction prediction method) to occur as the total amount of gas phase present within the flow increases.

Experimental studies in air-water two-phase flow were conducted by Shiomi *et al*. [53] for symmetric and asymmetric combinations of chevron plates with angles of 30° and 60°, with both horizontal and vertical upflow and downflow configurations, and correlated their results with the Chisholm method [37]. They observed that the bubbles followed zig-zag patterns characteristic of single-phase flow, and that the bubble size tended to increase with increasing liquid flow rates.

Kreissig and Müller-Steinhagen [54] experimentally characterized air-water two-phase flow for two types of PHEs, one of which used chevron-patterned plates with a 60° chevron angle. For several total mass fluxes and qualities, the overall port-to-port pressure drop data was collected and compared to several two-phase friction factor correlations that were developed for conventional tubes. Of the correlations tested, the Dukler [55] correlation was found to give the best agreement, although it did still overestimate the overall pressure drop. It is interesting to note that the Dukler correlation is based on the homogenous flow model, which the authors noted was increasingly advantageous at higher mass fluxes; they suspected that the tortuous flow passages kept the two-phase flow from forming heterogeneous flow patterns. However, in a later flow visualization experimental study by Vlasogiannis *et al*. [56], which used the same PHE model and downward vertical flow orientation, large gas-continuous regions and slug-type flow patterns were observed, contrary to the aforementioned hypothesis.

Tribbe and Müller-Steinhagen [57] tested the pressure drop in air-water two-phase flow for symmetric and asymmetric plate combinations having chevron angles of either 30° or 60°, and corrugation depths of 2 or 3 mm. In a follow-up paper [58], the same authors used their

pressure drop data to develop a correlation for the two-phase frictional multiplier for flow in the corrugated section of the channel, which correlates the data for all the geometries and mass fluxes used in their experiments:

$$\Phi_{TP} = 1.423 - 0.0724 \ln X + \frac{1.031}{X} \tag{48}$$

where the Lockhart-Martinelli parameter X expresses the ratio of the frictional pressure gradient of the liquid phase flowing alone to that of the gas phase flowing alone at their respective superficial velocities:

$$X = \sqrt{\left(\frac{dP}{dz}\right)_{F,l} \Big/ \left(\frac{dP}{dz}\right)_{F,g}} \tag{49}$$

This correlations is claimed to be valid within $0.06 < X < 10$. The authors argue that the fact that the normalized two-phase frictional pressure drop for flows involving different chevron angles, channel gaps, and fluid viscosities, can be well represented by a single curve indicates that the influence of geometry on the two-phase frictional pressure drop is accounted for by the single phase friction factor – at least in the corrugated section. Another important observation made by the authors is that Equation (48) may be applied locally in a "stepwise manner" to reproduce the total pressure drop to within 4%, even though it was derived using total pressure drop over the entire corrugated section, and average absolute pressure. This has several major implications for the present model

- Equation (48) is applicable to most PHEs, and the higher viscosity of the propylene glycol will not have a drastic effect on its accuracy.
- Equation (48) may be used to find the local pressure drop in the corrugated section, assuming that an appropriate single-phase friction factor correlation is used to account for geometric effects.

The overall single-phase friction factor, as supplied by the appropriate correlation(s), may also be applied locally within the corrugated section. This re-affirms the quasi-equilibrium approach to estimating local field variable changes in the 1D model. As a starting point, the model employs the correlation proposed by Tribbe and Müller-Steinhagen to predict the two-phase multiplier.

Void Fraction Correlations

Additional correlations are required to estimate the void fraction, which is used in computing the source term as can be seen in Equations (37) and (38) . Following the recommendation in [55], the Rouhani correlation was chosen to begin, since the referenced study used the same model of PHE used in the experimental program of this study. This correlation reads [59]:

$$\alpha_n = \frac{x_n}{\rho_{g,n}}\left\{\left[1+0.12\left(1-x_n\right)\right]\left(\frac{x_n}{\rho_{g,n}}+\frac{1-x_n}{\rho_{ls}}\right)+\frac{1.18}{\dot{m}''_{total,n}\rho_{ls}{}^{0.5}\left[g\sigma\left(\rho_{ls}-\rho_{g,n}\right)\right]^{0.25}}\right\}^{-1} \quad (50)$$

where, again the assumption is invoke that the correlations may be applied locally to calculate the total mass flux and mass quality,

$$\dot{m}''_{total} = U_{ls,n}\left[\rho_{ls}+C_{in,n}(1-\eta_n)\right] \quad (51)$$

$$x_n = \frac{1-\eta_n}{\frac{\rho_{ls}}{C_{in,n}}+1-\eta_n} \quad (52)$$

Another possible approach is through the so-called drift-flux model [60], which (empirically) accounts for the relative motion between the gas and liquid phases. It may be written for the 1-D model after Collier and Thome [37]:

$$\alpha_n = \frac{\varepsilon_n}{C_o + \frac{u_{gj,n}}{j_n}} \tag{53}$$

where ε is the volumetric quality, u_{gj} is the weighted mean drift velocity, j is the total volumetric flux (gas and liquid phase combined), and C_o is an empirical correction factor. These variables are defined as:

$$\varepsilon_n = \frac{\dot{V}_{g,n}}{\dot{V}_{g,n} + \dot{V}_{ls,n}} = \frac{1-\eta_n}{\rho_{g,n}/C_{in,n} + 1 - \eta_n} \tag{54}$$

$$u_{gj,n} = u_{g,n} - j_n \tag{55}$$

$$j_n = U_{ls,n} + U_{g,n} = U_{ls,n}\left[1 + \left(1-\eta_n\right)\frac{C_{in,n}}{\rho_{g,n}}\right] \tag{56}$$

For this case, the most appropriate parallel is bubbly vertical upward flow, for which Collier and Thome recommend the following:

$$C_0 = 1.0 \tag{57}$$

$$u_{gj,n} = 1.53\left(1-\alpha_n\right)^2\left[\frac{g\sigma\left(\rho_{ls} - \rho_{g,n}\right)}{\rho_{ls}^2}\right]^{0.25} \tag{58}$$

After substituting the above and re-arranging, one obtains a complex implicit relation for the drift flux:

$$\alpha_n = \frac{\left(1-\eta_n\right)}{\left(\frac{\rho_{g,n}}{C_{in,n}} + 1 - \eta_n\right)}\left\{1 + \frac{1.532\left(1-\alpha_n\right)^2}{U_{ls,n}\left(1 + \left(1-\eta_n\right)\frac{C_{in,n}}{\rho_{g,n}}\right)}\left[\frac{\sigma g\left(\rho_{ls} - \rho_{g,n}\right)}{\rho_{ls}^2}\right]^{0.25}\right\}^{-1} \tag{59}$$

These correlations are compared in Figure 10 for a liquid superficial velocity of 0.06 m/s (approximately that which was achieved during the flow visualization experiments) for different

values of C_{in}. The drift flux model predicts more rapid increases in void fraction with respect to conversion in comparison to the Rouhani correlation; both exhibit nearly linear growth for lower AC mass loadings. The drift flux model is, comparatively, more sensitive to AC mass loadings; the high void fraction predictions at only 20% to 40% conversion are suspect, as this would imply there are few obstacles to bubble coalescence, which is certainly not the case in the tortuous flow passages in a PHE. With this consideration, it is more reasonable to expect a gradual rise in void fraction with respect to conversion. Hence, the model employs the Rouhani correlation to provide void fraction estimates.

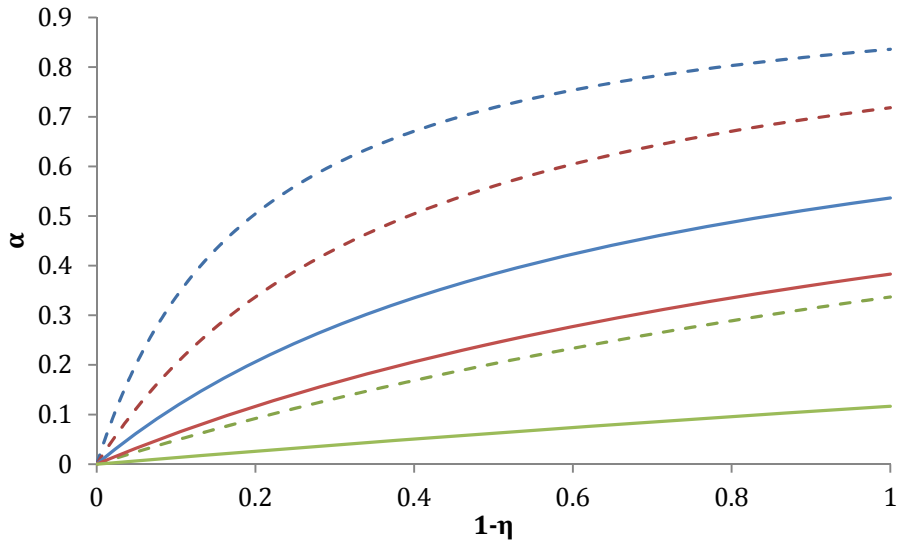

Figure 10 – Comparison of Rouhani correlation (solid lines) and drift flux model for vertical bubbly flow (dashed lines) for different C_{in}: 1 kg/m^3 (green), 5 kg/m^3 (red), and 10 kg/m^3 (blue)

For estimating the void fraction values, alternate correlations are not available in the open literature for PHEs that are considered in this study.

Heat Transfer Correlations

Of even greater importance to the fidelity of the model are correlations that will relate the flow conditions, heat exchanger geometry, and fluid properties to the convection coefficient. Since the decomposition pressure is a function of temperature, it is clear that the heat transfer occurring in the single-phase segment of the channel will determine where the reaction starts, assuming that the pressure is accurately predicted as well. The following section is a review of the single-phase and two-phase correlations available in the open literature for the thermal performance of PHEs.

Single-phase Flow

For typical liquid-liquid duties, there is an immense wealth of correlations for predicting thermal performance of chevron PHEs, some of which are compiled by Khan *et al.* [61] and Thonon [44]. Again, many of these correlations are focused toward specific plate geometries, flow rates, and fluids – most of which lie outside of the operating envelope and geometric characteristics of the system under consideration in this study. There is little available for low *Re* flows of viscous fluids, so lacking equipment and operating condition specific heat transfer information, recourse must be made to more general, but less accurate, correlations. First, it is desirable to establish the range of variation to be expected in the single-phase heat transfer coefficient. To cover the region in the reactor prior to the onset of reaction ($P > P_{eq}$), a correlation due to Muley, Manglik, and Metwally [43] was selected:

$$Nu = 1.6774\left(D_e / L\right)^{1/3}\left(\beta / 30\,\mathrm{deg}\right)^{0.38}\mathrm{Re}^{0.5}\,\mathrm{Pr}^{1/3}\left(\mu / \mu_w\right)^{0.14} \tag{60}$$

Since it was developed for viscous flows ($30 \leq \mathrm{Re} \leq 400$) and a corrugation amplitude ratio $2b/\Lambda = 0.56$, Equation (60) is correlated from data from the closest known match to the geometric parameters and flow conditions in this study's PHE ($2b/\Lambda = 0.43$, $1 \leq \mathrm{Re} \leq 100$). The higher

corrugation aspect ratio used to develop Equation (60) strongly suggests that it may overestimate the single phase heat transfer due to the increase of swirl flow that is promoted by deeper corrugations [50]. Therefore, Equation (60) will serve as an upper bound on the single phase heat transfer achievable with this system. To furnish a conservative estimate, and hence a lower bound on the prediction for the single-phase heat transfer, one may use Kakac *et al.*'s [62] correlation for flat plate heat exchangers:

$$Nu = 1.849\left[\left(D_e / L\right)\mathrm{Re}\,\mathrm{Pr}\right]^{1/3}\left(\mu / \mu_w\right)^{0.14} \tag{61}$$

Predictions from Equation (61) would represent the limiting case of laminar flow absent the secondary flows and higher surface area characteristic of a PHE's corrugated channel.

Figure 11shows a comparison between the Nusselt numbers calculated using Equations (60), (61) , and (63) over the low-*Re* range of interest with Pr = 107 (approximate value at 60°C). This comparison shows that Martin's correlation, Equation (63), despite being originally intended for turbulent flow in PHEs, may be a reasonable compromise between the respectively high and low predictions of Equations (60) and (61). However, it is important to note that Equation (63) has been modified slightly to fit between the two limiting cases discussed above: the value 0.122 has been reduced to 0.072, and is multiplied by the area enlargement factor Φ_{AE} since Martin's equation is based on the hydraulic diameter (for the Alfa Laval M3, $\Phi_{AE} \cong 1.1$ and $D_e / L \cong 0.0098$, where *L* is taken as the port-to-port plate length).

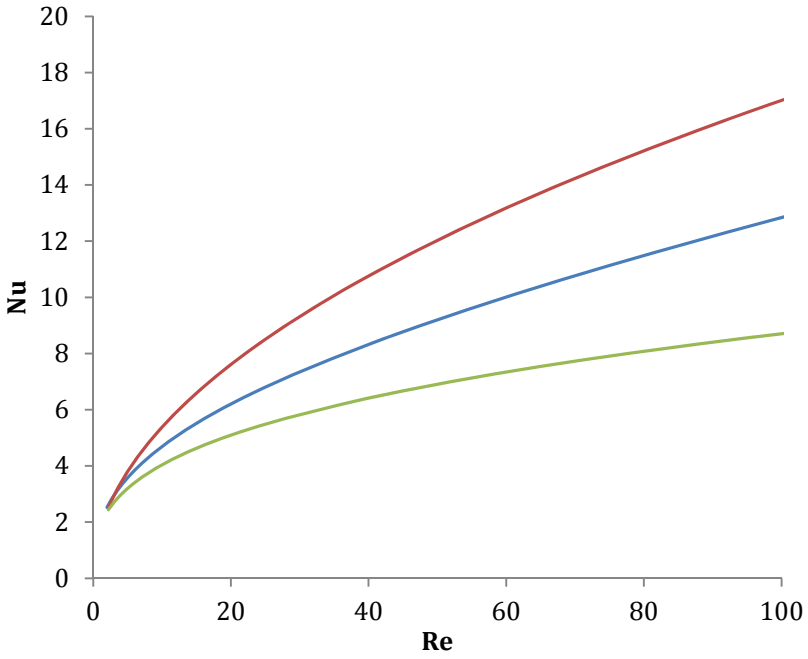

Figure 11 – Comparison of single-phase Nusselt number predictions obtained using the correlations in Equations (60) (red), (61) (green), and (63) blue

Two-phase flow

Heat transfer correlations for two-phase flow situations similar to those discussed above could not be located in the open literature, save for boiling or condensation correlations that would be unrealistic to predict the slurry side heat transfer coefficient. Perhaps the most promising approach is offered by Martin [41] and Schlünder [63], which exploits the asymptotic Lévêque solution as a means of relating the friction factor and Nusselt number, originally developed for the thermally developing, hydrodynamically fully-developed flow in circular tubes [64]. Martin proposed a modified form of the generalized Lévêque equation to correlate heat transfer data for turbulent flow in PHEs:

$$Nu_h = C_2 \, \mathrm{Pr}^{1/3} \left[f \, \mathrm{Re}^2 \, D / L \right]^{1/3} \tag{62}$$

where, the constant $C_2 = 3^{3/4}/[4\Gamma(1/3)]$ and $\Gamma(x)$ is the gamma function. While the Lévêque solution was originally intended for thermally developing laminar flow, Martin and Schlünder note that there is no reason to restrict its application as such. The modified semi-empirical form of the generalized solution for turbulent flow in PHEs, as proposed by Martin, is:

$$Nu_h = 0.122\,\mathrm{Pr}^{1/3}\left(\mu/\mu_w\right)^{1/6}\left[f\,\mathrm{Re}^2\sin(2\beta)\right]^{0.374} \tag{63}$$

To see how this may be applied to a two-phase flow situation, consider the origin of the term fRe^2, which arises from the asymptotic Lévêque approximation of the velocity profile near a solid wall [64]:

$$\lim_{y^*\to 0} u(y^*) = \left.\frac{du}{dy^*}\right|_{wall} y^* \tag{64}$$

$$\left.\frac{du}{dy^*}\right|_{wall} = \frac{1}{8}\frac{\left(f\rho U^2\right)_{ls}\Phi_{TP}^2}{\mu_{ls}} \tag{65}$$

where, Φ_{TP}^2 is the two-phase multiplier and f_{ls} is the corresponding single-phase friction factor for (slurry) liquid flowing alone. When substituted into the 2-D energy equation (neglecting axial conduction effects), one obtains the Lévêque approximation [64]:

$$\frac{\partial T}{\partial z^*}\left(\frac{\left(f\rho U^2\right)_{ls}\Phi_{TP}^2 y^*}{8\lambda_{ls}\mu_{ls}}\right) = \frac{\partial^2 T}{\partial y^{*2}} \tag{66}$$

This is a parabolic PDE that admits the following similarity transformation, after Jones [65]:

$$\psi'' + \frac{1}{3}\xi^2\psi' = 0 \tag{67}$$

where, for the constant wall temperature boundary condition,

$$\psi(\xi) = \frac{T - T_b}{T_w - T_b} \tag{68}$$

$$\xi = y\left(\frac{\left(f\rho U^2\right)_{ls}\Phi_{TP}^2}{8z^*\lambda_{ls}\mu_{ls}}\right)^{1/3} \tag{69}$$

$$\psi(0) = 1 \tag{70}$$

$$\psi(\xi \to \infty) = 0 \tag{71}$$

The corresponding solution is

$$\frac{T - T_b}{T_w - T_b} = 1 - \int_0^{\xi} \exp\left\{\frac{s^3}{9}\right\} ds \Big/ \int_0^{\infty} \exp\left\{\frac{s^3}{9}\right\} ds \tag{72}$$

For small ξ, as would be the case if the conductive heat transfer is assumed to be restricted to a thin layer in the vicinity of the wall, the solution may be approximated as

$$\frac{T - T_b}{T_w - T_b} \cong 1 - \frac{\xi(3)^{1/3}}{\Gamma(1/3)} \tag{73}$$

From which the Nusselt number, *Nu*, may be obtained:

$$Nu_h = \frac{hD_h}{k_{ls}} = -\frac{D_h \left.\frac{\partial T}{\partial y^*}\right|_{wall}}{T_w - T_b} \tag{74}$$

$$Nu_h = \frac{3^{1/3}}{\Gamma(1/3)}\left(\frac{f_{ls}\Phi_{TP}^2 \,\mathrm{Re}^2 \,\mathrm{Pr}\, D_h}{8z^*}\right)^{1/3} \tag{75}$$

In Martin's case, the term z^* is taken to be the distance between two crossing furrows. The principle argument here is that the original Lévêque approximation requires knowledge only of the velocity gradient at the wall. As long as the conduction sub-layer remains thin, such as in a thermal entry region or in fully-turbulent duct flow, then the forgoing result may still be applied. Assuming that the highly agitated two-phase flow arising from the solid-gas decomposition reaction is similar to turbulent flow (i.e., eddy-transport dominated bulk flow and a thin viscous

sub-layer where conduction dominates), then Martin's correlation for heat transfer in a PHE may be modified for two-phase flow simply by replacing f with $f_{ls}\Phi_{TP}^2$:

$$Nu = \Phi_{AE} 0.072 \,\mathrm{Pr}^{1/3} \left(\mu_{ls} / \mu_{ls,w}\right)^{1/6} \left[f_{ls} \Phi_{TP}^2 \,\mathrm{Re}^2 \sin(2\beta) \right]^{0.374} \tag{76}$$

where, again, the constant 0.122 was reduced to 0.072 to fall between Equations (60) and (61), and the area enlargement factor Φ_{AE} is included herein to account for the fact that Martin's correlation used the hydraulic diameter, since,

$$Nu = \Phi_{AE} Nu_h \tag{77}$$

The adjustment mentioned above should only be applied for $D_e / L \cong 0.0098$, since a change in the plate length and/or equivalent diameter would also change the upper and lower bound estimations.

It will likely come to pass that the empirical exponent and constant, which Martin obtained by fitting his equation to empirical correlations for industrial plates at different chevron angles and using the average of the parameters, will need to be tuned. This relation implies that the presence of bubbles in the bulk flow will cause an enhancement in heat transfer for flows having the same single-phase Reynolds number (assuming Equation (63) is applicable to turbulent flow as well as laminar flow), since $\Phi_{TP}^2 \geq 1$ – such a phenomenon was observed by Vlasogiannis *et al*. [56] in their flow visualization and heat transfer study of air-water two-phase flow in PHEs with vertical upward flow, although no mechanism for this enhancement was proposed. This may be explained, plausibly, upon consideration of the enhanced mixing from bubble agitation: the same mechanism responsible for increasing the frictional pressure drop is also responsible for enhancing the heat transfer.

Figure 12compares the predictions of Equation (76) as a function of conversion with the corresponding single-phase flow predictions from Equations (60), (61), and (63) for a liquid

superficial velocity of 0.06 m/s (approximately what is realized in the benchtop-scale reactor) and with AC mass concentrations of 1, 4, and 8 kg/m^3. The plot in Figure 12 demonstrates the upper and lower bounds expected for heat transfer performance; the range of values appears reasonable for low Reynolds flows.

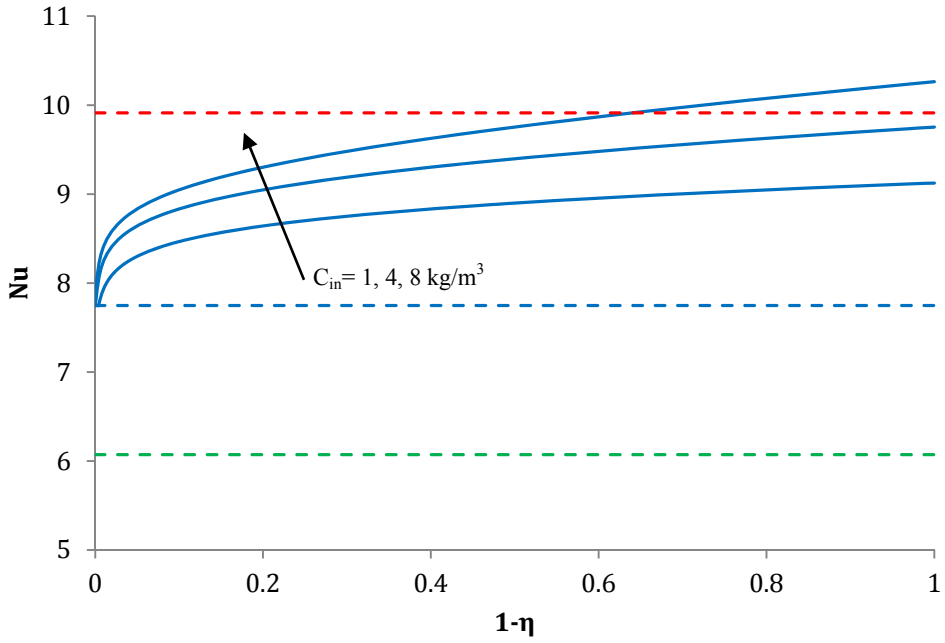

Figure 12-Comparison between two-phase Nusselt number predictions from Equation (76) as a function of conversion and single-phase Nusselt number predictions at the same superficial liquid velocity for different AC mass loadings (C_{in}). Dashed black line: Mulley and Manglik correlation, Equation (60); dashed blue line: Martin correlation, Equation (76); dashed red line: Kakac correlation, Equation (61)

It should be noted that Equation (76) is the only relation that would provide continuous variation with Φ_{TP}; no sudden jumps in the heat transfer coefficient would result once the

reaction commences and the model switches from the single-phase correlation to the two-phase correlation.

Numerical Model

The numerical code developed to solve the governing equations detailed in the previous chapter relies on the finite volume (FV) method, which exploits Gauss' divergence theorem to convert the volume integrals of Equations (21), (37) - (39) to surface integrals. As a result, each discrete cell serves as a finite-size control volume, inside of which the flow variables are assumed to vary continuously. Since the variation inside the cells is not known a-priori, it must be approximated by some type of interpolation scheme between the values at the cell faces. The development of the discretized mathematical model and the numerical scheme to obtain the solutions are discussed in this section.

Computational Domain and Discretization Scheme

The N channels of the physical domain defined for the mathematical model is discretized along the z-axis into I equal segments of length Δz. These "cells" represent the control volumes for which the intensive flow properties are to be determined; the governing equations are then integrated over each of these cells to obtain an algebraic system of equations that can be solved numerically using readily available computational techniques to produce a discrete approximation of the continuous system. For this purpose, consider the single cell (i,n) in Figure 13 whose center is located at $z_i = (i\text{-}1/2)\Delta z$:

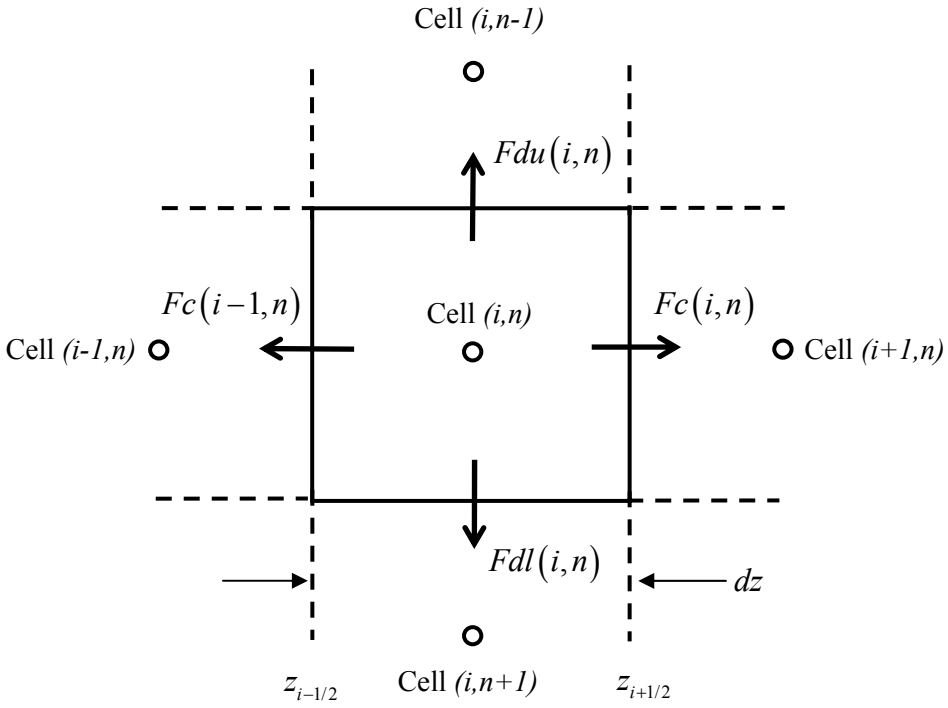

Figure 13 – Typical finite volume cell

The surface normals for the cell are indicated by the bold solid arrows. For the 1-D model, subject to the assumptions discussed in the previous section, the conservation equation for a generic intensive flow variable $\Phi(z,n)$ is

$$\frac{d}{dz}\left[U(n)\Phi(z,n)\right] = \phi'''(z,n) + \frac{1}{D_e}\left(\phi''_{w,u}(z,n) + \phi''_{w,l}(z,n)\right) \tag{78}$$

Here, U_{ls} is the superficial velocity of the liquid phase (which, again, may differ by channel if maldistribution is present), since for all the governing equations considered in this model the gas phase does not participate in transporting the flow quantities of interest. The term ϕ''' is a

volumetric source term; $\phi''_{w,l}$ and $\phi''_{w,u}$ are wall flux terms at the lower and upper plate forming the channel wall, respectively. This equation is then integrated from $z_{i-1/2}$ to $z_{i+1/2}$:

$$Fc(i,n) - Fc(i-1,n) = S(i,n) + \frac{1}{D_e}\left(Fdu(i,n) + Fdl(i,n)\right) \tag{79}$$

where the convective and wall flux functions for the cell (i,n) are defined as:

$$Fc\left(i,n\right) = \int_{z_{i-1/2}}^{z_{i+1/2}} U\left(n\right)\frac{d}{dz}\Phi\left(z,n\right)dz \tag{80}$$

$$Fdu\left(i,n\right) = \int_{z_{i-1/2}}^{z_{i+1/2}} \phi''_{w,l}\left(z,n\right)dz \tag{81}$$

$$Fdl\left(i,n\right) = \int_{z_{i-1/2}}^{z_{i+1/2}} \phi''_{w,l}\left(z,n\right)dz \tag{82}$$

And the source term function,

$$S\left(i,n\right) = \int_{z_{i-1/2}}^{z_{i+1/2}} \phi'''(z,n)dz \tag{83}$$

This approach is used to obtain the FV form of the mass, momentum, and energy equations, where the appropriate substitution for Φ is made, as shown in Table 2 and Table 3.

Table 2 – Convective and diffusive flux functions rendered in discrete form

Equation	Φ	***Fc(i,n)***	***Fd(i,n,n±1)***
Mass	η	$U_{ls}(n)\eta(i,n)$	0
Energy (slurry)	θ	$U_{ls}(n)\theta(i,n)$	$\varphi(i,n,n\pm1)\left[\theta(i,n\pm1)-\theta(i,n)\right]$
Energy (load)	θ	$U_{ld}(n)\theta(i,n)$	$R(n)\varphi(i,n,n\pm1)\left[\theta(i,n\pm1)-\theta(i,n)\right]$
Momentum	P	$P(i,n)$	$\left(1/2D_h\right)f_{ls}(i,n)U_{ls}^2(n)\Phi_{TP}^2(i,n)$

Table 3 - Volumetric source terms rendered in discrete form

Equation	Φ	$S(i,n)$
Mass	η	$-Da(n)\eta(i,n)^{\frac{2}{3}}\dot{M}'''(i,n)\left(1-\alpha(i,n)\right)$
Energy (slurry)	θ	$-Da(n)\eta(i,n)^{\frac{2}{3}}\dot{M}'''(i,n)\left(1-\alpha(i,n)\right)$
Energy (load)	θ	0
Momentum	P	$-g\left[\alpha(i,n)\rho_g(i,n)+\left(1-\alpha(i,n)\right)\rho_{ls}\right]$

The values at the cell faces -- $\Phi(z_{i+1/2},n)$ and the like – are presumed known, while values of Φ within a cell are approximated by an appropriate interpolation scheme. To start, linear interpolation is used in the present version of the code. However, the user may select a value of the blending parameter, ζ_Φ, to be used in estimating the volume average of Φ for a given cell:

$$\bar{\Phi}(i,n)=\left(1-\zeta_\Phi\right)\Phi(i+1/2,n)+\zeta_\Phi\Phi(i-1/2,n) \tag{84}$$

Setting $\zeta_\Phi = 1$ gives a fully upwind biased scheme for parallel flow channel, or a downwind biased scheme for a counterflow channel. This weighting parameter may be adjusted independently for each variable that requires an evaluation inside the cell, hence the subscript.

Solution Procedure

Because of the non-linear source term, the system must be solved iteratively. This is accomplished by linearizing the equations about an initial guess, computing the solution of the linearized equations, and then repeating the process with the previously calculated values as the new guess values until the change between successive guess values falls below a pre-determined error tolerance. For any flow variable having an actual value (e.g., the true solution to the

system) Φ, let $\hat{\Phi}$ represent the guess value, and $\delta\Phi$ represent a small perturbation from the guess value such that:

$$\Phi = \hat{\Phi} + \delta\Phi \tag{85}$$

If the perturbation is assumed to be small, the perturbation of the source term may be neglected and any terms involving $\delta\Phi$ multiplied by either itself or the perturbation of other unknown variables may be also neglected. Any flux function *F* may then be written as:

$$F(i,n) = \hat{F}(i,n) + \delta F(i,n) \tag{86}$$

where δF signifies the perturbation of the flux function with respect to the variable Φ, and the hat signifies the value of the flux function with respect to $\hat{\Phi}$. The finite volume equation for the cell centered at z_i is then approximated by:

$$\begin{aligned} &\delta\left(Fc(i-1,n) - Fc(i,n)\right) - \frac{\delta}{D_e}\left(Fdu(i,n) + Fdl(i,n)\right) = \\ &-\left(\hat{F}c(i-1,n) - \hat{F}c(i,n)\right) - \frac{1}{D_e}\left(\hat{F}du(i,n) + \hat{F}dl(i,n)\right) - \hat{S}(i,n) \end{aligned} \tag{87}$$

This, for convenience, will hereafter be represented by

$$\delta Eq(i,n) = -\hat{E}q(i,n) \tag{88}$$

where, *Eq(i,n)* is the conservation equation for Φ associated with the cell at z_i in channel *n*, and the operator δ and hat superscript represent the left-hand side and right hand side of Equation (87), respectively. Since the terms on the right-hand side are known at the current iteration, and the terms on the left-hand side are linear in $\delta\Phi$, the system of equations for a total of *J* cells in the computational domain may be rendered as a linear system:

$$T_{jk}\delta\Phi_k = X_j \tag{89}$$

where, T_{jk} is the coefficient matrix, $\delta\Phi_k$ is the vector of unknowns in δEq, and X_j is the vector containing $\hat{E}q(i,n)$ for each cell. Solving this linear system and applying (83) for each variable Φ yields the new guess values for the next iteration.

Rather than solving for temperature, concentration, and pressure in a single linear system, the numerical code developed decouples the mass and energy equations into two separate linear systems and solves them independently. With the new guesses obtained for the temperature and concentration, the momentum equation is subsequently applied directly to each cell to obtain the new pressure field. While this process requires more iteration to achieve convergence, it is significantly less computationally expensive than solving a single system that would be 3 times larger, thereby allowing for finer axial resolution to be achieved. This consideration becomes especially important if the user intends to simulate a reactor with a large number of plates. Furthermore, since there is only a one-way coupling between the momentum and mass transfer equations, the pressure is re-evaluated at the end of an iteration for each cell using the latest values of η. After every 10 iterative cycles or so, the coefficient matrix for the energy equation is updated, since cells with changing values of η have changing convection coefficients, according to Equation (76).

To aid the convergence of the solution, especially for cases with high *Da*, it was found that limiting the change permissible in the primary flow variables between successive iterations was necessary. This was accomplished by applying a constant multiplying factor $p \leq 1$ to the right hand side of the system in Equation (89), which effectively reduces the magnitude of the correction $\delta\Phi_k$, but still progresses the iterative procedure closer to $X_j = 0$. This is especially important for the first few iterations after the initial guess, which will often produce large $\delta\Phi_k$ and over-correct, leading to either divergence or and/or oscillatory behavior. An additional

safeguard against divergence was to place reasonable upper and lower limits on the primary variables θ and η. The lower limit for the temperature was placed at 0.01 to avoid the possibility of negative absolute temperatures, which are both physically impossible and would rapidly cause divergence since Equation (5) would grow rapidly, thereby causing further reduction in temperature for the next iteration and sending the temperature to $-\infty$, or predicting premature exhaustion of the AC. An upper limit on θ was not needed since increased temperature tended to increase the reaction rate and consequently cause a lower temperature prediction on the next iteration.

For cases where the AC was completely exhausted before the outlet, the source term needed to be "shut-off" to reflect the fact that the endothermic reaction would cease. Although the kinetic model dictates that η would approach 0 asymptotically on account of the vanishing surface area, it is possible for negative concentration values to arise when there is insufficient axial resolution. Forcing the source term in the species conservation equation to 0 when this occurs creates a step discontinuity in the concentration profile, which can lead to oscillations in the iterative procedure through the following mechanism:

1) The source term is set to 0 when $\eta \leq 0$, negative η are automatically set to 0;
2) On the subsequent iteration, excess mass upstream of the switch-off point causes cells downstream with the source term switched "off" to attain $\eta > 0$.
3) The source term is switched "on" in the next iteration, causing the cycle to repeat.

This numerical artifact is especially pronounced for high *Da*, where the source term can produce large changes in η. The greater magnitude of these changes will increase the margin from the source term's shut-off criterion ($\eta \leq 0$) about which the oscillations will occur. The problem could be remedied by allowing the source term to remain "on" for the species equation, even with negative concentration values, thereby eliminating the discontinuity in the concentration

profile. Conversely, in cells where $\eta \leq 0$, the source term is switched "off" for the energy equation. Once the iterative procedure converged, the negative concentration values were set to zero. Using this procedure the numerical oscillations can be obviated and can render enhanced stability to the overall iterative procedure.

Temperature Dependence of Thermal Properties

The presence of the viscosity correction term in the heat transfer correlations is an additional aspect that must be considered because both the Prandtl number and the viscosity of PG decrease considerably with temperature. Figure 14 shows that over the 30 - 60°C range, the viscosity decreases by a factor of 3.8, approximately. Thus, the term $(\mu/\mu_w)^{0.16}$ in Equations (63) and (76) is roughly 1.2, if one assumes the slurry and thermal load are at 30° C and 60° C, respectively. The usual engineering approximation for fluid properties in instances where large cold and hot stream temperature differences are present is to evaluate them at an appropriate mean temperature. The model's dependence on empirical correlations precludes a complete account of these highly-nonlinear effects due to the additional feedback mechanism between the mass, momentum, and energy equations; for the time being, the choice was made to simply apply this standard approach to the model, and assume that the viscosity correction term was unity to avoid over-prediction, since the exponent on the correction terms were not fitted to highly viscous fluids. Also, it was found that attempting to incorporate the temperature dependence of the fluid properties to the local heat transfer and friction factor calculations destabilized the iterative solution procedure, and therefore required higher relaxation to be applied. This slowed the execution time for the simulation considerably. With no real guarantee that this approach would improve the numerical model's accuracy, it was decided that neglecting the viscosity correction term was the best course of action, so as not to the run the risk of over-prediction.

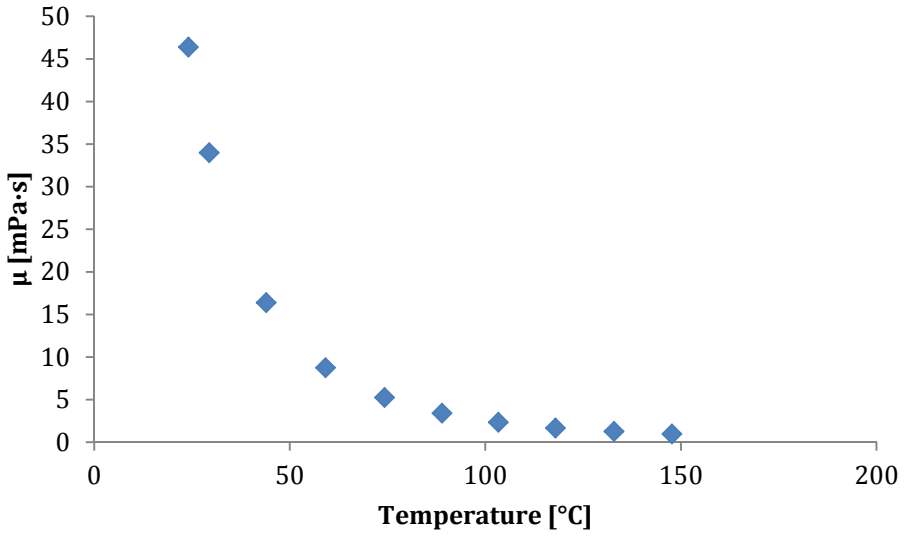

Figure 14 – Viscosity of pure propylene glycol (PG) as a function of temperature [39]

Other thermo-physical properties of interest, namely the thermal conductivity and density, do not appear to change significantly over the 30-60°C range [39].

Model Predictions for a Reactor Sizing Problem

From a system design standpoint, the question yet unanswered for the proposed architecture is, "Given a set of operating constraints, how much AC can be reacted? At what point does the reactor achieve complete conversion?" To show that the model is capable of answering this question, a "prototype" system consisting of 7 channels, with three 4 load-side channels and 3 slurry channels in a parallel flow arrangement (shown in Figure 5) was simulated using the numerical scheme detailed above. The load fluid was chosen to be water, since this is a commonly used fluid for liquid-liquid heat exchanger duties, although this choice is somewhat arbitrary for the following set of simulations for reasons that will be described shortly. The inlet pressure, flow rate, load fluid inlet temperatures, and AC loadings were systematically varied.

The numerical model was used to calculate the axial variation of pressure, temperature, and concentration; for each channel. From this data, the overall performance is gauged by the total heat rejection rate and the rate of AC consumption as a function of the operating conditions. The choice to use only seven channels was motivated primarily by the limitations of the computational power available for performing the calculations, but it also illustrates how the end plates effect the distribution of the thermal load.

Material Properties

The thermophysical properties for each simulation are held constant and evaluated according to the tabulated values in Table 4:

Table 4 – Material property inputs for simulations

Property	Value	Units	Source
k_{wall}	13.4	W/m·K	[40]
k_{ls}	0.196	W/m·K	[39]
k_{ld}	0.5	W/m·K	[40]
$c_{p,ls}$	2700	J/kg·K	[66]
$c_{p,ld}$	4180	J/kg·K	[40]
μ_{ls}	Equation (90)	mPa·s	[39]

Table 4 Continued

Property	Value	Units	Source
μ_{ld}	1.0	mPa·s	[40]
μ_g	0.012	mPa·s	[40]
ρ_{ls}	1036	kg/m^3	[39]
ρ_{ld}	1000	kg/m^3	[40]
ρ_p	780	kg/m^3	[2]
ΔH	2000	kJ/kg	[2]

The slurry temperature is evaluated at the slurry inlet temperature, which will produce conservative heat transfer coefficient estimates due to the lower Reynolds number (additionally, these simulations were run with the slurry inlet temperature at 62°C, so the change in the viscosity is not as severe, as compared to temperatures in the vicinity of 30°C). The property evaluation is taken from an exponential curve fit to the data from [39]:

$$\mu_{ls} = \exp\left\{\left(1.7411E-4\right)T_{in,n}{}^2 - \left(0.15489\right)T_{in,n} + 34.452\right\} \tag{90}$$

where, T_{in} is the inlet temperature of the slurry in kelvin. This relation is applicable to 300 K ≤ T ≤ 406 K. The gas viscosity, μ_g, is assumed to be that of carbon dioxide at standard temperature and pressure since the results are not noticeably sensitive to variations thereof. The gas product is assumed to behave as an ideal stoichiometric mixture based on the reaction in equation 1, allowing the density to be estimated from the ideal gas equation of state and Dalton's law:

$$\rho_g = \frac{M_{AC}P}{3T\bar{R}} \tag{91}$$

where, M_{AC} is the molecular weight of the gas mixture. The gas temperature is assumed to remain at the slurry inlet temperature, but is allowed to vary with pressure in accordance with the recommendation of Kreissig and Müller-Steinhagen [54].

For the set of simulations discussed here, the conditions on the load side of the reactor were selected to emulate isothermal conditions that would be encountered during a condensation process. To avoid modifying the code, which is configured to solve the conjugate heat transfer problem, the flow rate of the water was set much higher than the slurry (1.42 L/s) so that its bulk temperature change from inlet to outlet would be negligible compared to the slurry's temperature change. The properties assumed for the water have little effect on the results, since the dominant thermal resistance is on the slurry side and the wall temperature is effectively constant – they were assumed to be those corresponding to 25°C for simplicity's sake. The objective of this exercise is to examine the thermal and chemical effects on the slurry side.

The plate length, width, chevron angle, and area enlargement factor were selected to mirror the Alpha Laval M3 PHE used in this study, and are summarized in Table 5:

Table 5 – PHE geometric parameters used in simulation

Parameter	Value
L	0.48 m
D_e	0.00468 m
W	0.10 m
Φ_{AE}	1.1
β	30°

It was found that 100 divisions per channel were sufficient to ensure convergence for these simulations, as an increase to 200 divisions changed the heat rejection predictions by only ~1%. The energy and mass conservation equations were satisfied to within an order of 10^{-9} and 10^{-10}, respectively.

Estimation of Kinetic Parameters

The parameters relevant for the kinetic model are the particle diameter (fixed at 0.25 mm) and the constant κ in Equation (33) . The data reported by Schmidt for his batch reactor was used to estimate κ, since both pressure, temperature, and heat rejection data was provided. For the batch reactor, a closed system energy balance gives:

$$\dot{w} = \Delta H A_{total} \kappa \left(P - P_{eq} \right)^2 \tag{92}$$

where, $\dot{w}$ is the energy absorbed from the heating coil due to the endothermic reaction (assuming perfect mixing, i.e., the heat from the hot-side fluid is absorbed by the AC immediately), and A_{total} is the total particle surface area, given by

$$A_{total} = \frac{24 m_{AC}}{D_p \rho_p} \tag{93}$$

where, m_{AC} is the total mass of AC added to the reactor, assuming spherical particles of uniform size. Therefore, after combining Equations (90) and (91),

$$\kappa \cong \frac{\dot{w} D_p \rho_p}{24 \Delta H m_{AC} \left(P - P_{eq} \right)^2} \tag{94}$$

Using the peak power ratings for Schmidt's data using PG as the heat transfer medium at 60°C and 400 torr, assuming a particles diameter of roughly 1 mm, and assuming a particle density of 780 kg/m^3 (the minimum density specification for the bulk power Schmidt used in his experiments), κ was estimated to be 2.4×10^{-10} m^{-2} kPa^{-2}. The caveat for this estimation is that

the particles sizes were not well controlled in Schmidt's experiment and no particles size measurements were apparently taken. The peak power rating was selected for this estimation because at the small timeframe during which the peak power was recorded, after the AC was introduced into the reaction chamber, the particle temperature would be closest to the bulk fluid temperature. Hence, P_{eq} could then be calculated with reasonable accuracy. This value was used in all simulations performed in this study.

Effect of Residence Time on Conversion

Ideally, one would operate the reactor such that the amount of AC loaded into the slurry is precisely the amount that is consumed so that no AC reacts outside of the exchanger. However, the limited residence time inside the reactor effectively limits the amount of AC that can be reacted for a given flow rate, inlet pressure, and inlet pressures. Thus, a tradeoff point exists in the sense that the power rating due to AC decomposition increases with slurry flow rate, the fraction of total AC reacted is reduced. This can be counteracted by increasing the slurry or load-side inlet temperature, reducing the inlet pressure by manipulating the reactor back pressure, or some combination of the two. It is also important to bear in mind that the inlet slurry temperature should be such that no AC (or only a small amount) reacts before reaching the reactor, placing a limit on the amount of pre-heating that can be applied to the slurry.

Figure 15 shows three simulations that were performed for a fixed inlet pressure of 108 kPa and different slurry flow rates, which are assumed to be distributed evenly through the three slurry channels. The slurry inlet temperature is set at 335 K so that the reaction will start slightly downstream of the inlet. For three different slurry flow rates, the load fluid temperature is increased until ~95% conversion is achieved; the decreasing particle surface area model would dictate that 100% conversion is approached asymptotically. For the lowest flow rate (0.014 L/s/channel), the load fluid temperature only needed to be increased to about 350 K, and

complete conversion is approached quickly. Increasing the flow rate required increasingly larger load temperature increases in order to attain complete conversion, requiring up to 390 K for the fastest flow rate. On the lower plot, the total amount of energy rejected as latent heat is shown as a function of load side temperature. Increasing the power rating by increasing the flow rate comes at the expense of requiring significantly higher temperatures.

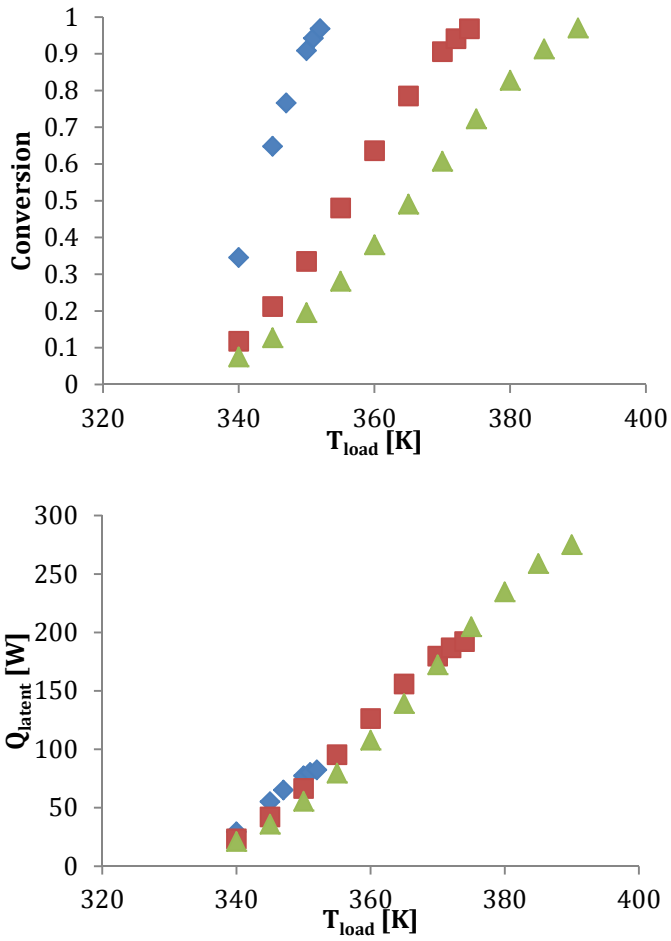

Figure 15 – Conversion (top) and total latent heat absorbed (bottom) as a function of load inlet temperature for a slurry inlet pressure of 108 kPa and slurry inlet temperature of 335 K for slurry flow rates of 0.04, 0.10 and 0.14 L/s (blue, red, green)

The next set of simulations examined the effect of inlet pressure alone for a fixed flow rate of 0.014 L/s and 0.043 L/s, so as to determine whether the flow rate or pressure was the dominant factor in conversion. Also, the AC loading was set to 8 kg/m^3 so that the endothermic reaction would have a noticeable effect on the temperature profiles. Figure 16 compares the conversion as a function of load fluid temperature, T_{ld}, for different inlet pressures. The inlet pressure did not appear to have that drastic of an effect on the size of the load temperature range over which $0 < \eta < 1$ for a fixed flow rate. However, increasing the flow rate by three fold significantly increased the requisite load temperature for complete conversion, while also reducing the apparent effect of the pressure

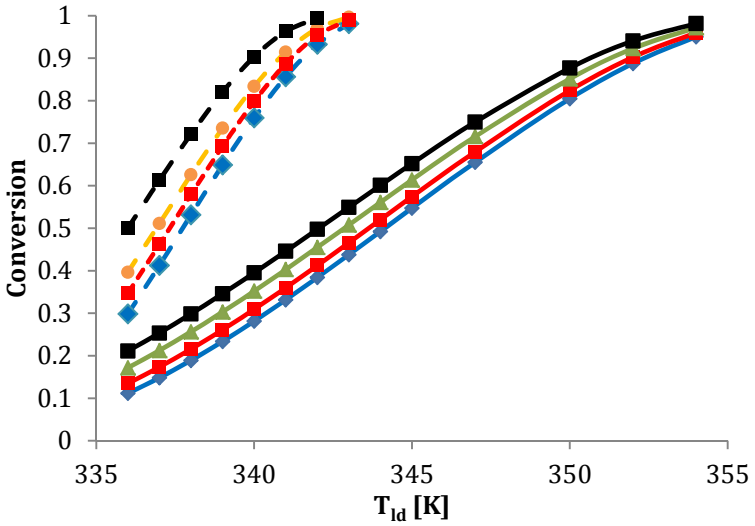

Figure 16 – Conversion as a function of load temperature for different inlet pressures and slurry flow rates of 0.014 L/s (dashed line) and 0.043 (solid line): 110 kPa (blue), 108 kPa (red), 106 kPa (orange), 105 kPa (green), and 102 kPa (black)

It is also interesting to consider the ratio of energy consumed by the reaction to the total heat extracted from the load fluid as a sort of effectiveness metric. The logic behind this idea is that, ideally, as much of the thermal load as possible should be rejected in the form of latent heat. However, because a finite temperature difference is required between the load and slurry sides, some of this heat will be rejected as sensible heat in the slurry fluid. Because higher temperatures tend to increase the reaction rate at a given pressure, the proportion of latent heat to sensible heat will be a function of the timescale for heat transfer between the fluids relative to the reaction timescale. The results corresponding to the data in Figure 16 are plotted as a function of normalized load temperature in Figure 17– T_{ld}* is the highest load temperature at which complete conversion is achieved for the respective data set (343 K for the "low" slurry flow rate and 354 for the "high" slurry flow rate); T_{ls} is the slurry inlet temperature, which is 335 K in all cases.

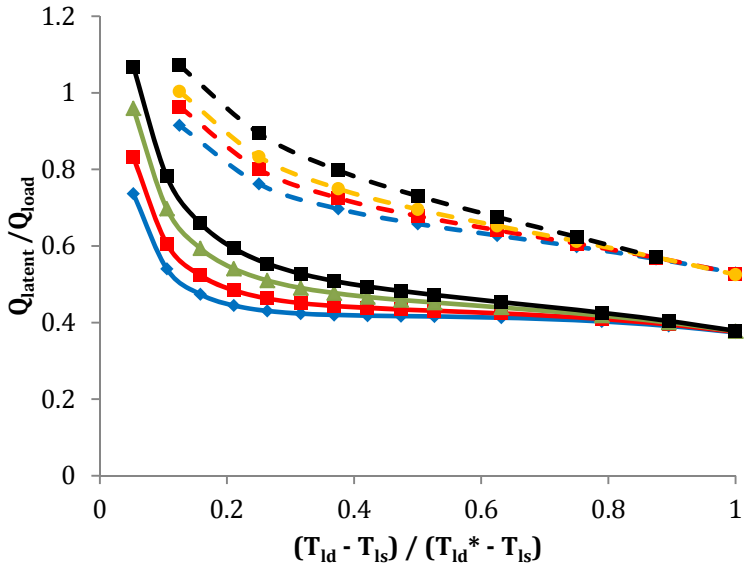

Figure 17 – Latent/sensible heat ratio as a function of normalized load temperature for slurry flow rates of 0.014 L/s (dashed line) and 0.043 L/s (solid line) for different inlet pressures: 110 kPa (blue), 108 kPa (red), 106 kPa (orange), 105 kPa (green), and 102 kPa (black)

At low normalized load temperatures (corresponding to 336 K for both sets) and inlet pressures of 102 kPa, the amount of heat absorbed by the reaction is greater than the amount of heat removed from the load fluid, yielding a latent-to-load temperature ratio (LL-ratio) above unity. Physically, this means that the reaction occurs faster than the heat can be transferred from the load side. Such a situation is undesirable since the reaction will predominantly by consuming latent heat from the slurry, essentially wasting the AC. On the other hand, a latent-to-sensible heat ratio of unity occurs when heat is extracted from the load at the same rate as the reaction, constituting ideal operating conditions. The LL-ratio decreases monotonically in all cases, and converge to points corresponding to their respective flow rates as complete conversion is approached. One immediately notices that the lower flow rate has a higher LL-ratio at ~100% conversion than the higher flow rate.

The above results show that the slurry flow rate per channel is the dominant parameter in determining the extent of AC conversion when the pressure is above atmospheric. For a fixed flow rate and load temperature, the residence time may be increased by installing additional plates on the PHE to decrease the slurry flow rate per channel so as to achieve complete conversion. If one intends to operate with a minimum $T_{ld} - T_{ls}$ and reject a given thermal load as latent heat, the model can be used to determine the minimum number of plates for a given plate length, channel spacing, and chevron angle. As an example, suppose that it is desired to reject 2 kW of heat. Using the data from Figure 15- Figure 17, one can determine the required reactor size as a function of inlet pressure and AC loading. Table 6 tabulates the total and latent heat rejected, the corresponding operating conditions, and the predicted number of plates that would be needed to remove a 2 kW heat load. Entries in red text indicate that the required load temperature for complete conversion is above the electronics industry standard limit of 85°C [67], and therefore do not represent a viable design option:

Table 6: Reactor size (min. number of plates) to reject a thermal load of 2 kW; Red text indicates T_{ld} exceeding 85°C

Slurry Flow Rate (L/s)	C_{in} (kg/m^3)	Q_{latent} (W)	Q_{total} (W)	Q_{latent} / Q_{total}	ΔT (K)	P_{in} (kPa)	Min. Plates	q" (W/cm^2)
0.078	8	1114	2017	0.55	7.4	110	30	0.12
0.083	8	1185	2076	0.57	6.9	108	32	0.11
0.083	8	1185	2029	0.58	6.6	106	32	0.11
0.090	8	1293	2040	0.63	5.8	102	35	0.10
0.049	8	754	2015	0.37	19.0	110	6	0.58
0.056	8	862	2275	0.38	18.7	108	7	0.56
0.056	8	862	2228	0.39	18.1	105	7	0.55
0.056	8	862	2168	0.40	17.5	102	7	0.54
0.098	5	876	2051	0.43	5.8	105	38	0.09
0.049	5	471	2068	0.23	18.9	105	6	0.60
0.033	5	314	2103	0.15	43.5	105	1	3.65

The Alpha Laval M3 gasketed plate heat exchanger used in this study, with the compression bolts tightened fully and 30 plates installed, measures only 30.2 cm in height with the end plates included, the heat transfer plate stack being about 26.2 cm. This gives approximately 1 cm per additional plate added to the stack. Thus, choosing the fourth entry from the top in Table 6 for the reactor size (since it has the smallest ΔT and therefore the highest ratio of latent heat rejection to sensible heat rejection), a system to reject 2 kW of heat would be about 33 cm thick, occupy a volume of 29.6 L (~1800 in^3), have a footprint of 865 cm^2 (134 in^2) and weigh approximately 36 kg (the PHE used in this study weighed 36 kg with 30 plates when filled with water, as indicated by the manufacturers specification sheet). This reactor would

consume 0.72 g/s of AC. This reaffirms the choice for using a PHE as a reaction vessel, since adding additional channels to the heat exchanger amounts to only a small increase in size. Note also that because these simulations used only 7 channels (6 heat transfer plates and 2 end plates), the heat rejected per slurry channel will be underestimated for larger reactors (i.e., with 20+ channels) since the end plates act as insulators. This decreases the total thermal load rejected, but is only apparent with small reactors.

The overall power rating for the reactor is also an important measure of merit, since the overarching objective is to manage the greater heat loads anticipated to arise in the next generation of high-performance electronics. From the above results, it can be seen that increasing the power rating of the reactor by increasing the flow rate degrades the LL-ratio. From this consideration, there is a tradeoff between the total power rating and the proportion of latent heat consumed. The optimum balance of this tradeoff will certainly depend on the specific application and the design restrictions thereof. For any reactor design selected from Table 6, the total heat duty per unit surface area of heat transfer plate is:

$$q'' = \frac{Q_{total}}{\Phi_{AE} L_{pp} W N_{plates}} \tag{95}$$

Assuming the heat load for an electronic device is 50-100 w/cm^2 [68], a 200 cm^2 device would require 10-20 kW. With a plate area of ~533 cm^2, one would require the following number of plates for the operating conditions tabulated in Table 7 :

Table 7 – Minimum number of plates required to manage the waste heat of a hypothetical 200 cm^2 electronic device assuming heat fluxes between 50 and 100 W/cm^2; red text indicates that the maximum temperature for electronics cooling has been exceeded; green text indicates most favorable operating conditions

Operating Conditions					Min. Plates	
Min. Flow Rate (L/s)	Max. Flow Rate (L/s)	C_{in} (kg/m^3)	Q_{latent} / Q_{total}	ΔT (K)	50 W/cm^2	100 W/cm^2
0.40	0.81	8	0.55	7.4	161	322
0.42	0.84	8	0.57	6.9	167	334
0.43	0.86	8	0.58	6.6	171	341
0.47	0.93	8	0.63	5.8	186	371
0.23	0.46	8	0.37	19.0	32	64
0.24	0.47	8	0.38	18.7	33	67
0.24	0.48	8	0.39	18.1	34	68
0.25	0.50	8	0.40	17.5	35	70
0.50	1.00	5	0.43	5.8	200	401
0.23	0.45	5	0.23	18.9	31	63
0.10	0.19	5	0.15	43.5	5	10

The more realistic choices for this particular PHE are indicated with green text (assuming the PHE can accommodate 64-70 plates). With an LL-ratio of 37%-40%, a respectable portion of waste heat is rejected as latent heat, although larger load temperatures are required for complete conversion. In this case, one must compromise for the lower LL-ratio in favor of total power rating.

Axial Temperature and Concentration Profiles

In all of the conversion vs. load temperature curves a point of inflection may be observed, signifying the effect of decreasing particle surface area beginning to overtake the tendency of increasing temperature and decreasing pressure to accelerate the reaction. This is also manifested in the axial AC mass concentration profiles, as illustrated in Figure 18. Increasing the load temperature shifts the inflection point in the curves further upstream,

resulting in a bell-shaped curve. It is also instructive to consider the axial slurry temperature distribution as well. For the set of simulations shown in Figure 15 above, the temperature profiles for the 110 kPa inlet pressure case is plotted as a function of load temperature in Figure 19.

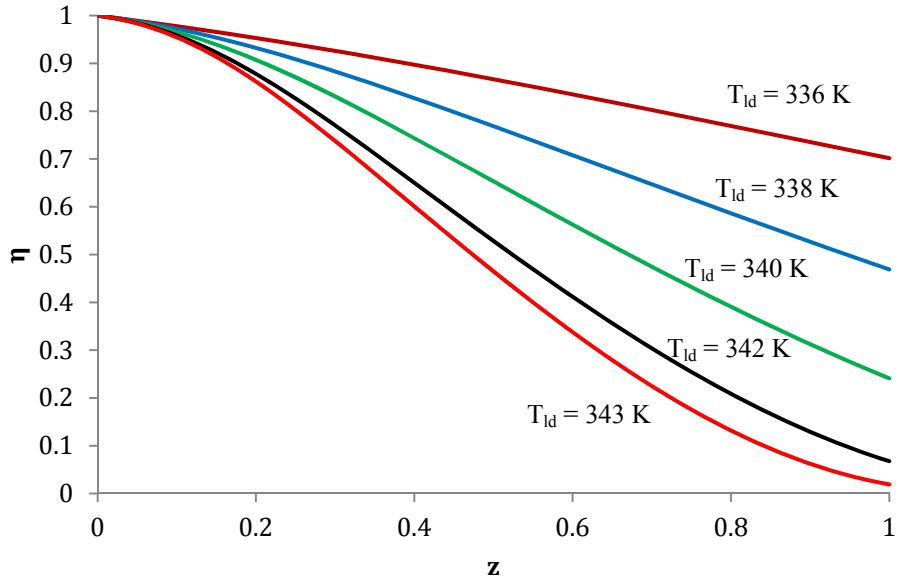

Figure 18 – AC mass concentration as a function of dimensionless axial distance for 108 kPa inlet pressure and slurry flow rate of 0.014 L/s for different load temperatures. AC mass loading was 8 kg/m^3

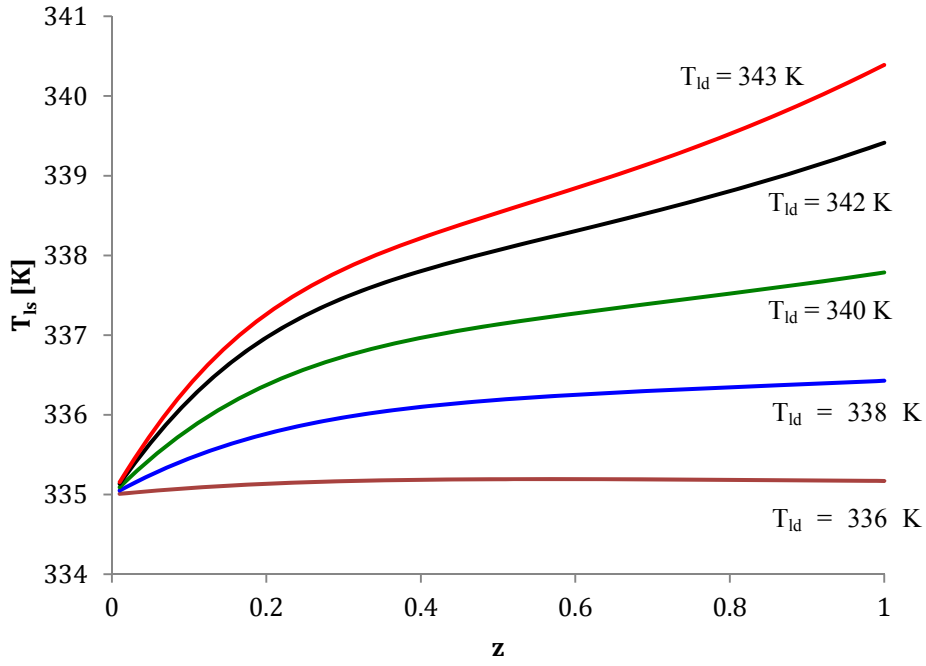

Figure 19 – Slurry temperature profile as a function of dimensionless axial distance for 110 kPa inlet pressure and slurry flow rate of 0.014 L/s at different load temperatures. AC mass loading was 8 kg/m^3

For lower load temperatures (and incomplete conversion), the slurry temperature profiles experience a brief increase before leveling off as the reaction accelerates. At higher temperatures, with the reaction nearing 100% conversion, an inflection point appears as the reaction begins to decelerate on account of the shrinking particles size in a fashion similar to that seen in the concentration profiles. Lower AC mass loadings, as expected, make this effect less pronounced since the amount of latent heat content relative to the sensible heat content is reduced.

CHAPTER III

EXPERIMENTAL WORK

Motivation

The coupled and non-linear governing equations associated with the hydrodynamic, thermal and chemical (species) transport phenomena in multi-phase flows that are encountered in this study – especially for a complex flow geometry in the heat exchanger configuration under consideration, necessitates experimental validation for calibration, refinement as well as evaluation of the accuracy and limitations of the predictive abilities of the numerical models developed in this study. None of the reports in the literature have explored the empirical characterization of gas producing chemical reactions in chevron plate heat exchangers. Hence, experimental validations of the predictions from the numerical model developed in this study were performed. The conjectures about the thermal-hydraulic behavior of the reactor are tested from the experimental investigations performed in this study. Limitations to the experimental facility prevented the testing of the ammonium carbamate for heat transfer measurements. Thus, the scope of the experimental work was limited to testing the hydrodynamic behavior of an analogous system, which is accomplished by simulating the gas-producing decomposition reaction by the well-known acid-base neutralization reaction between sodium bicarbonate and acetic acid.

The experiments were performed to obtain quantitative data for the magnitude of the bubble dynamics, pressure drop and the absolute pressure as well as qualitative information on the flow regimes. Both of the pressure parameters are affected by the rate of evolution of gas products in a chevron plate heat exchanger, and are of crucial importance in controlling the decomposition of AC. Insights gained from the experiments, in turn, may be used to evaluate the

accuracy of the assumptions used for developing the numerical models, and to calibrate as well as refine the numerical models, if necessary.

The primary objectives of this exercise are to obtain the following quantitative and qualitative information:

1. Gas phase behavior
    a. Flow regime and bubble characteristics
    b. Bubble velocities
2. Pressure field
    a. Total pressure
    b. Pressure drop

Methodology

Preliminary Testing and Chemical Characterization Studies

To allow for direct comparison with the numerical model, the parameters governing the chemical kinetics of the sodium bicarbonate/ acetic acid analog system were determined. The experimental parameters were adjusted to best simulate the analogous transport phenomena for the AC thermal management system. Both of these objectives were pursued in the preliminary experiments described in this section.

Chemical Kinetics

The overall acid-base neutralization reaction between sodium bicarbonate and acetic acid is described by:

$$NaHCO_3 + CH_3COOH \rightarrow CH_3COONa + H_2O + CO_2 \quad (96)$$

This is a multi-step reaction involving the dissociation of the aqueous reactants, the subsequent formation of carbonic acid and its decomposition into carbon dioxide and water, but is first-order

with respect to acetic acid, the dissociation of which is the rate-limiting step [69]. A simple first order rate law therefore describes the molar rate of gas generation,

$$\frac{d\left[CO_2\right]}{dt} = \hat{k}\left[CH_3COOH\right] \tag{97}$$

Sahoo and Saha [70] note that, in aqueous solution, the neutralization reaction was diffusion limited, and hence, the experimentally measured rate constant would depend on the degree of mixing – a comparison between the two works reveals that the moving water band technique employed by Parkash [69] showed reaction half-times on the order of 20 seconds, whereas Sahoo and Saha [70] measured the half-time as less than 1 second by measuring changes in solution conductance. The latter study showed that the rate constant measurements reported in the former study were tied to the rate of release of CO_2 from the aqueous solution, and could not be ascribed to the chemical kinetics. This complexity renders an accurate appraisal of the reaction time by direct observation to be quite difficult, for such an observation would require gauging the reaction time arising from the situation when the release of CO_2 could no longer be confirmed visibly.

Clearly, the task of ascertaining the functional relationship between the rate constant and flow conditions for an analog reactor is beyond the scope of this project. To gain an initial foothold for adapting this chemical system in the numerical model, an order-of-magnitude estimate of the "effective" rate constant (vis., what would be measured if the reactive species were combined and subjected to mixing similar to that produced by the PHE) is sufficient. It is important to verify if the numerical model developed in this study and the experiments performed in this study are able to simulate the representative situation for the total volume of gas production as in the actual AC-based thermal management system. This objective was accomplished by combining solutions of sodium bicarbonate and acetic acid in a beaker while

undergoing vigorous stirring. The time for the frothing produced by the reaction to disappear was recorded, which allowed for the rate constant to be approximately calculated using the integrated 1st order rate equation:

$$[A] = [A]_o \, exp\left\{-\hat{k}t\right\} \tag{98}$$

where [*A*] is the molar concentration of acetic acid at time *t* after the two solutions are mixed, and $[A]_o$ is the initial molar concentration of acetic acid. Defining the variable $r = [A]/[A]_o$ and taking the logarithm of Equation (98), the rate constant may then be computed:

$$\hat{k} = -\frac{\ln(r)}{\Delta t} \tag{99}$$

where, Δt is the observed time at which the reaction has progressed to a conversion fraction of *r*. At the completion of the reaction, the remaining reactive species will be the one with the highest initial concentration. Letting *B* signify the molar concentration of sodium bicarbonate, one may compute *x* at the reaction's completion:

$$r = \frac{Max([A]_o, [B]_o) - Min([A]_o, [B]_o)}{Max([A]_o, [B]_o)} \tag{100}$$

The results of these calculations are listed in Table 8:

Table 8- Approximate rate constant measurements

V_{water} (ml)	V_{PG} (ml)	V_{acid} (ml)	m_{bicarb} (g)	Δt (sec)	$[A]_o$ (M)	$[B]_o$ (M)	r	k (1/s)
40.0	10.0	10 (10%)	1.009	2.53	0.29	0.20	0.31	0.46
40.0	10.0	10 (10%)	1.008	3.23	0.29	0.20	0.31	0.36
40.0	10.0	10 (10%)	1.002	5.14	0.29	0.20	0.31	0.23
40.0	10.0	10 (10%)	1.000	3.00	0.29	0.20	0.32	0.38
40.0	10.0	10 (10%)	1.007	6.63	0.29	0.20	0.31	0.18
40.0	10.0	10 (10%)	1.006	8.26	0.29	0.20	0.31	0.14
40.0	10.0	10 (10%)	1.007	7.23	0.29	0.20	0.31	0.16
40.0	10.0	10 (10%)	1.007	6.65	0.29	0.20	0.31	0.18
40.0	10.0	10 (10%)	1.001	8.75	0.29	0.20	0.31	0.13
40.0	10.0	10 (10%)	1.005	6.95	0.29	0.20	0.31	0.17
80.0	20.0	10 (10%)	2.001	6.84	0.16	0.22	0.27	0.19
80.0	20.0	10 (10%)	2.001	7.27	0.16	0.22	0.27	0.18
80.0	20.0	10 (10%)	2.005	7.34	0.16	0.22	0.27	0.18

The quantities listed inside parenthesis in the column headed by "V_{acid} " indicate the volume fraction of acetic acid present in the test sample where the values listed in the same column (without parenthesis) indicate the total volume in ml for these samples. There is, again, an implicit assumption contained within these results that the species are perfectly mixed, such that their molar concentration is given by $[S] = M_s/V_{fluid}$, where S is a chemical species, M_s is the total moles of S present, and V_{fluid} is the total volume of solvent within the beaker (water, PG, and liquid concentrated acetic acid). This experiment was conducted in 250 ml beaker with a magnetic stir bar. The average values of the calculated rate constants is 0.23 s^{-1} (these results have a measurement uncertainty of ±92% at a 95% confident level). Notwithstanding the significant level of measurement uncertainty, it is clear from these measurements performed in this study - that the reaction half times are much closer to the claims by Sahoo and Saha [70] of ~ 1 second, which suggests that this is a reasonable approximation.

Fluid Properties

The two major quantities of interest for these experiments are viscosity and density, which are used in computing the Reynolds number, friction factor, and mass flow rate, among other parameters of interest. The density and viscosity of acetic acid are very close to that of water (1.0446 g/ml and 1.056 mPa·s at 25 °C) [70]. Hence, the properties of the acetic acid solution were assumed to be that of pure water at the same temperature. Propylene glycol, in contrast has a viscosity of 46.4 mPa·s [39] at the same temperature, which is significantly higher than that of water (which is 1.00 mPa·s at 20°C) [71]. Also, propylene glycol has similar density to that of water (1.033 g/ml at 23°C [39, 72]).

The dynamic viscosity for different volume fractions of propylene glycol were measured using a Gilmont ™ falling ball viscometer (Thermo Fisher Scientific Inc.), enabling the viscosity of a fluid sample to be calculated based on the following relation,

$$\mu = F(\rho_{ball} - \rho_{fluid})\Delta t \tag{101}$$

where, μ is the dynamic viscosity in mPa·s, F is a constant depending on the type of ball used in the experiments (the instrument manufacturer provides a value of $K = 0.3$ for a type 3 glass ball with a density of 2.53 g/cc) and Δt is the time for the ball to pass between the upper and lower marker lines on the instrument. The measurements were performed at 26°C, and the viscometer tube was held in burette clamps to ensure both vertical alignment and consistency. The measured values for fall times are listed in Table 9. From the fall times shown in Table 9, the average values of viscosity were calculated and plotted in Figure 20. The maximum value of measurement uncertainty is ±6% at 95% confident level. A Gaussian distribution is assumed for estimating the measurement uncertainty since the dominant error is based on visual judgment. The variation in the fluid density with PG volume fraction is very small. The density increase was measured to be 3.1% when the volume fraction increased from 6.4% to 31.5%. The

viscosity was measured to increase by 220% when the volume fraction increased from 6.4% to 31.5%. Therefore, the density of the PG/water mixture is assumed to be invariant with respect to PG volume fraction.

Table 9 – Raw data for falling ball viscometer measurements for different PG/water mixtures

Fall Times Δt (s) vs PG volume fraction (%)				
31.50%	**6.40%**	**8.40%**	**16.80%**	**20%**
45.49	13.24	14.13	18.41	22.57
42.58	13.22	14.02	18.52	22.57
43.04	13.33	14.01	18.57	22.56
43.81	13.29	14.13	18.56	22.41
44.54	13.16	14.06	18.66	22.41
	13.19	14.03	18.57	22.22
	13.43	13.62	18.15	22.19
	13.48	13.77	18.53	22.16
	13.54	13.85	18.45	21.91
	13.39	13.81	18.81	20.99
	13.27	13.88	18.5	20.88
	13.31	14.02	18.79	22.04
				20.37
				21.27
				21.34
				21.31
				20.9
				21.02
				21.53
				21.59

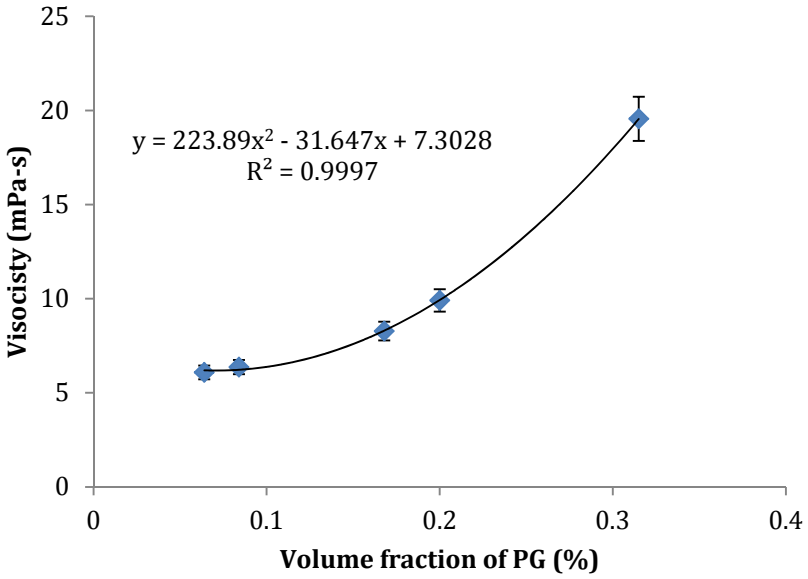

Figure 20 – Viscosity of PG and water mixture as a function of PG volume fraction, as calculated from averages in Table 8

Experimental Facility

The experimental apparatus consists of an Alpha Laval M3 gasket plate heat exchanger with a transparent window, a high-speed video camera, digital (computer) flow loop controller and digital data acquisition system. The relevant dimensions for the PHE are listed in Table 10. A photograph of the front view of the testing rig with attached pressure transducers and window assembly as well as the PHE (in vertical orientation) are shown in Figure 21.

Table 10 – Plate geometric characteristics for M3 plates used in experiments

Λ (mm)	11.0
D_e (mm)	4.68
β (deg)	30
L_{pp} (mm)	323.6
L_c (mm)	275
W (mm)	94.3

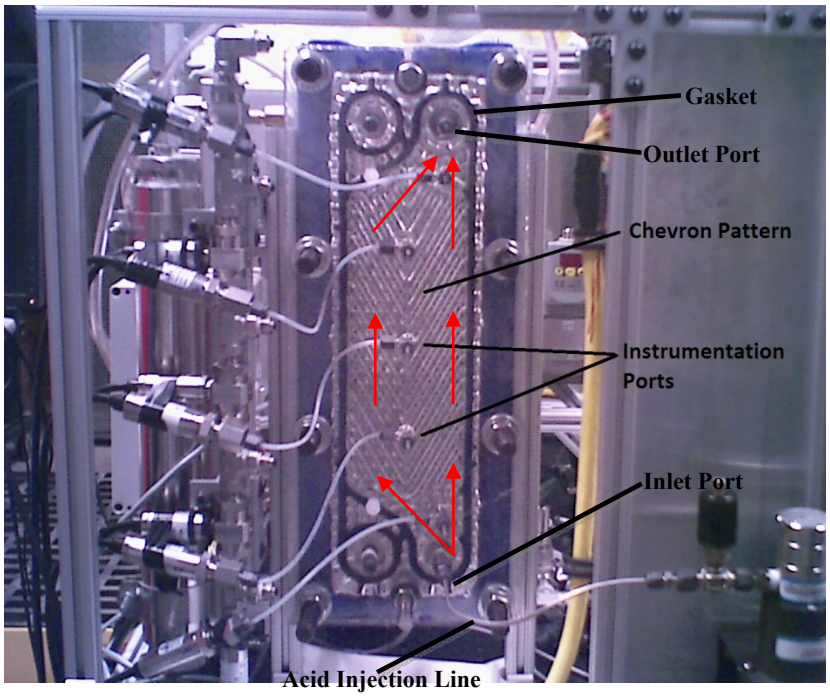

Figure 21 - Front view of PHE apparatus; red arrows illustrate flow path

A diagram representation of the flow and instrumentation network of the test rig is displayed in Figure 22:

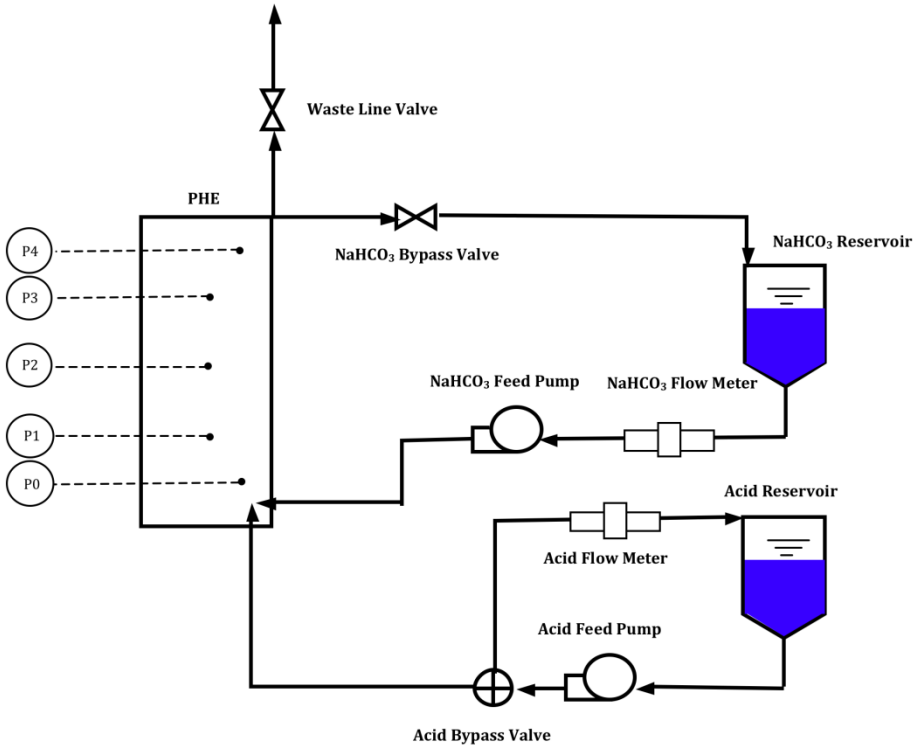

Figure 22 - Test rig piping and instrumentation diagram. The circle elements P0, P1, P2, P3, and P4 represent pressure transducer ports

Sodium bicarbonate solution (with a propylene glycol and DI water mixture as the solvent) is supplied by the "bicarb" feed loop, and fed into the heat exchanger through the inlet port labeled in Figure 21**.** Similarly, a dilute solution of acetic acid is supplied by the acid feed loop and is injected through a port in the window centered over the heat exchanger inlet port. The line used to inject the acid is fed through the window port and bent such that it discharges along the main flow direction on the right half of the chevron plate. Such an arrangement avoids the potential problem of injecting back into the bicarb feed line, which would create additional flow resistance for the bicarb feed pump and prevents the reaction from starting before the flow reaches the heat exchanger.

The ratio of reacting species can be adjusted by varying the respective speeds of the feed pumps (Tuthill DGS centrifugal pumps). The speeds are varied using a 10-turn potentiometer that is attached to each pump controller. This also enables the Reynolds number to be varied systematically. Each flow loop also features a turbine flow meter (FTB 2002), which is used to set the flow rates for each fluid loop. Five pressure taps are fabricated along the length of the window. Five absolute diaphragm pressure transducers with a 50-PSI ceiling are connected to the five pressure taps (Omega Instruments PX 409-050 A5V).

A digital data acquisition system is used to record the data from the flow meters and pressure transducers. The digital data acquisition system is comprised of the SCXI series data acquisition cards (SCXI 1102 analog voltage in for the pressure transducers and SCXI 1126 for the flow meters) and LabVIEW virtual instrument (VI) control software (National Instruments). The pumps are activated from the VI by a digital out signal from an SCXI 1161 card. A high-speed digital image acquisition apparatus is used for flow visualization (consisting of Vision Research Phantom V4.2 camera with a 100 mm Karl Zeiss Macrovision lens, and is controlled remotely through Vision Research's Phantom 630 software).

The window was fabricated in-situ using an acrylic casting resin (Electron Microscopy Sciences), and measures ½" in thickness. The chevron pattern on the window is formed by using a mold constructed with one of the PHE plates. This material is soft and easy to manipulate, but unfortunately presents some difficulty in replicating the heat exchanger conditions when fully compressed; namely, only ~15 N·M of torque can be applied to the six compression bolts, meaning that the clearance between the lower plate and the window chevron pattern is greater than nominal (which requires ~150 N·M of torque to fully compress the gasket). To determine if this shortcoming would have a drastic effect on the flow patterns; nitrogen was injected through the inlet while water was fed through the bicarb loop. During the test, the bubbles were observed

to follow a zig-zag pattern, consistent with expectations for low chevron angle PHEs [10-12]. Hence the overall flow pattern is not expected to be affected, although the observed friction pressure drop values may be less severe than in the case of a fully compressed gasket. Another impediment to operating at elevated pressure is the propensity for this material to deform and allow for liquid to escape around the gasket, especially around the second set of inlet/outlet ports, which are unused in this experiment. This was partially obviated by incorporating steel H-brackets to straddle the width of the plate. Pressure screws were used for applying additional compression to these areas. This modification to the apparatus is shown in Figure 23.

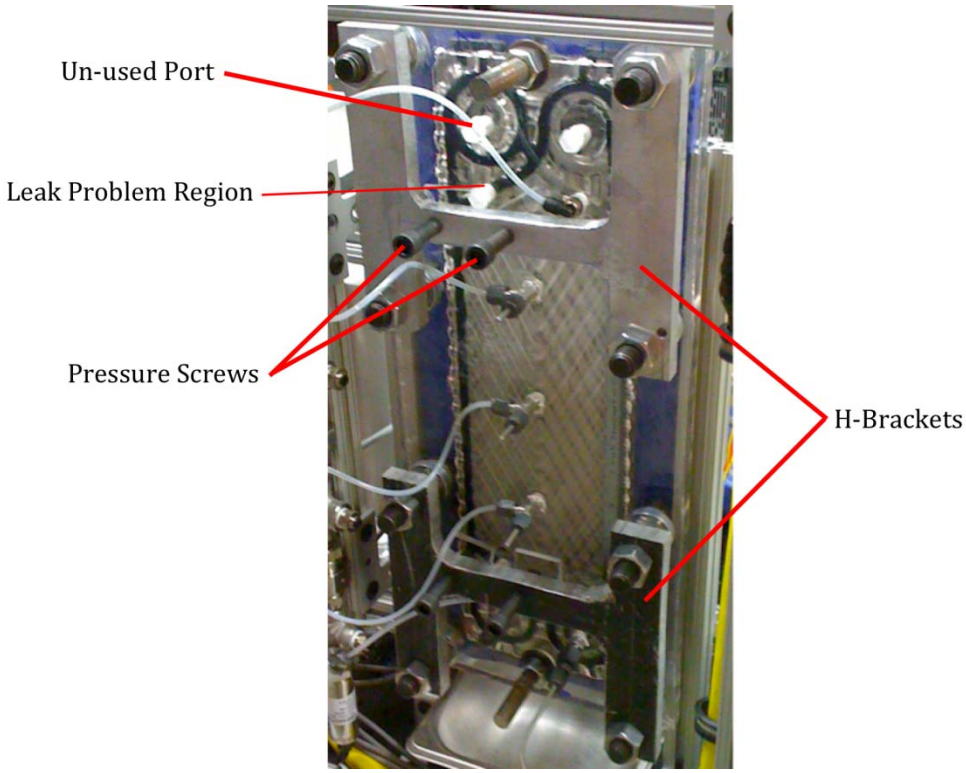

Figure 23 - Photograph of H-brackets and pressure screws to limit compliance of window at problematic leak regions

Additional measures to limit the back pressure in the heat exchanger, such as using large diameter tubing and valves on the flow segments following the heat exchanger outlet (i.e., the waste line and bicarb bypass line and their respective valves) were also proven effective at reducing the likelihood of leaks developing in these particular areas. Similar flow visualization studies reported in the literature involved other types of materials – such as polyester plates [58], Plexiglass (with an embossed chevron pattern) [53, 56], plastic [11], polyurethane resin [14], and acrylic [12].

It was found that high concentrations of acetic acid (>10%) would dissolve the window material. This issue can be surmounted by using dilute acetic acid solutions and applying a transparent sacrificial barrier to the window surface in contact with the chemicals. For this study, a thin layer of commercial carcanuba wax was applied to the window surface. After several tests were conducted, the wax layer was stripped using domestic window cleaner, and reapplied before the next series of tests were initiated.

Testing Procedure

Experiments were conducted under adiabatic conditions with the heat exchanger configured for a single channel. The experiments were performed by systematically varying the Reynolds number for different ratios of sodium bicarbonate to acetic acid molar flow rates. This was accomplished by varying the relative proportion of propylene glycol to water, and by adjusting the speed of the feed pumps for acid and bicarb. For all test runs, the pressure data was recorded from the five transducers (P0-P4); the clock time on the high speed camera was synchronized to the digital data acquisition. This enabled comparison between the high-speed video footage and the pressure as well as flow rate data, during post-processing of the experimental results.

System Assembly and Preparation

Sodium bicarbonate (Sigma Aldrich, 99% purity, powder form) at a concentration of 20 g/L was dissolved in a mixture of water and propylene glycol (Sigma Aldrich, 99%). After the conclusion of a set of experiments, the window and plate surfaces were thoroughly cleaned. Also the remaining silicone sealant on the gasket was stripped; a fresh layer was applied immediately preceding window installation to help ensure a watertight seal on the plate periphery in the absence of high compression around the gaskets. All tubing, pumps, and flow meters were also flushed with de-ionized water to remove the contaminants.

Once the window was mounted and secured, the pressure transducers were connected, the bicarb bypass valve was opened and the bicarb feed pump was run at low speed to fill the chamber. During initial filling, a low pump speed was used to prevent aeration of the fluid as the air within the lines was displaced. Pores on the window have a tendency to "capture" bubbles, and obstruct the optical access required for flow visualization. However, these bubbles can be dislodged by gradually increasing the rate of bicarb circulation until the adhered bubbles are removed. The bicarb solution was allowed to circulate continuously to ensure a well-mixed solution and to prevent the window from fogging. Fogging was observed to occur when fluid was allowed to rest within the chamber.

Testing Cycle

With both the acid and bicarb bypass valves open, the pump speeds were adjusted to their desired set point and allowed to stabilize, during which time the camera and illumination apparatus were adjusted. Once the flow visualization apparatus was ready the set points on both pumps were adjusted and the pumps were stopped momentarily. The bypass valves on both the acid and bicarb flow loops were closed, and the waste outlet line was opened. The experiment was started using VI controller, which triggered the acid and bicarb pumps simultaneously (at

the same instant), and the camera recording was also triggered. Images were recorded by the camera at 1000 frames per second for the whole duration of the test. After ten seconds elapsed, the VI automatically stopped the acid pump while the bicarb pump continued to operate for a few more seconds before stopping subsequently. To ensure that no reacted mixture remained in the heat exchanger, the bicarb pump was run for a few additional seconds to completely purge the chamber. The bypass valves for both flow loops were opened and the waste line was closed before re-activating the bicarb feed pump. This procedure was repeated twice for each test series.

Instrument Calibration

Prior to commencing the experiments, the flow meters were calibrated by opening the bypass valve and collecting the flow from the return line in a beaker that was placed on a digital balance. The mass accumulated on the balance as a function of time was logged in the VI. This was used to obtain the frequency versus mass flow rate curves. Identical calibration procedures were implemented for both the acid and bicarb flow meters. The results showed that the acid pump (which had the highest flow restriction due to the small diameter of the injection line) was capable of pumping at a stable flow rate (for a fixed potentiometer setting) at volumetric flow rates above ~0.01 L/s. Maximum flow rates were measured to be 0.06 L/s and 0.03 L/s for the bicarb and acid pump respectively.

Uncertainty Analysis

In general, sources of experimental uncertainty may be classified as either bias errors, which are inherent in the instrument reading, or statistical errors, which arise from the random temporal variation of an experimental variable. The statistical uncertainty was quantified in the conventional fashion by assuming that random variations in the flow rate and pressure readings

follow a Gaussian distribution. Thus, at a 95% confidence level, the uncertainty for an experimental variable w may be estimated as:

$$\Delta w = \pm 1.96\sigma_w \tag{102}$$

where, σ_w is the standard deviation associated with the average value of w. This method was also used to estimate the uncertainty for the flow meter readings, since they were calibrated by performing a linear regression on time-averaged readings which were due to both fluctuations in the pump output and the uncertainty of the flow meter itself. In this case, Equation (102) is modified by assuming that the deviations from the calibration curve follow a Gaussian distribution, which gives the following estimate for the uncertainty:

$$\Delta w = \pm\left(1.96\sigma_w + \overline{w}\right) \tag{103}$$

where, $\overline{w}$ is the mean absolute deviation from the calibration curve. The bias uncertainties associated with the flow meter and pressure transducer readouts are shown in Table 11, and the uncertainties associated with the experimental parameters used in the following calculations are shown in Table 12(a comprehensive tabulation is provided in Appendix B).

Table 11 – Instrument bias uncertainties

Instrument	Uncertainty (±)	Method
Pressure Transducers	0.2 %	Provided by manufacturer
Acid Flow Meter	6.5%	Equation (103)
Bicarb Flow Meter	0.07%	Equation (103)
500 mL Grad. Cylinder	0.5 %	1/2 smallest graduation
10 mL Grad. Cylinder	0.1%	1/2 smallest graduation

Table 12 – Total uncertainties of select experimental parameters

w	$\Delta w/w$	Source
ρ	3.1 %	Max variation over range of PG concentrations tested
μ	6 %	Equation (103) and Figure 20
D_e	2.1 %	± 0.1 mm calipers
L	1.0 %	± 1.0 mm calipers
$\rho g L$	3.3 %	Equation (106)

Quantities derived using calculations from multiplicative formulas, such Reynolds number and molar concentration, required the use of Equation (104) to estimate the uncertainty propagation:

$$\left(\frac{\Delta w}{w}\right)^2 = \sum_i^I \left(\frac{\Delta x_i}{x_i}\right)^2 \tag{104}$$

where, x_i is the i-th independent variable involved in the computation of w. For quantities involving a linear combination of uncertain quantities, such as pressure drop, the following relation is used:

$$\frac{\Delta w}{w} = \frac{\sum_{i}^{I} \Delta x_i}{\sum_{i}^{I} x_i} \tag{105}$$

This is also known as the Kline-McClintock method [72]. Equation (104) was used to estimate the uncertainty of the pre-mixed acid and bicarb solutions, which are shown in Table 13. The total uncertainty for experimental variables subjected to both bias uncertainties and statistical uncertainties were estimated with Equation (106) as follows:

$$\frac{\Delta w_{total}}{w} = \sqrt{\left(\frac{\Delta w_{bias}}{w}\right)^2 + \left(\frac{\Delta w_{stat}}{w}\right)^2} \tag{106}$$

where, $\Delta w_{bias} / w$ is the uncertainty in the value reported by the instrument and $\Delta w_{stat} / w$ is the uncertainty due to time averaging computed with Equation (102). Combining these two uncertainties in this fashion is permissible since they are both independent random variables. Equation (106) is used for estimating the uncertainty in the pressure and flow rate data.

Table 13 – Pre-mixed solution uncertainties

Variable	Uncertainty (±)
PG Mixture Strength	0.44 %
Acid Solution Strength	0.60 %
Bicarb Solution Strength	0.13 %

The PG/water solution was mixed in 4 L batches using the 500 mL graduated cylinder to dispense both the water PG into a 4 L Erlenmeyer flask. To account for the fact that the graduated cylinder had to be filled several times to dispense the proper amount of fluid, each fill was treated as an independent variable. Hence, for a 20% PG/water mixture, Equation (104) yields:

$$\Delta\dot{x}_{PG} = \frac{N_{pours}\Delta w_{500mL}}{\left(4.00L\right)} \tag{107}$$

where, N_{pours} is the number of times the 500 mL graduated cylinder was filled to dispense the required amount of water and PG, and Δw_{500mL} is the uncertainty associated with any given reading of the 500 mL cylinder. The acid solution was mixed in 1 L batches by dispensing the glacial acetic acid with the 10 mL graduated cylinder, and the water with the 500 mL graduated cylinder. The bicarb solution was mixed by measuring 20 g of $NaHCO_3$ powder using a digital balance, and then dispensing the powder into the previously mixed 4 L batch of PG/water solution. The uncertainty in the mass measurement was estimated to be +/- 0.10 g, approximately twice the mass of $NaHCO_3$ residue in the weighing boat after the bulk of the powder was transferred to the PG/water solution.

For the following analysis let the uncertainty associated with an experimental variable w be recast as:

$$\varepsilon_w \equiv \frac{\Delta w}{w} \tag{108}$$

The total uncertainty for the total pressure drop (ΔP_{tot}) may be calculated as:

$$\varepsilon_{\Delta P_{tot}} = \frac{P_1\varepsilon_{P_1} + P_3\varepsilon_{P_3}}{\Delta P_{tot}} \tag{109}$$

where, for the k-th pressure transducer:

$$\varepsilon_{P_k} = \sqrt{\left(\varepsilon_{P_k}\right)_{bias}^2 + \left(\varepsilon_{P_k}\right)_{stat}^2} \tag{110}$$

It follows that the total uncertainty for the frictional pressure drop is:

$$\varepsilon_{\Delta P_F} = \frac{\Delta P_{tot}\varepsilon_{\Delta P_{tot}} + \rho g L \varepsilon_{\rho g L}}{\Delta P_F} \tag{111}$$

where:

$$\Delta P_F = \Delta P_{tot} - \rho g L \tag{112}$$

From the single-phase pressure data, the uncertainty range on the total pressure drop is 21% ≤ ε ≤ 25%, with an average uncertainty of 24% Applying Equation (111) to the single phase frictional pressure drop, one obtains an average uncertainty of ~±300%, with a range of 124% ≤ ε ≤ 3700%. Applying the above procedure for the single-phase friction factor, the corresponding uncertainty is:

$$\varepsilon_f = \sqrt{4\varepsilon_{\dot{V}_{tot}}^2 + 9\varepsilon_{D_e}^2 + 4\varepsilon_W^2 + \varepsilon_{\Delta P_F}^2 + \varepsilon_\rho^2 + \varepsilon_L^2} \tag{113}$$

The result of this calculation is an average uncertainty of ±300% and a range of 124% ≤ ε ≤ 3700%. Table 14 tabulates the computed total uncertainty values over each test series to be described in the following section:

Table 14 – Total relative uncertainties (ε) calculated for each two-phase experimental series

Series	$\dot{V}_{acid}$	$\dot{V}_{bicarb}$	$\dot{V}_{total}$	ΔP_{tot}	P1	P3	Re
A1	14	3.1	4.9	630	6.0	6.0	8.4
A4	16	4.4	7.0	410	3.9	3.8	9.7
A5	6.2	0.4	1.3	300	3.1	3.2	6.9
A6	14	3.2	4.8	120	1.0	1.1	8.3
A7	6.5	1.5	2.3	170	1.4	1.4	7.1
A8	7.9	3.8	5.2	310	2.5	2.4	8.5
A9	7.4	3.1	4.6	300	2.4	2.3	8.2
B1	16	4.3	6.7	680	6.0	5.8	9.5
B2	14	4.7	6.8	790	6.4	6.3	9.6
B3	16	4.4	7.0	380	3.9	3.8	9.7
B4	10	3.5	4.9	370	3.7	3.7	8.4
C1	6.7	3.0	4.5	440	2.6	2.6	8.2
C2	7.7	3.2	5.0	480	3.0	3.0	8.4
C4	7.3	3.7	5.1	240	1.5	1.5	8.5
D1	13	2.3	4.7	310	2.4	2.5	8.2
D2	18	2.1	5.8	340	2.9	2.9	8.9
D3	16	4.9	8.1	580	4.0	4.1	11
D4	8.5	2.1	4.1	170	1.3	1.2	7.9

Results

Single-phase Pressure Drop Tests

In order to establish a base-line for the study, experiments were performed spanning the entire range of achievable Reynolds numbers (from a single pump acting alone). The experiments were performed using mixtures of propylene glycol and water (at different ratios) to achieve different values of *Re*.

Considerable difficulties were encountered for measuring the frictional pressure drop since the system was restricted to low flow rates. In such a situation the gravitational component of the pressure gradient is the major contributor to the total pressure drop. Consequently, all the

calculated values of frictional pressure drops (both for the port-to-port length and the center corrugated length) lie within the uncertainty margin of the pressure transducers (± 0.2 kPa). Hence, any friction factor correlation derived from the data would be associated with a wide range of spread in error. Nevertheless, a comparison of the single phase friction factor calculated from experimental runs with 20% and 31.5% PG/water mixtures and those predicted by Martin's [41] and Fernandes *et al.*'s [46] correlations are presented in Figure 24. The pressure transducers covering the corrugated section are spaced approximately 150 mm apart, and with the fluid density known, the gravity pressure drop can be calculated and subtracted from the total measured total pressure drop to obtain the frictional component. The friction factor is subsequently calculated using Equation (24) (with the value of two-phase multiplier set to 1). In this instance the superficial velocity is computed from the mass flow rate and overall cross sectional area. Both correlations follow approximately the same Reynolds number dependence as the experimental data, but consistently over-predict. It is reasonable to ascribe this disagreement to the low torque placed on the compression bolts, since this would create greater than nominal plate spacing, and hence lower hydraulic resistance. The correlations from the literature, conversely, are based on experimental data with fully-compressed gaskets. Attempting a curve fit to the data of the form $f=C/Re$ yields the following correlation:

$$f = 24\,\mathrm{Re}^{-1} \tag{114}$$

This correlation reproduced the single-phase experimental data with an average deviation of 23% and a maximum deviation of 420% at a 95% confidence level, provided $8 \leq Re \leq 70$. There is slight mismatch between the data points for the 31.5% PG solution and the 20% PG solution in the range of $25 \leq Re \leq 35$, but it does not appear to be significant compared to the spread in the data in this range. The discrepancies are probably due to the fact that the data sets for both

solutions were obtained on different days, between which the test rig had to be disassembled and cleaned. This could have caused variations in geometric parameters for the experiments.

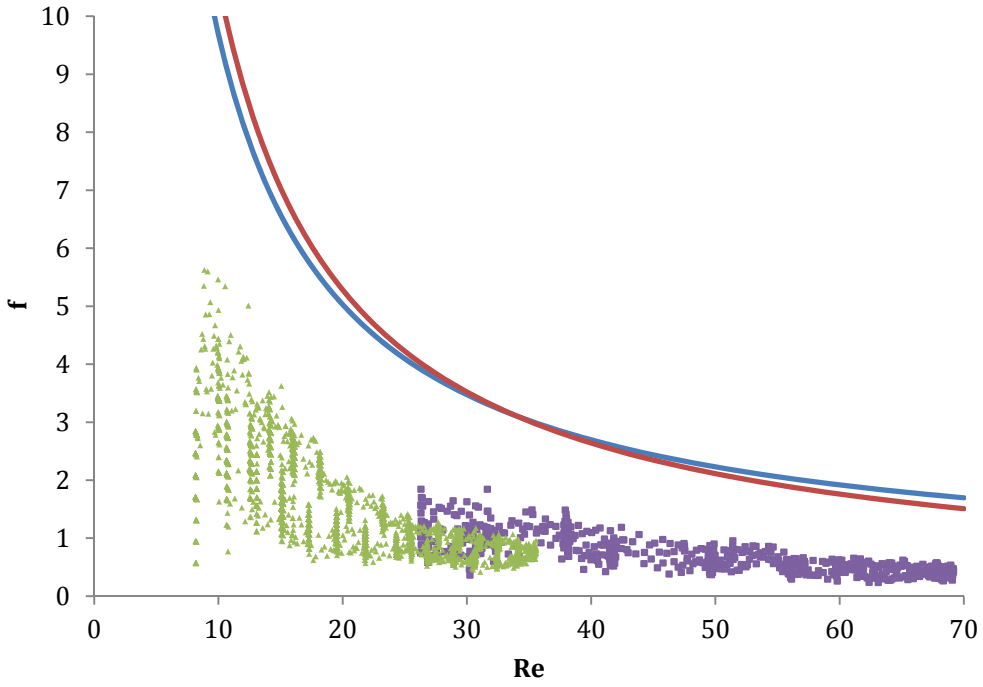

Figure 24 - Total frictional pressure drop over the chevron pattern compared with predictions from Martin's (red line) and Fernandes *et al.*'s (blue line) correlations. Percentage of PG was adjusted to extend range of Reynolds numbers covered by the data: 20% (purple) and 31.5% (green)

Due to limitations in the pressure transducer resolution, it was not possible to discern with a reasonable degree of certainty any variation in the spatial character of the pressure fields as *Re* was varied – the only visible difference that occurs is the rise in absolute pressure that occurs as the flow rate is increased due to the hydraulic resistance of the outlet line and valve. Figure 25 shows typical axial pressure distributions measured during the single phase experiments for both PG/water mixtures at a fixed flow rate.

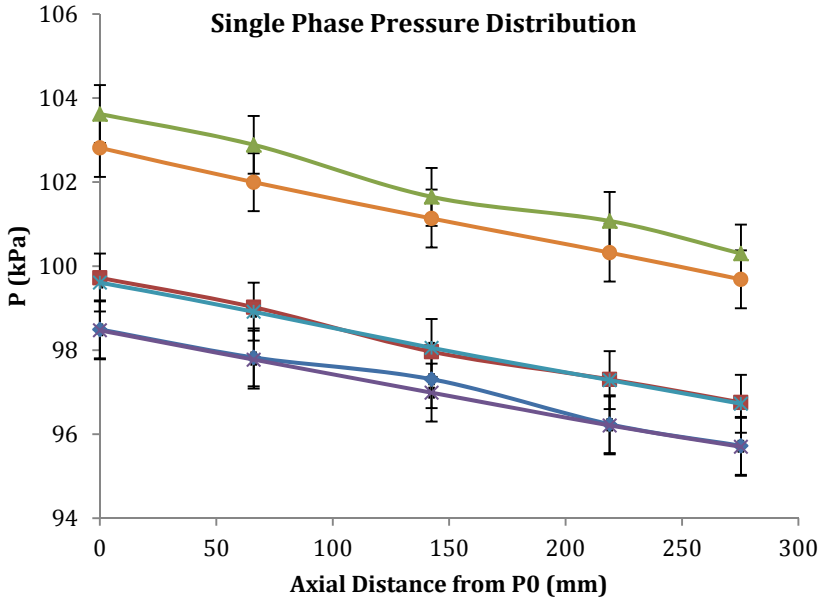

Figure 25 – Absolute pressure readings for representative single phase flow tests with both 31.5% and 20% PG/water mixtures. Each dot corresponds to the location of a pressure transducer relative to the position of transducer P0

Two-phase Pressure Drop Tests

Pressure drop and absolute pressure measurements obtained from experiments involving flow-mixing and chemical reaction between acetic acid and bicarbonate solutions are presented in the following section. The test matrix is displayed in Table 10, where PG strength is the volume fraction of propylene glycol used in the PG/water mixture, and acid strength is likewise the volume fraction of acid in the dilute acid solution. The Reynolds number is adjusted to account for the fact that the effective volume fraction of PG to water, and hence the viscosity, changes when both solutions are introduced into the chamber. This is accomplished by determining the new PG volume fraction, $\dot{x}'_{PG}$, from a simple mass balance as follows:

$$\dot{x}'_{PG} = 1 - \frac{\dot{V}_{PG\ Solution}}{\dot{V}_{total}}\left(1 - \dot{x}_{PG}\right) - \frac{\dot{V}_{Acid\ Solution}}{\dot{V}_{total}} \tag{115}$$

where, $\dot{x}_{PG}$ denotes the nominal volume fraction of the PG/water mixture before it is fed into the chamber. The viscosity of the new mixture can then be estimated using the curve fit equation shown in Figure 20, assuming the characteristic mixing time scale is much smaller than the bulk flow time scale – a reasonable assumption since the mixing length scale is ~D_e, whereas the bulk flow length scale is ~L_c.

Table 15 - Test Matrix

Test Set A						
Test Series	**A1**	**A3**	**A4**	**A5**	**A6**	**A7**
Acid Strength	5%	5%	5%	5%	2.35%	2.35%
Bicarb Loading (g/L)	20	20	20	20	25	25
PG Strength	20%	20%	10%	10%	10%	10%
Total flow rate (L/s)	0.064	0.072	0.074	0.065	0.041	0.032
Re	76	83	121	102	66	51
Cin, Acid (mol/L)	0.14	0.13	0.13	0.14	0.14	0.14
Cin, Bicarb (mol/L)	0.20	0.20	0.20	0.20	0.20	0.20
Test Set B						
Test Series	**B1**	**B2**	**B3**	**B4**		
Acid Strength	5%	5%	5%	5%		
Bicarb Loading (g/L)	20	20	20	20		
PG Strength	20%	20%	20%	20%		
Total flow rate (L/s)	0.058	0.049	0.042	0.070		
Re	71	62	53	86		
Cin, Acid (mol/L)	0.18	0.19	0.20	0.18		

Table 15 Continued

Test Set B					
Cin, Bicarb (mol/L)	0.19	0.19	0.18	0.19	
Test Set C					
Test Series	**C1**	**C2**	**C3**		
Acid Strength	5%	5%	5%		
Bicarb Loading (g/L)	20	20	20		
PG Strength	32%	32%	32%		
Total flow rate (L/s)	0.068	0.055	0.031		
Re	73	57	32		
Cin, Acid (mol/L)	0.35	0.34	0.35		
Cin, Bicarb (mol/L)	0.14	0.14	0.14		
Test Set D					
Test Series	**D1**	**D2**	**D3**	**D4**	
Acid Strength	8%	8%	7%	7%	
Bicarb Loading (g/L)	30	30	31.4	31.4	
PG Strength	10%	10%	25%	25%	
Total flow rate (L/s)	0.063	0.053	0.061	0.037	
Re	100	84	74	43	
Cin, Acid (mol/L)	0.32	0.33	0.37	0.40	
Cin, Bicarb (mol/L)	0.28	0.27	0.26	0.25	

Each set of experiments were designed to achieve a fixed ratio of flow rates for acid and bicarbonate solutions. In instances where large amounts of gas were produced the designed experiments were difficult to implement because of the sudden increase in reactor back pressure. This would force the pumps to operate at slower speeds. Also, active compensation for the changes in pump speeds during the course of each test run was not implemented since the duration of each experiment was only 10 seconds. Each test series was repeated three times, with the exception of test series B4, which was repeated four times, and C2, which could only be repeated once. In all test series, the flow transients that were recorded following pump activation persisted for only a few seconds before pressure readings remained steady, allowing for the

pressure transducer readings to be time averaged. As an example of the temporal dependence of typical pressure transducer and flow meter readings logged during a test run, the results for test series A4 are shown in Figure 26-Figure 28. In these plots, the dotted lines represent, in order of increasing time, the points where the acid pump is activated, the point where "steady-state" is achieved, and the point where the acid pump is stopped.

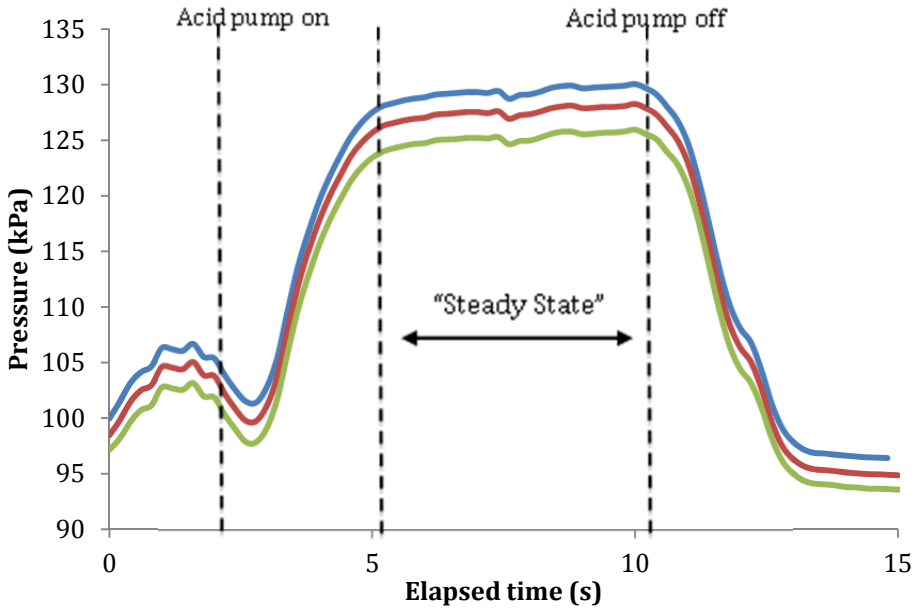

Figure 26- Absolute pressure readings for test series A4

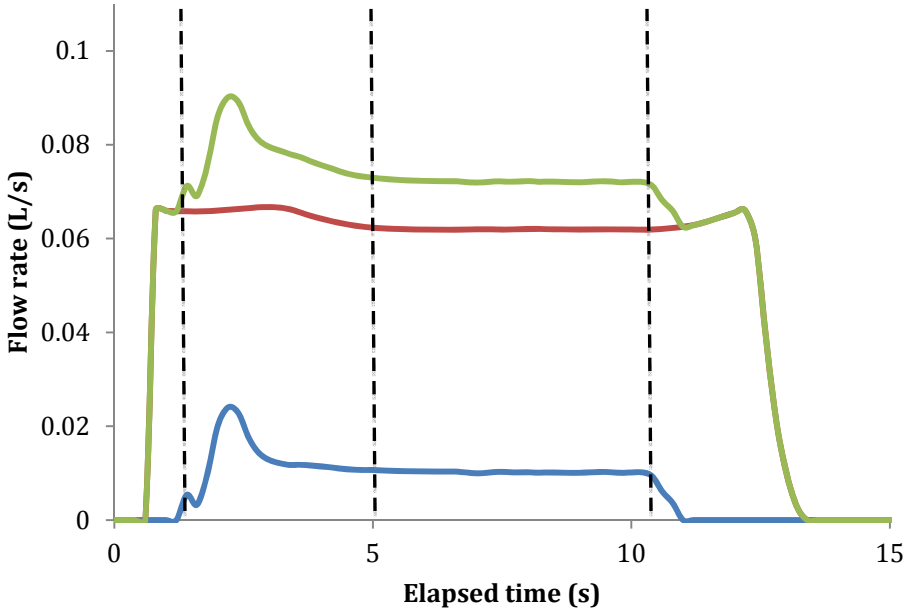

Figure 27- Volume flow rate for acid and bicarb pumps for test series A4

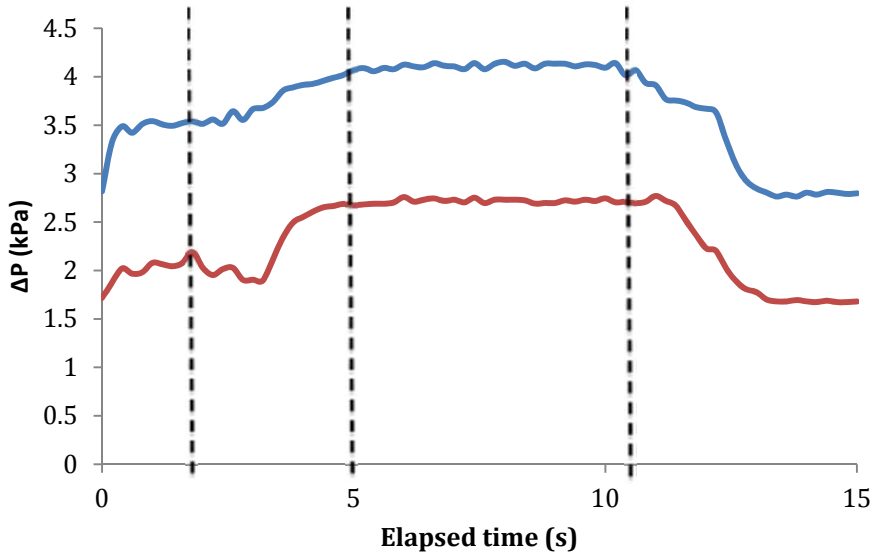

Figure 28- Total pressure drop for the center corrugated section (red line, P1-P3) and from inlet to outlet port (blue line, P0-P4) for test series A4

The same flow characteristics shown above were found to exist in all the experiments performed in this study. Thus, data obtained from the 'plateau' regions are considered to be representative of the system during sustained operation. Figure 26 reveals a significant rise in the absolute chamber pressure that occurs at the onset of reaction, which is large in comparison to the total pressure drop observed across the reactor. In test set A, the back pressure rise can be seen to increase with increasing flow rates, as illustrated in Figure 29. Figure 30- Figure 32 likewise show a similar trend; the time-averaged readings of each pressure transducer presented in Figure 29- Figure 32 are averaged over the three runs for each test series.

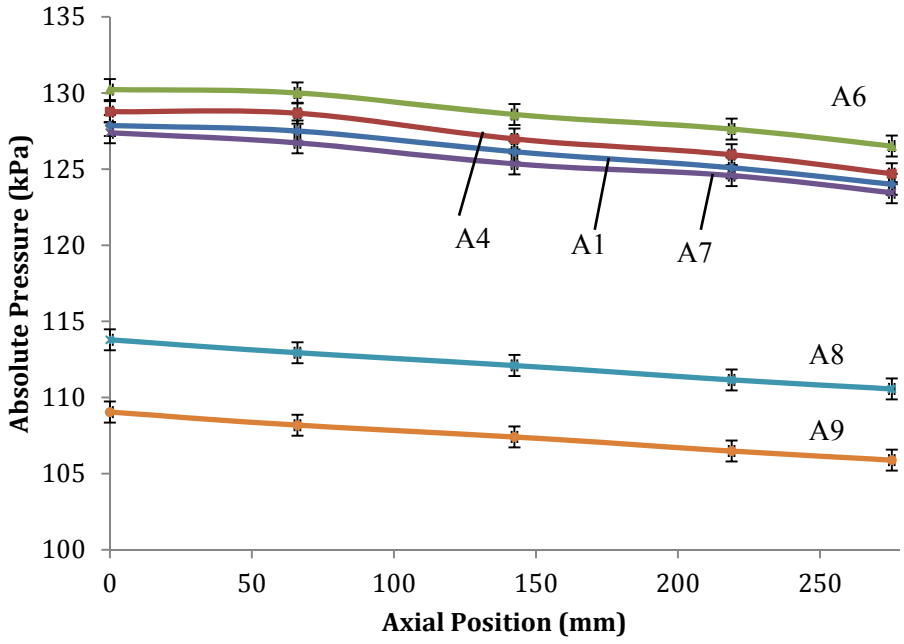

Figure 29 – Absolute pressure versus axial position for test set A

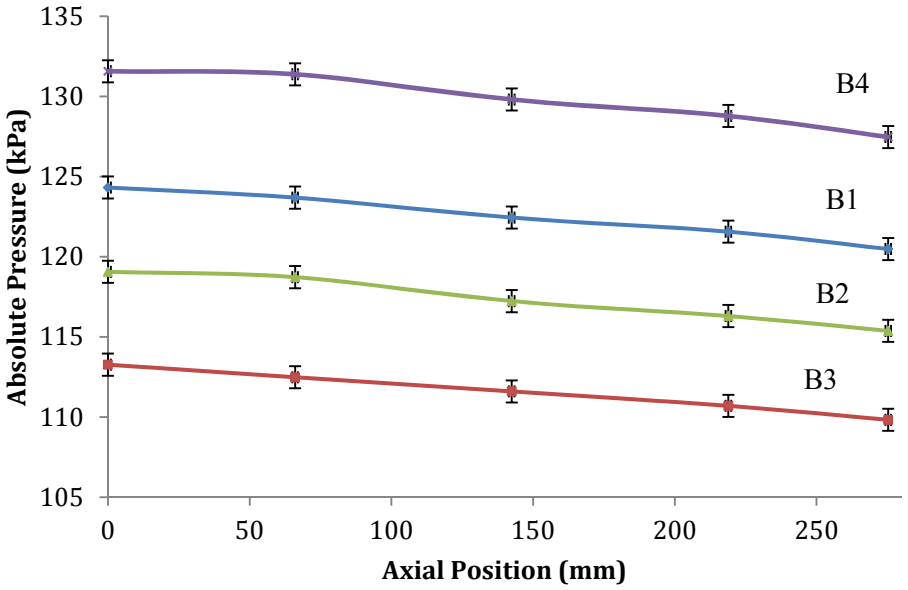

Figure 30 – Absolute pressure versus axial position for test set B

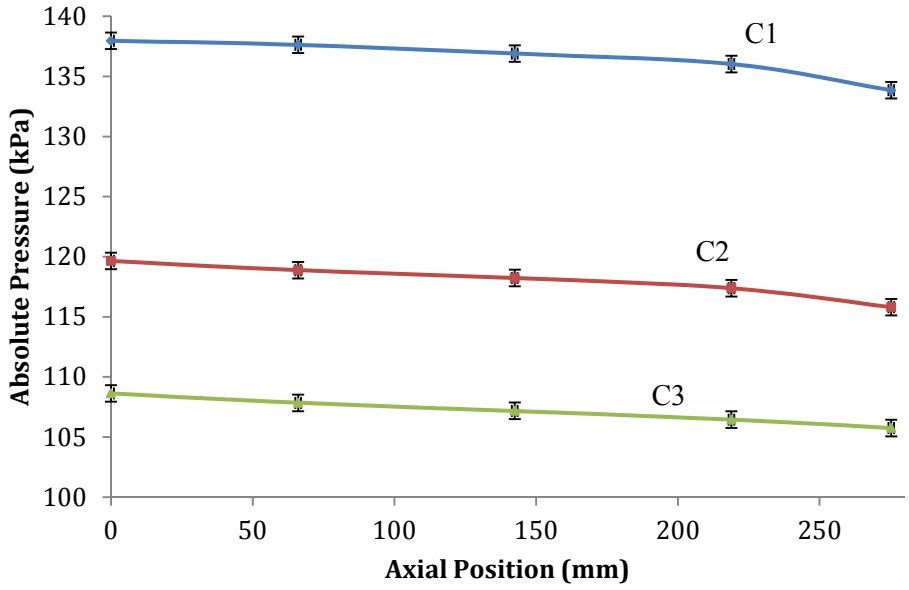

Figure 31 – Absolute pressure versus axial position for test set C

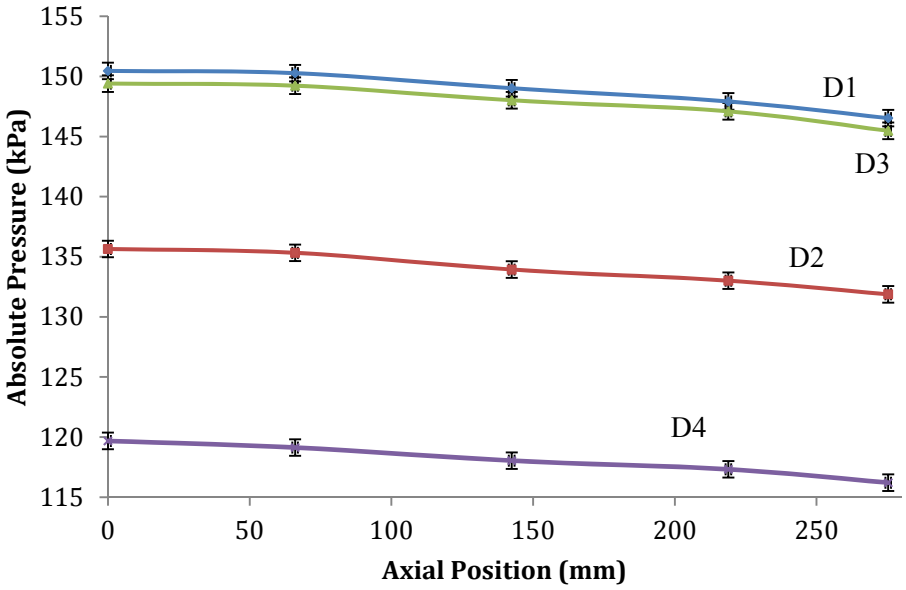

Figure 32 – Absolute pressure versus axial position for test set D

The drastic increase in back pressure, in addition to its close correlation with flow rate, suggests that the total gas evolution within the entire system (reactor and waste line) is directly responsible for this effect. This is observed from the pressure data plots for each test series where the pressure drop is plotted as a function of the molar flow rate of the limiting reactant. All test series on the resulting composite plot adhere to a positive linear trend with respect to molar flow rate, which would occur if the reaction proceeds to completion within either the reactor chamber or subsequently in the waste line. For steady-state, constant volume and isothermal conditions, one would expect the pressure to increase linearly with moles of gas in the chamber, assuming that there is no dissolved gas present.

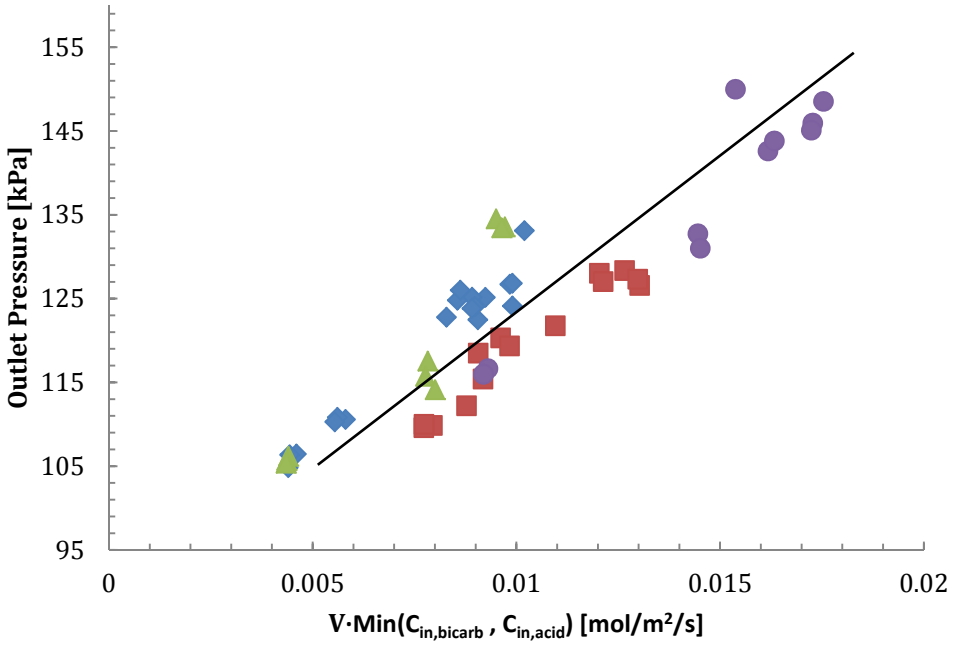

Figure 33 – Reactor back pressure as function of maximum gas flux

Two-phase Multiplier Assessment

Calculating the frictional component of the two-phase flow pressure drop was required for estimating the hydrostatic and acceleration components. This in turn required an estimation of the void fraction:

$$\Delta P_{grav} = \int_{z_0}^{z_4} g\left[\left(1-\alpha\right)\rho_{ls} + \alpha\rho_g\right] dz \tag{116}$$

$$\Delta P_{acc} = \int_{z_0}^{z_4} \frac{\rho_{ls} U^2}{1-\alpha} dz \tag{117}$$

where, the locations z_0 and z_4 represent the axial location of the pressure transducers P0 and P4, respectively. Note that the advective acceleration terms for the gas phase have been omitted from Equation (108) because they of negligible magnitude compared to that of the liquid-phase. In

order evaluate the above integral, it was assumed that the majority of the reaction was completed in the neighborhood of z_0, allowing the void fraction to be treated as a constant. The value of the void fraction was obtained directly from the Rouhani correlation [59] by using the maximum mass quality corresponding to the acid and bicarb flow rates:

$$\Delta P_{grav} \cong \left[\left(1-\bar{\alpha}\right) \rho_{ls} + \bar{\alpha}\bar{\rho}_g \right] (z_4 - z_0) \tag{118}$$

$$\Delta P_{acc} \cong \rho_{ls} U^2 \left[\frac{1}{1-\bar{\alpha}} - 1 \right] \tag{119}$$

The gas density did not change appreciably for the range of pressure drops encountered in this study. Hence the gas density was evaluated for the reference conditions corresponding to the pressure at P4 and room temperature. The density values were calculated using the ideal gas equation of state.

The two-phase multiplier Φ_{TP} was subsequently obtained by dividing the frictional pressure drop for the two-phase experimental data by the single phase frictional pressure drop calculated for liquid flowing at the same Reynolds number, using the single-phase friction factor correlation developed from the single-phase experimental data. These results are plotted in Figure 34 against the Lockhart-Martinelli parameter, defined in Equation (49) :

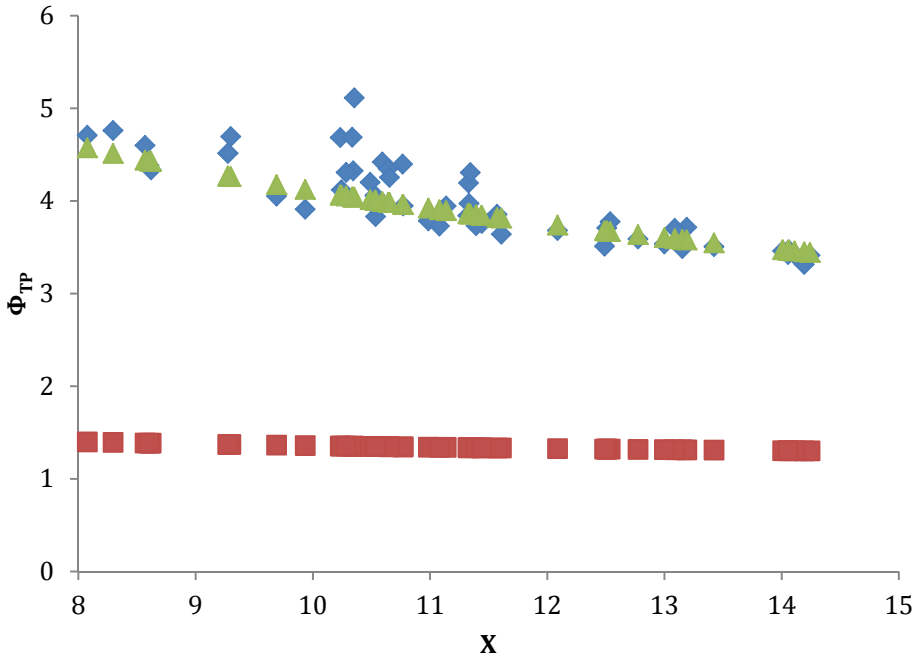

Figure 34 – Two-phase multiplier from experimental data (blue) compared to Equation (48) (red) as a function of the Lockhart-Martinelli parameter. Approximate curve fit shown in green

The experimental data exhibits a steeper downward trend with increasing X compared to the corresponding predictions from Equation (48). The data may be reproduced to within ~21% at a 95 % confidence level by the following equation:

$$\Phi_{TP} = \frac{13}{\sqrt{X}} \tag{120}$$

To compensate for the bias error (under-prediction for the values obtained by correlation), a multiplying factor of 3.0 was applied to Equation (48) . This approach provided reasonably good agreement between model predictions and experimental results given the scatter shown in Figure 34, which will be demonstrated shortly. It is still important to mention that the limited range of values of X is an impediment to deriving any strong conclusions and prevented

the development of a simple multiplier correction that would suffice for the entire range of the parameters and thus limited the applicability of the correlation ($0.06 \leq X \leq 10$). The discrepancy between Equation (48) and the data may be reasonably attributed to the rapidly expanded gases (and additional fluid agitation) arising from the vigorous neutralization reaction. Conversely, the empirical correlation of Tribbe and Müller-Steinhagen was based on experiments where a well-controlled flow rate of air was introduced at the inlet.

Simulations were performed using the numerical model for the experimental values of inlet pressure and molar flow rates for the bicarb and acid flow rates used in the experiments. A rate constant of 20 s^{-1} was assumed, since this allowed the reaction to fully complete within the first 1/3 or 1/2 of the reactor length – as long as the reaction reached completion, the pressure drop predictions were not particularly sensitive to the rate constant. The multiplier correction mentioned previously was applied to the Tribbe and Müller-Steinhagen correlation [59]. This was performed to account for the inlet and outlet distribution zones. Some representative results are shown in Figure 35 and Figure 36.

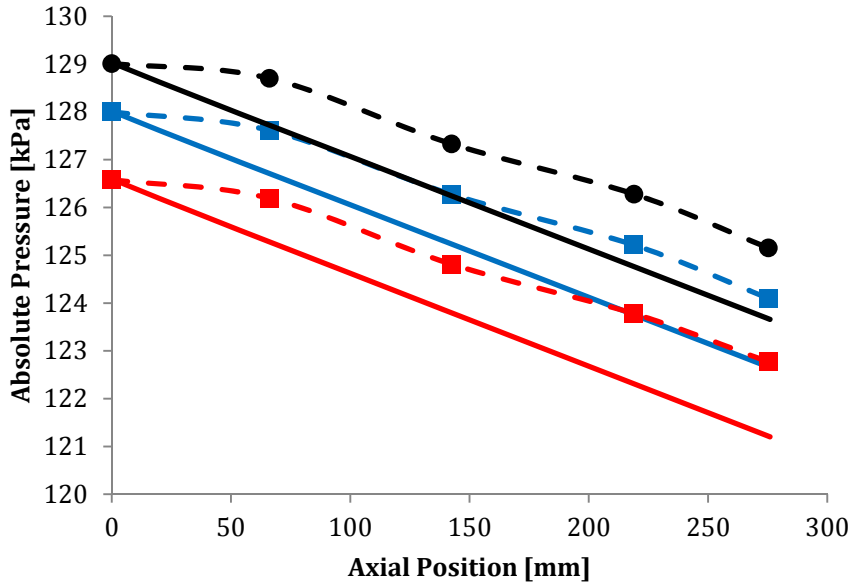

Figure 35 – Comparison of numerical prediction (solid line) to experimental axial pressure profiles (dashed line) for test series A1

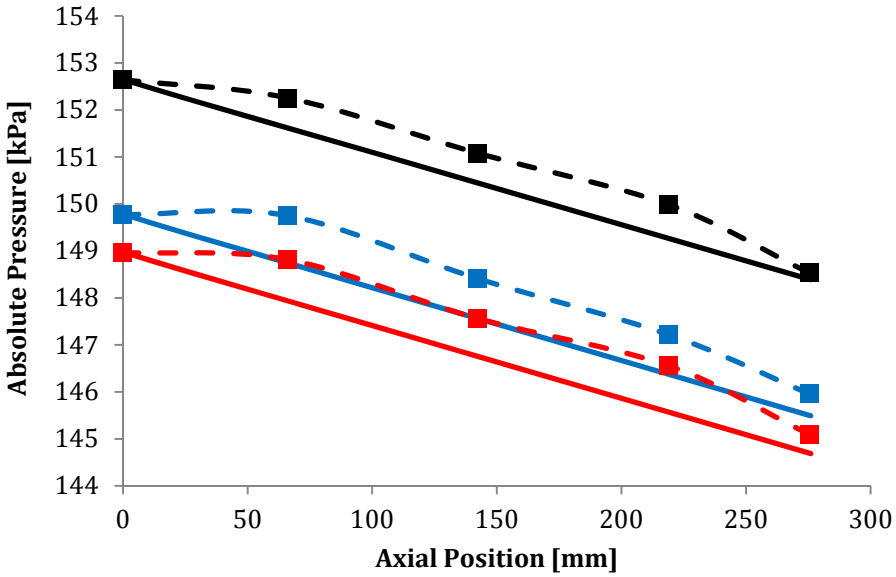

Figure 36 – Comparison of numerical prediction (solid line) to experimental axial pressure profiles (dashed line) for test series D1

The numerical model tended to over-predict the total pressure drop (P0-P4) for most cases, with errors ranging from 0.7% to 48% and an average error of 26%, compared to the experimental results.

Void Fraction Correlation Assessment

Using the absolute pressure readings from transducer P4 and the ambient temperature (26°C), it was possible to use the ideal gas equation of state to predict the density of CO_2 at the reactor outlet, which then allowed the superficial gas velocity at the outlet to be computed. This data, pictured in 37 as a function of total gas phase mass flux (assuming the reaction reaches to completion), could then be used with either the Rouhani [59] or drift flux void fraction correlations [37] to estimate the gas velocity at the outlet. The resulting calculations are plotted as a function of total gas phase mass flux in Figure 38. The corresponding void fraction predictions for Figure 38 are plotted in Figure 39.

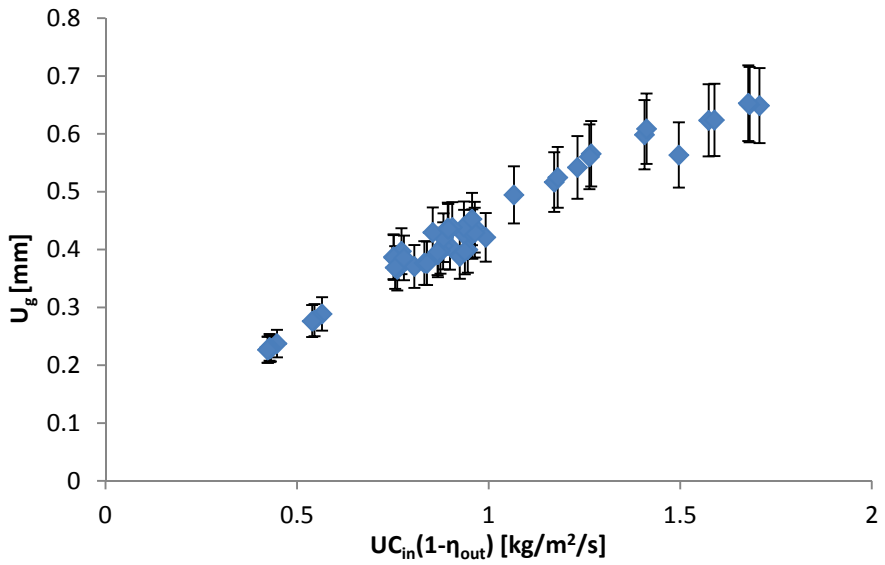

Figure 37 – Gas phase superficial velocity at outlet as a function of gas phase mass flux

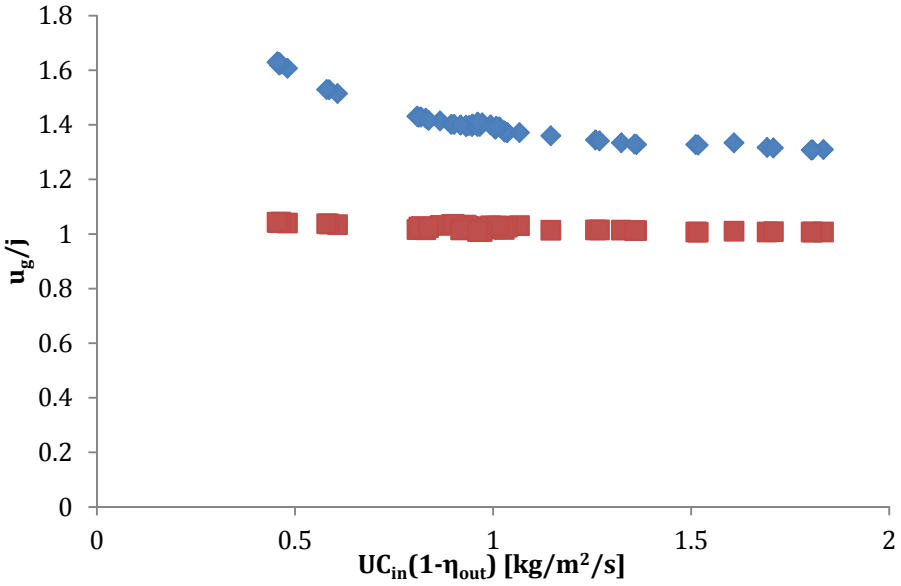

Figure 38- Gas velocity at outlet normalized by total volumetric flux using void fraction predictions from Rouhani correlation (blue) and drift flux model (red)

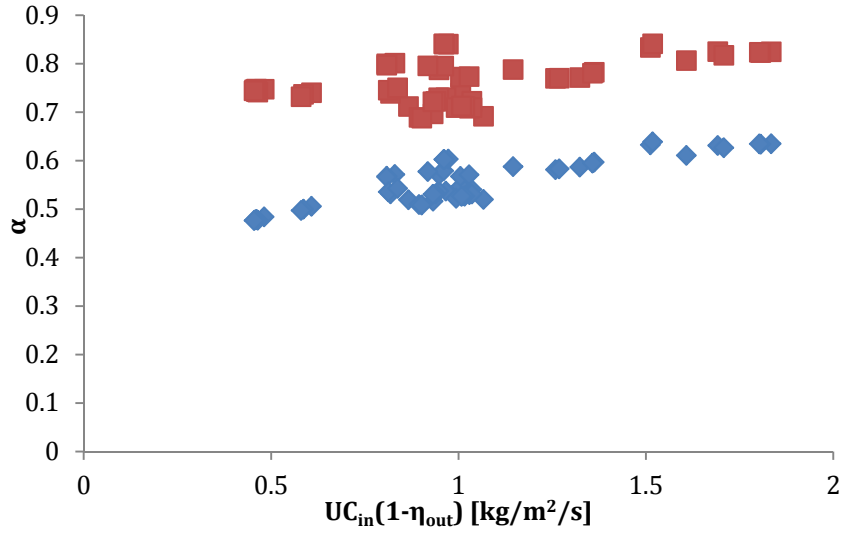

Figure 39 – Void fraction predicted by Rouhani correlation (blue) and drift flux model (red)

The values of pressure, inlet molar concentrations, and flow rate data were used to obtain the plots shown in Figure 37 - Figure 39. These plots were, again, extracted from all test series, assuming the reaction had reached completion by the outlet ($\eta_{out} = 0$); the gas velocity is computed using equation 16. The term 'outlet', refers to the axial location at which the corrugated section terminates and the outlet port distribution zone begins, corresponding roughly to the location of pressure transducer P4. Thus, the cross sectional area at which the velocities are obtained is still the effective plate spacing multiplied by the distance between the edges of the gasket, $A_c = WD_e$. The scatter in both the void fraction and gas exit velocity predictions are more severe for the drift flux model and show only a small variation over the mass fluxes obtained experimentally, much in contrast to the Rouhani correlation [59]. The trends shown in Figure 38 and Figure 39 have better clarity for the Rouhani correlation, which suggests that it may be the more appropriate choice for the model.

Figure 37 exhibits a decreasing slope in the gas superficial velocity at the outlet with increasing mass flux. The immediate interpretation of this trend is that as the amount of gas present in the reactor increases, there is additional hydrodynamic resistance for the bubbles to overcome. The important implication here is that the escape kinetics of the gas products is hindered with their increasing production, leading to larger enhancements in back pressure. Assuming that the largest hydrodynamic resistance occurs in the reactor chamber, adjusting the pressure outside of the reactor may only be effective in reducing the channel pressure up until a limiting point. This limiting point will occur when the hydrodynamic conditions prevailing inside the reactor prevent that gas from escaping at the rate demanded by the pressure gradient created from the imposed outlet pressure. For an AC reactor, this would place a limit on the amount of gas that could be evolved, as further reductions in pressure at the outlet would not produce any decreases in the pressure inside the reactor, constituting a 'choking' condition.

Flow Visualization Results

Video footage was obtained for test sets A-C, and test series D1. For each individual run, the camera was repositioned to a different axial location to the right of the central spine to track the stream-wise evolution of the two-phase flow pattern. Before running the reaction, a reference video was recorded to differentiate pre-existing voids in the window or aeration bubbles, which were found to be much smaller and occurred less frequently than the CO_2 bubbles produced by the reaction. Figure 40 and Figure show screenshots from representative times during 'steady-state' operation. ImageJ 1.45s, a public domain image analysis and processing software developed by the National Institute of Health (NIH), was used for image processing to obtain information about the hydrodynamic behavior for the individual bubbles within the focal plane of the camera. This information was used to track and measure (on a frame-by-frame basis) flow patterns, bubble size distribution, and bubble velocity.

In general, two prevailing flow patterns were observed: foam/froth where the reaction occurred, and dispersed bubbly-flow in areas downstream of where the reaction had ceased. For the purpose of this discussion, the former flow regime is termed as "type I flow", and the latter as "type II flow". Examples of these flow regimes are shown in Figure 40 and Figure 41, respectively.

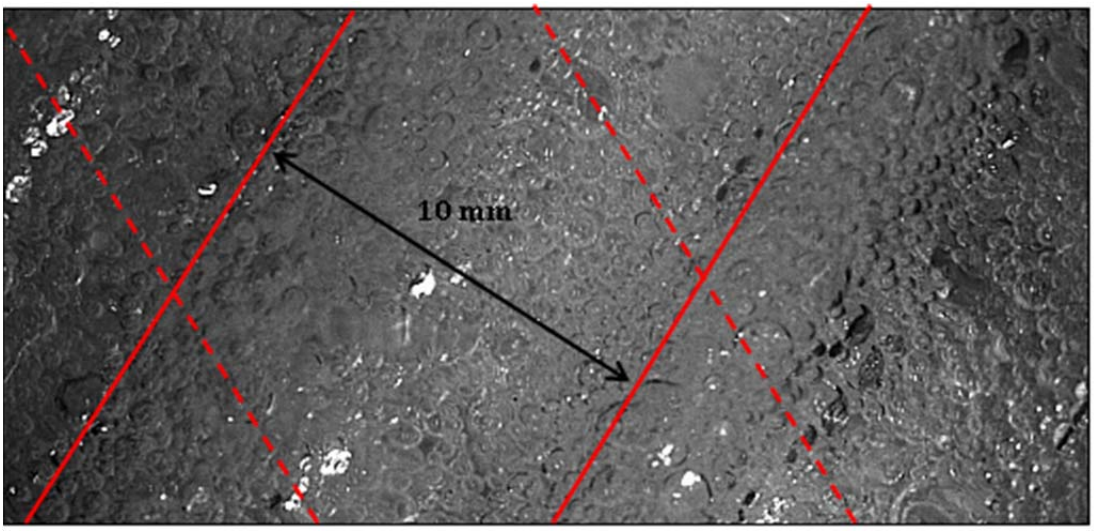

Figure 40 – Test series B3, run 1: axial position between pressure transducer P0 and P1. Typical of type I flow

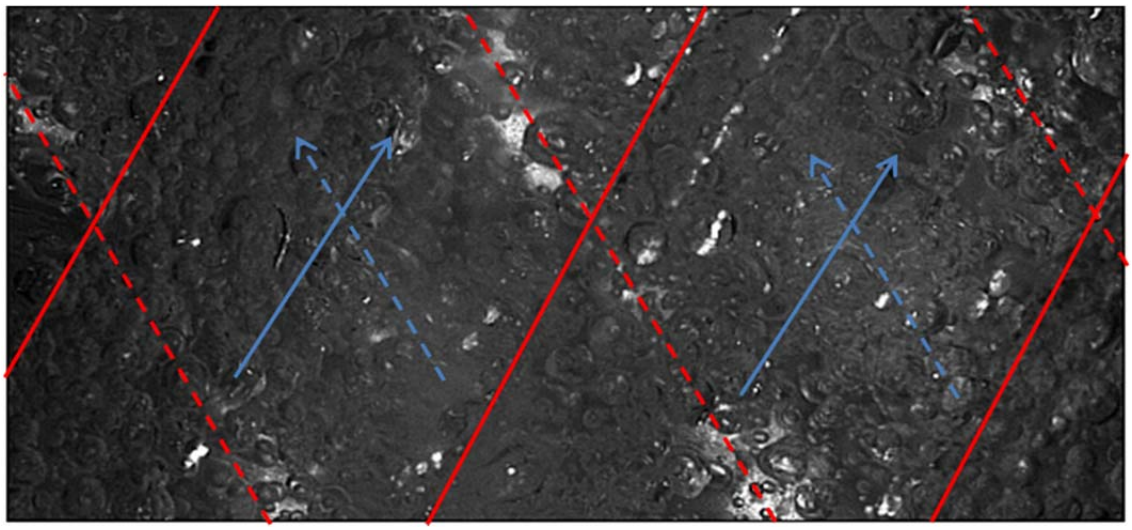

Figure 41 – Test series B3, run 2: axial position between pressure transducer P2 and P3. Typical of type II flow. Blue arrows represent direction of 'crossing flow' furrow-directed streams (solid - upper furrows; dashed – lower furrows)

Bubble Pathlines

Inspecting the flow pattern in test series B3, after the initial start-up transient had subsided, revealed a steady set of path lines that the bubbles appeared to follow regardless of bubble size. Different bubbles as far as 1 second apart and having different sizes and morphology could be observed following nearly identical pathways. The overall flow structure consists of a majority of bubbles following the corrugation direction, with several sub-streams whose shape and size did not vary appreciably with time. The consistent character of these flow paths, representative depictions of which are provided in Figure 42 - Figure 44, also supports the conclusion that approximately steady-state conditions exist even in the presence of a gas-generating chemical reaction.

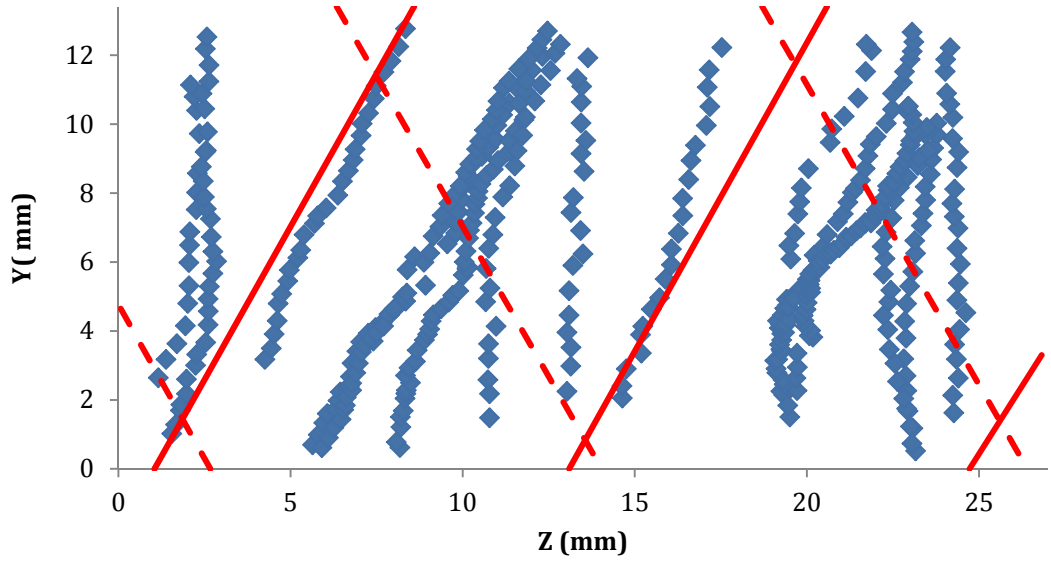

Figure 42 – Bubble path lines traced from test B3, run 1 at various times during steady-state condition. Lines indicate crests of furrows; solid lines represent the upper plate (transparent window) and dashed lines represent the lower plate

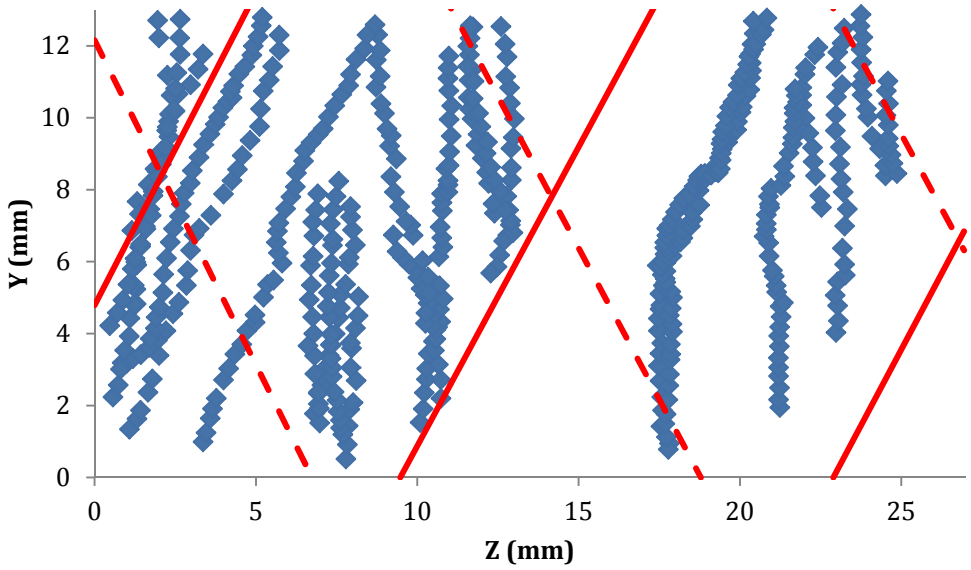

Figure 43 – Bubble path lines traced from test B3, run 2 at various times during steady-state condition

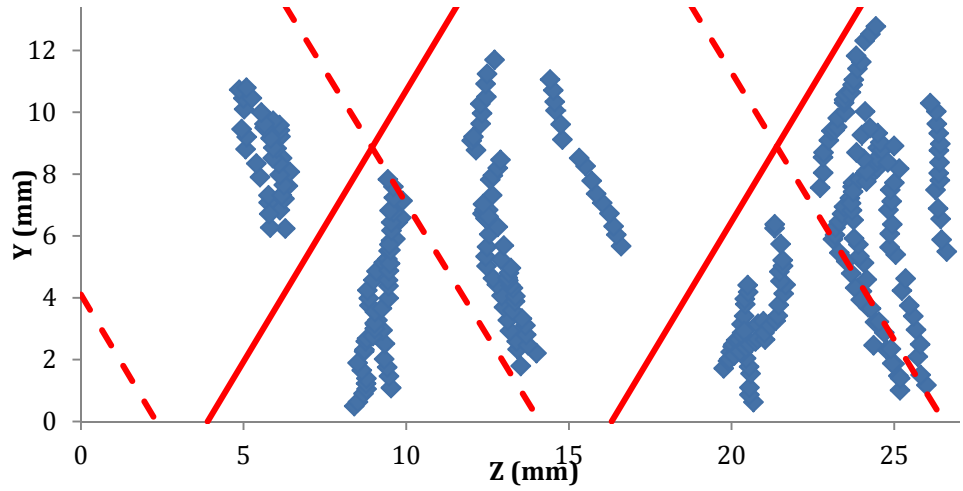

Figure 44 – Bubble path lines traced from test B3, run 3 at various times. Fewer bubbles were able to be tracked because there was a higher number of bubbles in this region that adhered to the window and obscured view

Since only a few frames were needed to approximate the instantaneous velocity of a bubble, data could be extracted from a broader set of high-speed video results, even in cases where the visibility did not permit bubbles to be accurately tracked for more than three frames. In this case, however, accurate resolution of the bubble's shape was required, since the small time scale would mean that errors in calculating position of an object between successive frames is amplified considerably. In performing these computations it was assumed that a bubble's bulk velocity was high relative to deformations it might undergo, which was observed to be the case except with particularly large or irregularly shaped bubbles (an infrequent occurrence). Hence, the bubble's instantaneous velocity could be predicted by tracking its geometric centroid. In the B3 test series, the calculated velocities, which were predominantly in the y-direction, did not correlate with bubble size. Slower bubbles tended to congregate near contact points between the upper and lower corrugations, whereas bubbles traveling along main furrow streams tended to be faster. Figure 45 shows the range of bubble velocities in the y-direction (main flow direction) that could be measured in a typical frame. The majority of bubbles were concentrated in the range of 0.1 to 0.3 m/s; the calculations performed to determine the gas velocity in the two-phase multiplier assessment section yielded higher predictions – around 0.5 m/s - for the average velocity in the stream-wise direction, indicating the void fraction may be underestimated by the Rouhani correlation [59]. It is important to keep in mind, however, that the bubbles measured were close to window, and may have been slower than bubbles deeper in the channel and more removed from the wall's influence.

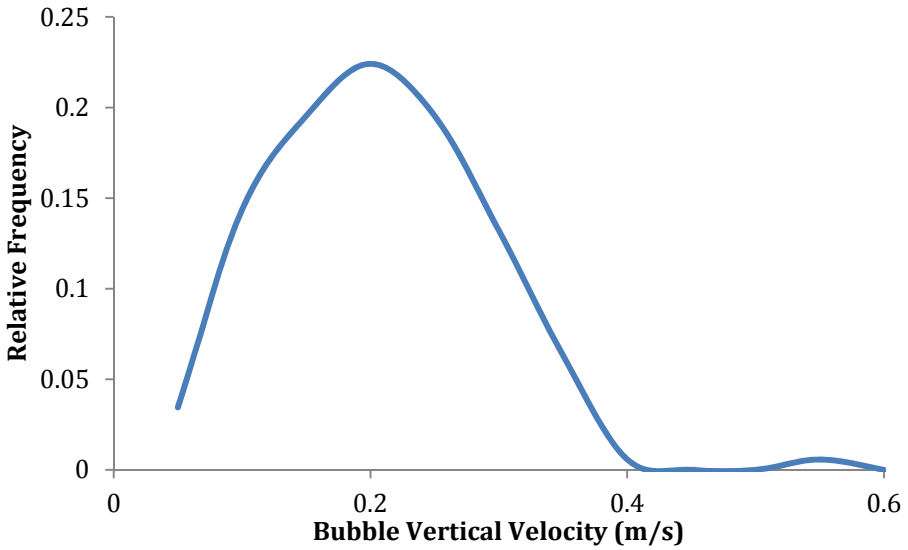

Figure 45 – Bubble velocity distribution sampled from test B3 run 1.Bubbles were selected from a "reference" frame, and their centroid position tracked for 7-10 frames thereafter. Velocity was calculated as $(Y_t - Y_{t+\Delta t})/\Delta t$, where Y_t is the y position of a bubble's centroid at time t and Δt is the time interval between successive frames (0.001 sec)

Bubble Size Distributions

Figure 46 and Figure 47 show bubble size distributions counted manually from test B3. The red lines and blue lines each represent a sample size of about 200 bubbles from various locations. Bubbles were measured and counted if their shape and size could be determined reasonably well. The different line colors indicate that the sample groups were taken from different frames, about one second apart in both cases. The observed region in run 1 was occupied by type I flow, and the reaction was so vigorous in this area that only bubbles at the window surface could be discerned. The regions in runs 2 and 3 were occupied by type II flow, but bubble adhesion to the window was severe in run 3, so only run 2 could be used to yield enough visible bubbles from which a size distribution could be estimated. However, the wider spacing between bubbles seen in type II flow allowed for bubbles at different depths to be

observed – these appeared to move somewhat faster than the flow at the window level. The similar shapes of the red and blue lines indicate that the bubble population sampled is representative of the true time-averaged size distribution of bubbles in the region observed by the camera.

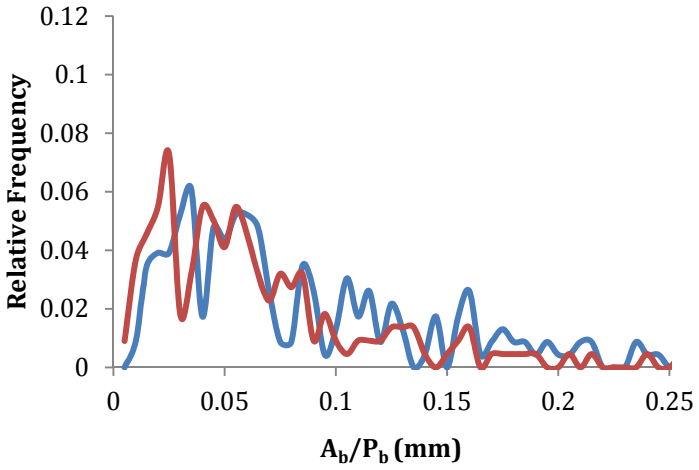

Figure 46 – Bubble size distribution for test B3, run 1

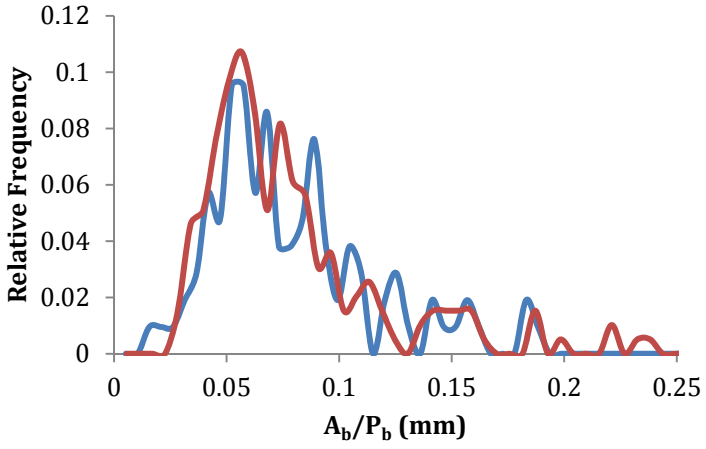

Figure 47 – Bubble size distribution for test B3, run 2

In the regions occupied by type I flow, characteristic bubble sizes (defined as the ratio of bubble area A_b to bubble perimeter P_b) were predominantly clustered in the $0 < L_c \leq 0.05$ mm region, as shown by the histogram in Figure 46. Type II flow regions showed a wider range of bubble sizes, and the dominant region was between 0.05 and 0.1 mm, which can be seen in Figure 47.

Overall, the video footage showed that the bubble paths conform to the paths of their respective furrows, but bubbles in the mid-plane region where the upper and lower plates meet will follow sub-stream patterns induced by the interaction from the crossing main flow streams; in other words, the single-phase flow path is unaltered by the presence of bubbles, which is consistent with the observation from the flow visualization study of Tribbe and Müller-Steinhagen [58] for bubbly flow. As the total gas evolved by the reaction increases, the flow path again remains unaltered from its single-phase counterpart, but the typical bubble size decreases and the bulk flow takes on a froth or foam-like appearance owing to both the tortuosity of the flow path and the rapid gas evolution, which constrained the size range that a bubble could take. In no instances were any large heterogeneous flow structures observed, which suggests that a homogenous friction factor and/or void fraction model is permissible.

CHAPTER IV

CONCLUSIONS AND FUTURE WORK

In this study, a reduced-order numerical model was developed to solve the coupled heat, mass, and momentum transfer equations for a multi-phase, continuous flow reactor for high heat flux thermal management applications. This model was used to demonstrate the feasibility of the reactor architecture by analyzing a prototype sizing problem. Experiments were performed with a simulated chevron PHE reactor utilizing high-speed flow visualization and reactor pressure measurements. The experimental results were consistent with the model predictions for total pressure drop.

The example set of results shown for the numerical model developed in this study indicate that high power ratings can be achieved with a compact reactor operating at near atmospheric pressure conditions and a modest heat rejection temperature (62°C slurry and 70°C load), without the use of a vacuum pump, as in Schmidt's reactor [2]. The model predictions for the Alfa Laval M3 gasketed plate heat exchanger show that low slurry residence times are desirable, allowing for roughly 50% of the thermal load to be rejected as latent heat when passing 0.005 L/s in each slurry channel for inlet pressures between 102 and 110 kPa. This model can be used to incorporate new experimental data for heat and momentum transfer for improving fidelity, in addition to accounting for non-idealities such as flow and pressure maldistribution. The numerical model was used to successfully account for a variety of input parameters and solve the coupled heat, mass, and momentum transfer problem to a high degree of precision. The numerical robustness of the model affords a wide range of reactor designs that may be explored without compromising accuracy or stability. Calculations are executed within a reasonable time frame (10-30 min) for both small and medium reactors (7-20 plates), thereby allowing comprehensive parametric studies to be performed for design optimization.

Based on a comparison of the model results for different flow rates, pressures, and load temperatures, it is apparent that the dominant parameter governing the conversion efficiency of the reactor is the residence time. An additional effectiveness metric, the LL-ratio, for gauging the performance of a reactor design and operating condition combination was introduced based on the objective of rejecting the greatest possible quantity of waste heat in the form of chemical latent heat. Hence, this implies that the temperature difference between the cold and hot streams be minimized - the model shows that the extent of hot/cold stream minimization that is plausible (such that full conversion is attained) is tied directly to the relative timescales for heat transfer between the two streams and the chemical reaction. At pressures close to atmospheric conditions, the LL-ratio is more strongly influenced by the residence time. However, increasing the LL-ratio comes at the expense of the total power rating, and vice versa. Maximizing the performance (in terms of heat duty and the amount of energy rejected as latent heat) of a given reactor geometry requires an optimal balance between the power rating and the LL-ratio, which will depend on the application.

These thermal performance predictions furnished by the model demonstrate that it is possible to convey high heat fluxes to a high energy density thermo-chemical heat sink using a chevron PHE. The exploitation of the superior heat transfer characteristics of chevron PHEs extends the reactive slurry concept to a novel system that does not sacrifice the advantage of high energy density by requiring excessive system volume and heat transfer surface area. This architecture will also scale more favorably than a batch reactor based design. These advantages stem from the higher surface area-to-volume ratio, and the higher overall heat transfer coefficients characteristic of PHEs compared to stirred tank reactors, which has been well documented in the chemical engineering literature [5, 6].

The absolute pressure data obtained from the simulated reactor showed that the rise in back pressure due to the evolution of gaseous products is far more significant than the effect of pressure drop. The amount of gas generation was found to correlate positively with the reactor pressure. Examining the gas superficial velocity at the outlet based on a mass balance and the ideal gas equation of state reveals a monotonically increasing gas velocity with increased gas flux, but with a decreasing slope. As this effect coincides with increased reactor pressure, one concludes that additional hydrodynamic resistance to gas flow is responsible for the increase in back pressure. Therefore, further refinement of the predictive model would require a means to account for the escape kinetics of the gas products as a function of the hydrodynamic conditions in the reactor chamber. This is the determining factor in the back pressure rise and would tend to slow the reaction rate.

The flow visualization results show that the basic flow patterns observed in earlier studies are preserved, validating the assumption that the two-phase multiplier approach used by Tribbe and Müller-Steinhagen [58] may be applied to a gas-generating reacting flow in a PHE. It was observed that the violent hydrodynamics arising from the gas-generating chemical reaction limits the size of bubbles. The average bubble size is reduced even further with increased gas generation, whereas in previous studies, larger gas fluxes tended to give rise to larger gas-continuous regions and slug-like behavior. In place of slug flow and gas pockets, a froth-like flow with nearly uniform bubble sizes (and the occasionally larger bubble) exists when larger quantities of gas are produced, irrespective of liquid velocity. The absence of these gas-continuous regions confirms that the gas products will not impede heat transfer. No previous studies have been reported on the hydrodynamics in chevron PHEs of this nature.

The two-phase multiplier calculations derived from the data show that substantial increases in the frictional pressure drop are produced by the presence of the chemical reaction.

The magnitude of this increase is underestimated by the correlation proposed by Tribbe and Müller-Steinhagen [58], which did not include any gas-generating chemical reaction. The comparison shows that the effect of the chemical reaction is responsible for appreciably stronger momentum transport than non-reactive gas and liquid flow. Equation (76) implies that the heat transfer will also be enhanced considerably by action of the gas generation. Thus, the estimates for thermal performance obtained using Tribbe and Müller-Steinhagen's correlation for Φ_{TP}^2 are probably lower than that of a real AC reactor, from the standpoint of minimizing the requisite cold/hot stream temperature differences for 100% conversion.

The path toward improving model fidelity may be approached from four fronts, involving both experimental and computational efforts:

1. A more detailed understanding of gas escape kinetics inside PHEs
2. A system-level model
3. Improved heat transfer correlations
4. Improved chemical kinetic models

Since the complex flow inside PHEs will likely preclude the development of a general model for gas escape kinetics, a study similar to this one but encompassing a broader range of mass qualities and flow rates, and for different PHE models, would be quite useful.

Further, it is also desirable to develop a numerical model for a system level thermal performance analysis, incorporating the reactor architecture considered in this study, since at this point only the reactor is considered alone, and the operating parameters used in the present model would depend on external components. On the experimental side, the obvious next step is to test the thermal performance of the proposed reactor architecture with actual ammonium carbamate slurry and subsequently utilize the findings in tuning and re-evaluating both the kinetic model and the heat transfer correlations used in the heat exchanger numerical model. It

will also be important to consider the effect of suspended AC particles on the rheology of the liquid phase, since solid suspensions have been known to cause non-Newtonian shear-thinning behavior [36].

The current model used to predict the kinetic behavior of ammonium carbamate was developed under static conditions, and may not be an adequate prediction tool for the range of operating conditions the reactor model will have to consider. Therefore, addressing the inadequacies in the current state of understanding of the ammonium carbamate decomposition under dynamic conditions in a heat transfer fluid is without question the most important issue in advancing this reactor scheme to a practical level of technical maturity.

The AC decomposition products generated within the reactor also represent an opportunity to reclaim the waste heat for other purposes. The gaseous NH_3 and CO_2 may be separated and stored so that the exothermic reformation of solid AC may be exploited to release the stored thermo-chemical energy at a later time. This idea was proposed in a patent concerning a solar power plant scheme [3], wherein the decomposition reaction was driven by the collection of solar energy. The component gases would then be re-combined when needed to supply the energy for steam generation. Such a process would require high pressures, in accordance with the relation for $P_{eq}(T)$ (Equation (5)), but is nevertheless worthy of further consideration.

REFERENCES

[1] G. Glatzmaier, Summary Report for Concentrated Solar Power Thermal Workshop, NREL (2011).

[2] J.E. Schmidt, The Use of Ammonium Carbamate as a High Specific Thermal Energy Density Material for Thermal Management of Low Grade Heat, MS Thesis, University of Dayton, Dayton, OH (2011).

[3] R. T. Lefroi, Solar Energy Heat Utilization, US Patent 4169499, (1979).

[4] A.A. Koutinas, P. Yianoulis, A. Lycourghiotis, Industrial scale modeling of the thermochemical energy storage system based on CO2 2NH3 NH2COONH4 equilibrium, Energy Conversion and Management 23 (1983) 55-63.

[5] Z. Anxionnaz, M. Cabassud, C. Gourdon, P. Tochon, Heat exchanger/reactors (HEX reactors): Concepts, technologies: State-of-the-art, Chemical Engineering and Processing: Process Intensification. 47 (2008) 2029-2050.

[6] A. M. Edge, I. Pearce, C. H. Phillips, C. H., Compact Heat Exchangers as Chemical Reactors for Process Intensification (PI), Process Intensification in Practice 28 (1997) 175-189.

[7] Z.W. Ma, P. Zhang, Pressure drop and heat transfer characteristics of clathrate hydrate slurry in a plate heat exchanger, Int. J. Refrig. 34 (2011) 796-806.

[8] J. Bellas, I. Chaer, S.A. Tassou, Heat transfer and pressure drop of ice slurries in plate heat exchangers, Appl. Therm. Eng. 22 (2002) 721-732.

[9] W.W. Focke, Turbulent convective transfer in plate heat exchangers, Int. Commun. Heat Mass Transfer. 10 (1983) 201-210.

[10] W.W. Focke, J. Zachariades, The effect of the corrugation inclination angle on the thermohydraulic performance of plate heat exchangers, Int. J. Heat Mass Transfer. 28 (1985) 1469-1479.

[11] D. Dović, B. Palm, S. and Švaić, Generalized correlations for predicting heat transfer and pressure drop in plate heat exchanger channels of arbitrary geometry, Int. J. Heat Mass Transfer. 52 (2009) 4553-4563.

[12] W.W. Focke, P.G. Knibbe, Flow visualization in parallel-plate ducts with corrugated walls, J. Fluid Mech. 165 (1986) 73-77.

[13] R. L. Shah, W.W. Focke, Plate heat exchangers and their design theory, in: R.K. Shah, E.C. Subbarao, R.A. Mashelkar (Eds.), Heat Transfer Equipment Design, Hemisphere Publishing, New York (1988), pp. 227-254.

[14] K. Nilpueng, S. Wongwises, Two-phase gas–liquid flow characteristics inside a plate heat exchanger, Exp. Therm. Fluid Sci. 34 (2010) 1217-1229.

[15] W.W. Focke, Asymmetrically corrugated plate heat exchanger plates, Int. Commun. Heat Mass Transfer. 12 (1985) 67-77.

[16] A. Muley, R.M. Manglik, Experimental study of turbulent flow heat transfer and pressure drop in a plate heat exchanger with chevron plates, J. Heat Transfer. 121 (1999) 110-117.

[17] A.G. Kanaris, A.A. Mouza, S.V. Paras, Optimal design of a plate heat exchanger with undulated surfaces, Int. J. Thermal Sci. 48 (2009) 1184-1195.

[18] L. Zhang, D. Che, Influence of corrugation profile on the thermalhydraulic performance of cross-corrugated plates, Num. Heat Transfer A. 59 (2011) 267-296.

[19] R. L. Heavner, H. Kumar, Wanniarachchi, 1993, Performance of an industrial heat exchanger: the effect of chevron angle, ALChE Symposium Series 89, (1993) 262-267.

[20] R. Shah, D. Sekulić, Fundamentals of Heat Exchanger Design, John Wiley and Sons, New Jersey, 2003.

[21] M.C. Georgiadis, S. Macchietto, Dynamic modelling and simulation of plate heat exchangers under milk fouling, Chem. Eng. Sci. 55 (2000) 1605-1619.

[22] M. Ciofalo, J. Stasiek, M.W. Collins, Investigation of flow and heat transfer in corrugated passages—II. Numerical simulations, Int. J. Heat Mass Transfer. 39 (1996) 165-192.

[23] S. Jain, A. Joshi, P.K. Bansal, A new approach to numerical simulation of small sized plate heat exchangers with chevron plates, J. Heat Transfer. 129 (2007) 291-297.

[24] Y. Tsai, F. Liu, P. Shen, Investigations of the pressure drop and flow distribution in a chevron-type plate heat exchanger, Int. Commun. Heat Mass Transfer. 36 (2009) 574-578.

[25] S. Freund, S. Kabelac, Investigation of local heat transfer coefficients in plate heat exchangers with temperature oscillation IR thermography and CFD, Int. J. Heat Mass Transfer. 53 (2010) 3764-3781.

[26] I. Gherasim, M. Taws, N. Galanis, C.T. Nguyen, Heat transfer and fluid flow in a plate heat exchanger part I. experimental investigation, Int. J. Therm. Sci. 50 (2011) 1492-1498.

[27] P.J. Heggs, P. Sandham, R.A. Hallam, C. Walton, Local transfer coefficients in corrugated plate heat exchanger channels, Chem. Eng. Res. Design 75 (1997) 641-645.

[28] M.M. Abu-Khader, Plate heat exchangers: recent advances, Renew. Sustain. Energy Reviews. 16 (2012) 1883-1891.

[28] M. Frejacques, Les base theoriques de la synthese industrielle de l'uree, Chim. Ind. 60 (1948) 22.

[29] B. Claudel, L. Boulamri, A new model of gas-solid kinetics: the case of ammonium carbamate formation and decomposition, Thermochimica Acta. 126 (1988) 129-148.

[30] B.R. Ramachandran, A.M. Halpern, E.D. Glendening, Kinetics and mechanism of the reversible dissociation of ammonium carbamate: involvement of carbamic acid, J. Phys. Chem. A. 102 (1998) 3934-3941.

[31] R. N. Bennet, P.D. Ritchie, D. Roxburgh, J. Thomson, The system ammonia + carbon dioxide + ammonium carbamate part I – The equilibrium of thermal dissociation of ammonium carbamate, Transactions of the Faraday Society 49 (1953) 925-929.

[32] E.P.J. Egan, J.E.J. Potts, G.D. and Potts, Dissociation pressure of ammonium carbamate, Ind. Eng. Chem. 38 (1946) 454-456.

[33] T.R. Briggs, V. and Migrdichian, The ammonium carbomate equilibrium, J. Phys. Chem. 28 (1924) 1121-1135.

[34] A. Bejan, Convection Heat Transfer*,* John Wiley and Sons, New Jersery, 2004.

[35] K.G. Clark, H.C. and Hetherinton, The heat of formation of ammonium carbamate from ammonia and carbon dioxide, J. Am. Chem. Soc. 49 (1927) 1909-1915.

[36] D. Azbel, A. L. Liapis, Motion of solid particles in a liquid medium, in: N.P. Cheremisinoff , R. Gupta (Eds.), Handbook of Fluids in Motion, Ann Arbor Science, Ann Arbor (1983), pp. 895-927

[37] J. G. Collier, J.R. Thome, Convective Boiling and Condensation, third ed., Oxford University Press, New York, 1996.

[38] V. P. Carey, Liquid-Vapor Phase-Change Phenomena: An Introduction to the Thermophysics of Vaporization and Condensation Processes in Heat Transfer Equipment*,* Hemisphere Publishing, New York, 1992.

[39] T. Sun, A.S. and Teja, Density, viscosity and thermal conductivity of aqueous solutions of propylene glycol, dipropylene glycol, and tripropylene glycol between 290 K and 460 K, J. Chem. Eng. Data 49 (2004) 1311-1317.

[40] F. P. Incropera, D. P. Dewitt, T. L. Bergman, A. S. Lavine, Fundametals of Heat and Mass Transfer, sixth ed., John Wiley and Sons, New Jersey, 2007.

[41] H. Martin, A theoretical approach to predict the performance of chevron-type plate heat exchangers, Chem. Eng. Proc. 35 (1996) 301-310.

[42] B. Thonon, Plate heat exchangers: a review of correlations for single-phase flow heat transfer and pressure drop, Int. J. Heat Exchangers 6 (2004) 1-34.

[43] A. Muley, R.M. Manglik, H.M. Metwally, Enhanced heat transfer characteristics of viscous liquid flows in a chevron plate heat exchanger, J. Heat Transfer. 121 (1999) 1011-1017.

[44] B. Thonon, R. Vidil, C. Marvillet, Recent research and developments in plate heat exchangers, J. Enhanced Heat Transfer 2 (1995) 149-155.

[45] M. F. Edwards, Heat transfer in plate heat exchangers at low Reynolds numbers, in: S. Kakaç (Ed.), NATO Advanced Study Institute, Turkey (1988), pp. 23-37.

[46] C.S. Fernandes, R.P. Dias, J.M. Nóbrega, J.M. Maia, Laminar flow in chevron-type plate heat exchangers: CFD analysis of tortuosity, shape factor and friction factor, Chem. Eng. Proc. 46 (2007) 825-833.

[47] J. Ding, R. Manglik, Analytical solutions for laminar fully developed flows in double-sine shaped ducts, Heat and Mass Transfer. 31 (1996) 269-277.

[48] G. Gaiser, *Stömungs- und Transportvorgänge in gewellten Strukturen*, Stuttgart (1990).

[49] H.M. Metwally, R.M. Manglik, Enhanced heat transfer due to curvature-induced lateral vortices in laminar flows in sinusoidal corrugated-plate channels, Int. J. Heat Mass Transfer. 47 (2004) 2283-2292.

[50] T.A. Rush, T.A. Newell, A.M. Jacobi, An experimental study of flow and heat transfer in sinusoidal wavy passages, Int. J. Heat Mass Transfer. 42 (1999) 1541-1553.

[51] D. Dović, B. Palm, S. and Švaić, Generalized correlations for predicting heat transfer and pressure drop in plate heat exchanger channels of arbitrary geometry, Int. J. Heat Mass Transfer 52 (2009) 4553-4563.

[52] J.R. García-Cascales, F. Vera-García, J.M. Corberán-Salvador, J. Gonzálvez-Maciá, Assessment of boiling and condensation heat transfer correlations in the modelling of plate heat exchangers, Int. J. Refrig. 30 (2007) 1029-1041.

[53] Y. Shiomi, S. Nakanishi, T. Uehara, Characteristics of two-phase flow in a channel formed by chevron type plates, Exp. Therm. Fluid Sci. 28 (2004) 231-235.

[54] G. Kreissig, H.M. Müller-Steinhagen, Frictional pressure drop for gas/liquid two-phase flow in plate heat exchangers, Heat Transfer Eng. 13 (1992) 42-52.

[55] A. E. Dukler, Two Phase Flow Data Analysis and Correlation Studies, Houston (1964).

[56] P. Vlasogiannis, G. Karagiannis, P. Argyropoulos, V. Bontozoglou, Air–water two-phase flow and heat transfer in a plate heat exchanger, Int. J. Multiphase Flow. 28 (2002) 757-772.

[57] C. Tribbe, H.M. Müller-Steinhagen, Gas/liquid flow in plate-and-frame heat exchangers - part I: pressure drop measurements, Heat Transfer Eng. 22 (2001) 5-11.

[58] C. Tribbe, H.M. Müller-Steinhagen, Gas/liquid flow in plate-and-frame heat exchangers - part II: two-phase multiplier and flow pattern analysis, Heat Transfer Eng. 22 (2001) 12-21.

[59] S.Z. Rouhani, E. Axelsson, Calculation of void volume fraction in the subcooled and quality boiling regions, Int. J. Heat Mass Transfer. 13 (1970) 383-393.

[60] M. Ishii, One-dimensional drift-flux model and constitutive equations for relative motion between phases in various two-phase flow regimes, ANL-77-47, Argonne National Lab (1977).

[61] T.S. Khan, M.S. Khan, M. Chyu, Z.H. Ayub, Experimental investigation of single phase convective heat transfer coefficient in a corrugated plate heat exchanger for multiple plate configurations, Appl. Thermal Eng. 30 (2010) 1058-1065.

[62] S. Kakaç, R. K. Shah, W. Aung, Handbook of Single-Phase Convective Heat Transfer, John Wiley and Sons, New York, 1987

[63] E.-U. Schlünder, Analogy between heat and momentum transfer, Chem. Eng. Proc.. 37 (1998) 103-107.

[64] A. Lévêque, Les lois de la transmission de chaleur par convection, Ann. Mines 12 (1928) 201-415.

[65] A.S. Jones, Heat transfer in the thermal entrance region of a flat duct, J. Aus. Math. Soc. A 19 (1975) 146-160.

[66] P. L. Geiringer, Handbook of Heat Transfer Media, Reinhold Publishing Corp., New York, 1962.

[67] I. Mudawar, Assessment of high-heat-flux thermal management schemes, Components Packaging Tech., IEEE Transactions on. 24 (2001) 122-141.

[68] C.H. Amon, J. Murthy, S.C. Yao, S. Narumanchi, C. Wu, C. Hsieh, MEMS-enabled thermal management of high-heat-flux devices EDIFICE: embedded droplet impingement for integrated cooling of electronics, Exp. Thermal Fluid Sci. 25 (2001) 231-242.

[69] B. Parkash, Reaction of RCOOH-$NAHCO_3$, a convenient illustration, Resonance (1998) 89-95.

[70] P. Sahoo, B. Saha, Inadequacy of water band movement technique for kinetic interpretation of RCOOH-$NAHCO_3$ reaction, Resonance (1999) 65-71.

[71] D.R. Lide, CRC Handbook of Chemistry and Physics, 86th ed., CRC Press, Boca Raton, 2005.

[72] J. V. Sengers, B. Kamgar-Parsi, Representative equations for the viscosity of water substance, J. Phys. Chem. Ref. Data 13 (1984) 185-205.

[73] S. J. Kline, F. A. and McClintock, Describing uncertainties in single-sample experiments, Mech. Eng. 1 (1953) 3-8.

APPENDIX A

TOTAL PRESSURE DROP CALCULATED FROM NUMERICAL MODEL

COMPARED TO EXPERIMENTAL MEASUREMENTS

Table A-1 – Total pressure drop measured from two-phase experiments compared to total pressure drop predicted using numerical model

Series	Run	ΔP, exp. (kPa)	ΔP, calc. (kPa)	Error (%)
A1	1	3.90	5.34	36.82
	2	3.81	5.37	40.89
	3	3.86	5.34	38.46
A4	1	4.11	5.78	40.65
	2	4.07	5.74	41.12
	3	4.04	5.77	42.67
A6	1	3.62	4.60	26.92
	2	3.62	4.66	28.75
	3	3.89	4.60	18.23
A7	1	3.66	4.25	16.16
	2	4.01	4.28	6.77
	3	4.14	4.27	3.17
A8	1	3.26	3.49	6.84
	2	3.17	3.45	8.95
	3	3.25	3.48	7.29
A9	1	3.06	3.19	4.14
	2	3.06	3.19	4.16
	3	3.36	3.18	5.16
B1	1	3.89	4.85	24.89
	2	3.78	4.93	30.55
	3	3.85	4.99	29.52
B2	1	3.79	4.41	16.41
	2	3.72	4.45	19.36
	3	3.54	4.44	25.45
B3	1	3.32	4.17	25.87
	2	3.52	4.14	17.51
	3	3.48	4.17	19.84
B4	1	4.13	5.49	32.89
	2	4.10	5.39	31.55
	3	4.13	5.36	29.88
	4	4.11	5.41	31.86
	5	4.04	6.01	48.69

Table A-1 Continued

Series	Run	ΔP, exp. (kPa)	ΔP, calc. (kPa)	Error (%)
C1	1	4.19	6.06	44.76
	2	4.06	5.98	47.47
	3	4.09	6.06	48.39
C2	1	3.93	5.31	34.97
	2	3.89	5.37	38.22
	3	3.71	5.49	47.87
C3	1	2.97	4.12	38.63
	2	2.91	4.08	40.20
	3	2.76	4.06	47.07
D1	1	4.11	4.24	3.30
	2	3.81	4.27	12.11
	3	3.87	4.27	10.40
D2	1	3.69	3.83	3.75
	2	3.86	3.89	0.70
D3	1	3.89	5.36	37.86
	2	3.97	5.63	42.03
	3	3.92	5.60	42.65
D4	1	3.61	4.02	11.39
	2	3.40	4.00	17.47
	3	3.45	4.06	17.64

APPENDIX B

EXPERIMENTAL PARAMETER UNCERTAINTY

The following tables show the relative uncertainty in percentages for experimental parameters relevant to the two-phase flow tests.

Table B1 – Relative uncertainties in experimental parameters for two-phase flow test series A calculated using Klein-McClintock method; units are in %

A1			
Run #	1	2	3
Re	3.53	3.45	3.63
Cin, Bicarb	10.89	11.27	11.93
Cin, Acid	5.00	6.03	5.73
PG Strength (Adjusted)	1.21	1.24	1.30
Viscosity	6.08	6.08	6.09
Acid Flow Rate	5.15	6.67	5.85
Bicarb Flow Rate	3.16	2.49	3.62
A5			
Run #	1		
Re	3.12		
Cin, Bicarb	7.00		
Cin, Acid	3.62		
PG Strength (Adjusted)	0.88		
Viscosity	6.04		
Acid Flow Rate	4.22		
Bicarb Flow Rate	0.45		
A4			
Run #	1	2	3
Re	3.39	3.31	3.22
Cin, Bicarb	7.64	8.35	14.34
Cin, Acid	4.17	4.11	5.54
PG Strength (Adjusted)	0.93	0.99	3.12
Viscosity	6.05	6.05	6.52
Acid Flow Rate	4.86	4.39	4.55
Bicarb Flow Rate	0.22	2.15	1.00

Table B1 Continued

A6			
Run #	1	2	3
Re	3.13	3.12	3.14
Cin, Bicarb	4.54	4.52	5.52
Cin, Acid	3.69	4.03	5.04
PG Strength (Adjusted)	1.42	1.42	1.55
Viscosity	6.05	6.05	6.06
Acid Flow Rate	4.31	4.66	5.93
Bicarb Flow Rate	0.51	0.36	0.23
A7			
Run #	1	2	3
Re	3.13	3.15	3.16
Cin, Bicarb	4.70	4.85	4.90
Cin, Acid	3.60	3.90	3.98
PG Strength (Adjusted)	1.44	1.46	1.46
Viscosity	6.05	6.05	6.05
Acid Flow Rate	4.27	4.58	4.65
Bicarb Flow Rate	0.44	0.63	0.79
A8			
Run #	1	2	3
Re	3.17	3.48	3.43
Cin, Bicarb	8.55	7.43	9.54
Cin, Acid	8.28	7.18	9.82
PG Strength (Adjusted)	2.37	2.13	2.59
Viscosity	6.09	6.07	6.11
Acid Flow Rate	4.62	4.26	6.78
Bicarb Flow Rate	3.66	2.78	1.11
A9			
Run #	1	2	3
Re	3.17	3.13	3.12
Cin, Bicarb	8.33	7.35	7.33
Cin, Acid	3.63	3.34	6.92
PG Strength (Adjusted)	2.32	2.12	2.11
Viscosity	6.08	6.07	6.07
Acid Flow Rate	4.35	4.11	4.47
Bicarb Flow Rate	3.46	2.87	2.11

Table B2 - Relative uncertainties in experimental parameters for two-phase flow test series B calculated using Klein-McClintock method; units are in %

B1			
Run #	1	2	3
Re	0.09	0.04	0.04
Cin, Bicarb	0.44	0.19	0.14
Cin, Acid	0.11	0.08	0.05
PG Strength (Adjusted)	0.21	0.02	0.01
Viscosity	0.18	0.06	0.06
Acid Flow Rate	0.11	0.09	0.05
Bicarb Flow Rate	0.04	0.04	0.04
B2			
Run #	1	2	3
Re	0.04	0.04	0.04
Cin, Bicarb	0.22	0.21	0.20
Cin, Acid	0.07	0.07	0.07
PG Strength (Adjusted)	0.02	0.02	0.02
Viscosity	0.06	0.06	0.06
Acid Flow Rate	0.08	0.07	0.08
Bicarb Flow Rate	0.05	0.05	0.03
B3			
Run #	1	2	3
Re	0.04	0.04	0.04
Cin, Bicarb	0.32	0.15	0.16
Cin, Acid	0.11	0.05	0.05
PG Strength (Adjusted)	0.03	0.02	0.02
Viscosity	0.07	0.06	0.06
Acid Flow Rate	0.14	0.05	0.05
Bicarb Flow Rate	0.03	0.04	0.04
B4			
Run #	1	2	3
Re	0.04	0.03	0.03
Cin, Bicarb	0.15	0.11	0.09
Cin, Acid	0.05	0.04	0.03
PG Strength (Adjusted)	0.02	0.01	0.01
Viscosity	0.06	0.06	0.06
Acid Flow Rate	0.06	0.04	0.04
Bicarb Flow Rate	0.04	0.02	0.01

Table B2 Continued

B4			
Run #	4	5	
Re	0.03	0.03	
Cin, Bicarb	0.10	0.10	
Cin, Acid	0.04	0.03	
PG Strength (Adjusted)	0.01	0.01	
Viscosity	0.06	0.06	
Acid Flow Rate	0.04	0.04	
Bicarb Flow Rate	0.01	0.01	

Table B3 - Relative uncertainties in experimental parameters for two-phase flow test series C calculated using Klein-McClintock method; units are in %

C1			
Run #	1	2	3
Re	0.04	0.04	0.03
Cin, Bicarb	0.38	0.36	0.30
Cin, Acid	0.03	0.03	0.03
PG Strength (Adjusted)	0.02	0.02	0.02
Viscosity	0.06	0.06	0.06
Acid Flow Rate	0.05	0.04	0.04
Bicarb Flow Rate	0.02	0.03	0.01
C2			
Run #	1	2	3
Re	0.04	0.03	0.03
Cin, Bicarb	0.36	0.35	0.29
Cin, Acid	0.03	0.03	0.03
PG Strength (Adjusted)	0.02	0.02	0.02
Viscosity	0.06	0.06	0.06
Acid Flow Rate	0.04	0.05	0.05
Bicarb Flow Rate	0.03	0.01	0.01

Table B3 Continued

C4			
Run #	1	2	3
Re	0.04	0.04	0.04
Cin, Bicarb	0.35	0.35	0.36
Cin, Acid	0.03	0.03	0.03
PG Strength (Adjusted)	0.02	0.02	0.02
Viscosity	0.06	0.06	0.06
Acid Flow Rate	0.04	0.04	0.04
Bicarb Flow Rate	0.04	0.04	0.04

Table B4 - Relative uncertainties in experimental parameters for two-phase flow test series D calculated using Klein-McClintock method; units are in %

D1			
Run #	1	2	3
Re	0.03	0.03	0.03
Cin, Bicarb	0.04	0.05	0.04
Cin, Acid	0.04	0.05	0.03
PG Strength (Adjusted)	0.02	0.02	0.02
Viscosity	0.06	0.06	0.06
Acid Flow Rate	0.04	0.06	0.04
Bicarb Flow Rate	0.01	0.02	0.00
D2			
Run #	1	2	
Re	0.03	0.03	
Cin, Bicarb	0.05	0.04	
Cin, Acid	0.04	0.04	
PG Strength (Adjusted)	0.02	0.02	
Viscosity	0.06	0.06	
Acid Flow Rate	0.05	0.05	
Bicarb Flow Rate	0.00	0.03	
D3			
Run #	1	2	3
Re	0.03	0.03	0.03
Cin, Bicarb	0.11	0.12	0.11

Table B4 Continued

D3			
Cin, Acid	0.03	0.04	0.03
PG Strength (Adjusted)	0.01	0.02	0.01
Viscosity	0.06	0.06	0.06
Acid Flow Rate	0.04	0.05	0.04
Bicarb Flow Rate	0.00	0.00	0.00
D4			
Run #	1	2	3
Re	0.03	0.03	0.03
Cin, Bicarb	0.13	0.11	0.12
Cin, Acid	0.03	0.03	0.03
PG Strength (Adjusted)	0.02	0.01	0.02
Viscosity	0.06	0.06	0.06
Acid Flow Rate	0.04	0.04	0.04
Bicarb Flow Rate	0.02	0.01	0.01

VITA

Name: Nicholas Paul Niedbalski

Address: Department of Mechanical Engineering

c/o Dr. Debjyoti Banerjee

Texas A&M University

College Station, TX 77843-3123

E-mail: nickgonzaga@me.com

Education: M.S., Mechanical Engineering

Texas A&M University, College Station, August 2012

B.S., Mechanical Engineering,

Gonzaga University, Spokane, May 2010

Publications:

Refereed Journal

- Aziz, A. and Niedbalski, N., 2011, "Thermally developing microtube gas flow with axial conduction and viscous dissipation", Int. J. Thermal Sci. 50 (3), pp. 332-340.

Peer Reviewed and Refereed Conference

- Niedbalski, N. Kang, S.-W., and Banerjee, D., 2011 "Numerical Study of Microchamber Filling in Centrifugal Microfluidics", Proc. ASME 2011 IMECE, Denver, CO.
- San Andres, L., Chirathadam, T. A., Ryu, K., Kim, T. H., Jarrett, C., Hagen, K., Martinez, A., Rice, B., Niedbalski, N., Hung, W., and Johnson, M., 2009, "Gas Bearing Technology for Oil-Free Microturbomachinery: Research Experience for Undergraduate (REU) at Texas A&M University", Proc. ASME Turbo Expo 2009.